Diss. ETH N^{o} 19225

Geophysics and non-destructive testing for transport infrastructure, with special emphasis on ground penetrating radar

A dissertation submitted to the
ETH ZURICH

for the degree of
Doctor of Sciences

presented by
JOHANNES HUGENSCHMIDT
Diplom-Geophysiker
Freie Universität Berlin, Germany
Executive MBA
University of St. Gallen

born June 1, 1960
citizen of Germany

accepted on the recommendation of
Prof. Dr. Alan G. Green, examinator
Prof. Dr. Eugen Brühwiler, co-examinator
Prof. Dr. Hansruedi Maurer, co-examinator

2010

For Paula

and Egon

Table of contents

Zusammenfassung **6**

Summary **8**

1 Introduction **9**

1.1 Transport infrastructure in Switzerland 9

1.2 Geophysics and non-destructive testing of transport infrastructure 13

1.3 Ground penetrating radar 20

1.4 GPR and non-destructive testing of transport infrastructure, with emphasis on contributions of the author 29

2 GPR inspection of concrete bridges **33**

3 Detection of chlorides and moisture in concrete structures with ground penetrating radar **47**

4 The inspection of retaining walls using GPR **58**

5 Processing strategies for high-resolution GPR concrete inspections **76**

6 Conclusions and outlook **90**

6.1 Conclusions 90

6.2 Outlook 91

Acknowledgements **93**

References **94**

7 Appendix A - Symbols and constants **100**

8 Appendix B - GPR inspection of a mountain motorway in Switzerland **101**

9 Appendix C - Railway track inspection using GPR **113**

10 Appendix D - Concrete bridge inspection with a mobile GPR system **123**

11 Appendix E - Curriculum vitae **136**

12 Appendix F - List of publications **137**

Zusammenfassung

Die Schweiz verfügt über ein weit verzweigtes Netz von Strassen und Schienenwegen. Vielerorts hat dieses Netz seine Kapazitätsgrenzen erreicht oder bereits überschritten. Auf Grund des hohen Verkehrsaufkommens und des Alters der Bauwerke besteht an vielen Orten Instandsetzungsbedarf. Die Optimierung von Instandsetzungsmassnahmen hat eine grosse Bedeutung, um Kosten und Behinderungen des Verkehrs auf einem vertretbaren Niveau zu halten. Mehrere Methoden, die in der Geophysik weit verbreitet sind, haben ihre Entsprechung im Gebiet der zerstörungsfreien Prüfung (ZfP). Die wichtigsten Unterschiede zwischen der Erde und der Verkehrsinfrastruktur bestehen in der Grösse und den beteiligten Materialien. Die geringere Grösse von Verkehrsbauwerken erfordert eine Anpassung der geophysikalischen Methoden, wie beispielsweise bei Wellenverfahren eine Erhöhung der eingesetzten Frequenzen. Deshalb wird im Bereich ZfP Ultraschall an Stelle von Seismik verwendet. Im Bauwesen wird eine reiche Palette von Materialien eingesetzt. Dennoch bestehen einige wichtige Baumaterialien vor allem aus Gesteinen, wie beispielsweise Beton (Gesteine, Zement und Zusatzstoffe) oder Asphalt (Gesteine, Bitumen und Zusatzstoffe). Die Tatsache, dass Verkehrsbauwerke vor allem aus Gestein bestehen, ist ein Grund für die Verwendung geophysikalischer Methoden für deren Prüfung. Seit etwa 20 Jahren wird Georadar (Ground Penetrating Radar, GPR) für die zerstörungsfreie Prüfung von Verkehrsbauwerken eingesetzt. Wichtige Vorteile sind, dass das Verfahren sehr schnell ist und dass Untersuchungen kontaktfrei möglich sind. Dies ermöglicht die Verwendung von Messfahrzeugen, die auf grossen Objekten wie Brückenplatten eingesetzt werden. Solche Messfahrzeuge sind nützlich, um sowohl die Behinderung des Verkehrs, als auch die Kosten in einem vertretbaren Rahmen zu halten.

In dieser Arbeit beschreibe ich die Untersuchung von verschiedenen Verkehrsbauwerken mittels GPR. Dazu gehören beispielsweise Asphaltbeläge, Eisenbahnschotter, Brückenplatten oder Stützwände. Die unterschiedlichen Grössen und Formen dieser Bauwerke und die vielfältigen für sie relevanten Problemstellungen erfordern jeweils eine Anpassung der Vorgehensweise, um die gewünschten Informationen zu erhalten. Dies ist besonders sichtbar bei den Messungen, bezieht sich aber auch auf die Verarbeitung und Auswertung der gemessenen Daten. Ich zeige, dass Georadar ein wirksames Instrument für die Untersuchung von Verkehrsbauwerken darstellt. Für mehrere Anwendungen konnte ich die Genauigkeit und Zuverlässigkeit der Radarergebnisse durch einen Vergleich mit den Ergebnissen zerstörender Prüfungen analysieren und bestimmen und somit nachweisen, dass die Methode für vielfältige Problemstellungen geeignet ist. Ich zeige ausserdem, dass hoch entwickelte, neuartige Verfahren zur Datenbearbeitung die Auswertung erheblich unterstützen können. Durch einen Vergleich verschiedener Verfahren, angewendet auf einen hochauflösenden Datensatz, zeige ich deren Grenzen auf. Bis heute werden Georadar Untersuchungen vor allem durchgeführt, um den strukturellen Aufbau von Bauwerken abzuklären. Hier stehen beispielsweise Fragen nach der Dicke von Schichten oder der Position von Einbauteilen im Vordergrund. Materialeigenschaften, wie der Feuchte- oder Chloridgehalt, sind im Bauwesen jedoch eben-

falls relevant. In einem Laborexperiment konnte ich nachweisen, dass Feuchte- und Chloridgehalt einen deutlichen Einfluss auf das Radarsignal haben. Dieser Effekt ist so gross, dass er auch unter Feldbedingungen, wo zusätzliche Einflüsse eine Rolle spielen können, anwendbar sein sollte. Die gegenwärtigen Arbeiten konzentrieren sich auf eine Automatisierung des Messfahrzeuges und die Untersuchung von Materialeigenschaften.

Summary

Switzerland has an extensive network of roads and railway lines that has reached or exceeded its capacity at many locations. Due to large traffic volumes and the age of the network, there is a need for repair at many locations. Optimization of repair measures is of great importance for keeping the obstruction to traffic flow and the cost to a minimum. Several methods that are commonly used in solid earth geophysics have their counterparts in non-destructive testing (NDT). The main differences between the earth and transport infrastructure are the size and the materials involved. The reduced scale of the infrastructure requires an adaption of the methods, such as an increase in frequency for the wave methods. Thus, ultrasonics is used for NDT rather than seismics. The most important building materials used for transport infrastructure consist mainly of mineral aggregates, such as concrete (mineral aggregates, cement, additives) or asphalt (mineral aggregates, bitumen, additives). Soils and rocks are also mineral aggregates. Accordingly, it makes sense to use geophysics designed for studying the earth to study transport infrastructure. For about twenty years, ground penetrating radar (GPR) has been used for the non-destructive inspection of transport infrastructure. Important advantages of this method are that it is fast and can be used in a non-contact mode. This facilitates the use of mobile acquisition units that can operate on large structures, such as bridge decks. These units keep obstruction to traffic flow to a minimum and confine costs to an acceptable level.

In this thesis I describe GPR approaches for the inspection of various structures related to ground transport including road pavements, railway ballast, bridge decks or retaining walls. Due to the different shapes and sizes of the targets and because of the different problems related to them, the GPR method has to be adapted to deliver the required information. This is particularly apparent in the data acquisition, but is also true for data processing and data analysis. I demonstrate that GPR is a powerful tool for the inspection of transport infrastructure. For several applications the accuracy and reliability of GPR results are analyzed and defined with the help of ground truth. I prove that the method fulfils a wide range of requirements defined by civil engineers. I show that advanced methods, such as inversion or data fusion, can significantly support the analysis of GPR data. The limits of these approaches are also demonstrated via a comparison of different methods applied to a high resolution data set acquired on a concrete structure. Until today, most GPR inspections are carried out to obtain structural information, such as layer thicknesses or the position of fittings hidden beneath the surface. However, material properties such as moisture or chloride content can also be of interest in civil engineering. In a laboratory experiment, I demonstrate that chlorides and moisture have a significant effect on the GPR signal. This effect is large enough to be observed under field conditions, where additional factors are likely to affect the quality of GPR data. Current work is focused on the automation of a mobile acquisition unit and on the evaluation of material properties.

1 Introduction

1.1 Transport infrastructure in Switzerland

Transport infrastructure is one of the most important lifelines of modern societies and economies. The Swiss network of motorways and federal roads has a length of greater than 1700 km (Figure 1) with more than 220 tunnels and about 1100 bridges. The value of this infrastructure is estimated to be about 80 billion Swiss Francs (Geel and Bosch, 2009). Almost 6 million vehicles use this network every day (FEDRO, 2009). Most of the motorway network was built in the 60's and 70's of the last century. After 30-50 years of operation many structures are in need of repair. In 2009, investments of 2.2 billion Swiss Francs in the motorway and federal roads network were planned. Of this total, 965 million Swiss Francs were intended for the construction of new roads and 1.2 billion Swiss Francs for the expansion and repair of the existing network. In addition to the motorways and federal roads, there are cantonal and municipal roads leading to a total length of the Swiss road network of about 71000 km.

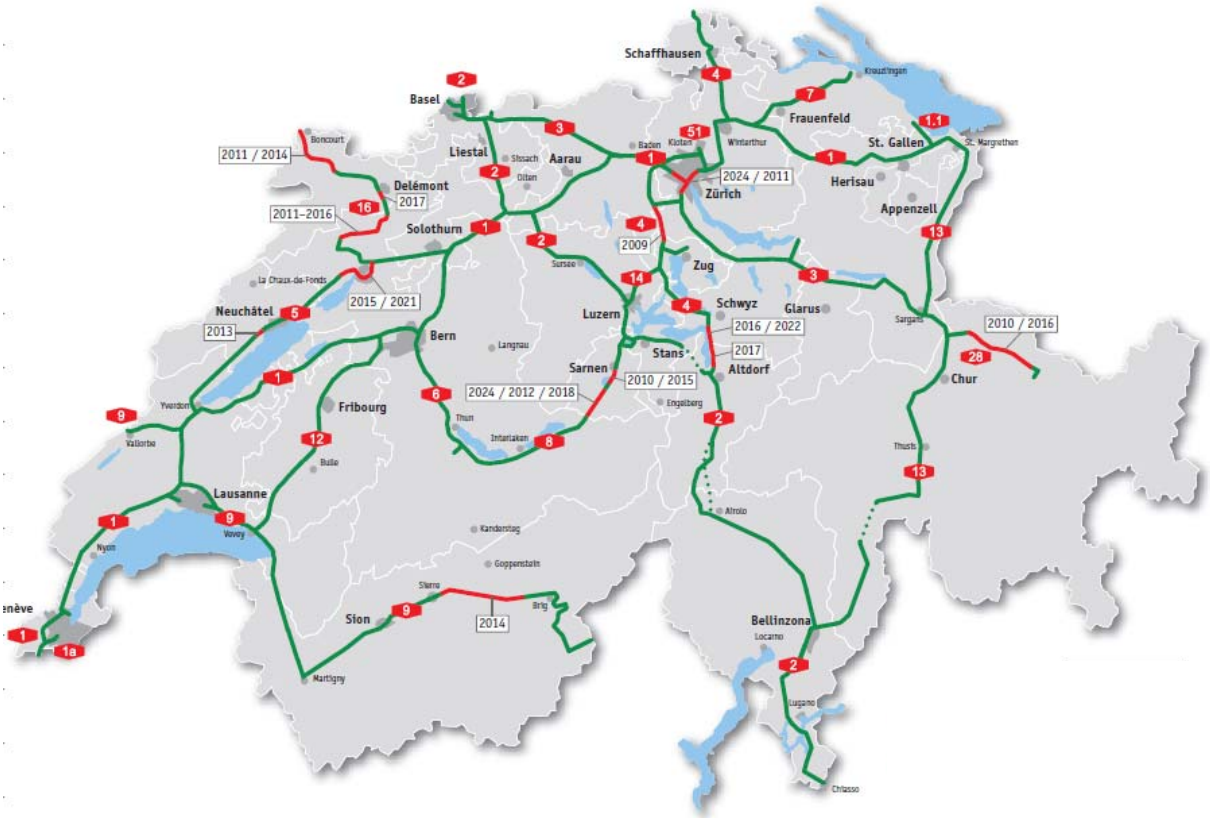

Figure 1: The Swiss motorway and federal roads network, currently in operation (green) and under construction/planned (red), from FEDRO (2009).

In many places, the motorway network has reached or exceeded its capacity. In Figure 2 yearly traffic jam hours for selected trouble spots are presented. Looking at the Zurich-Winterthur northern bypass, there were about 2500 hours of traffic jams in 2008. This means that during nearly one third of the time, there was a traffic jam on this stretch of motorway.

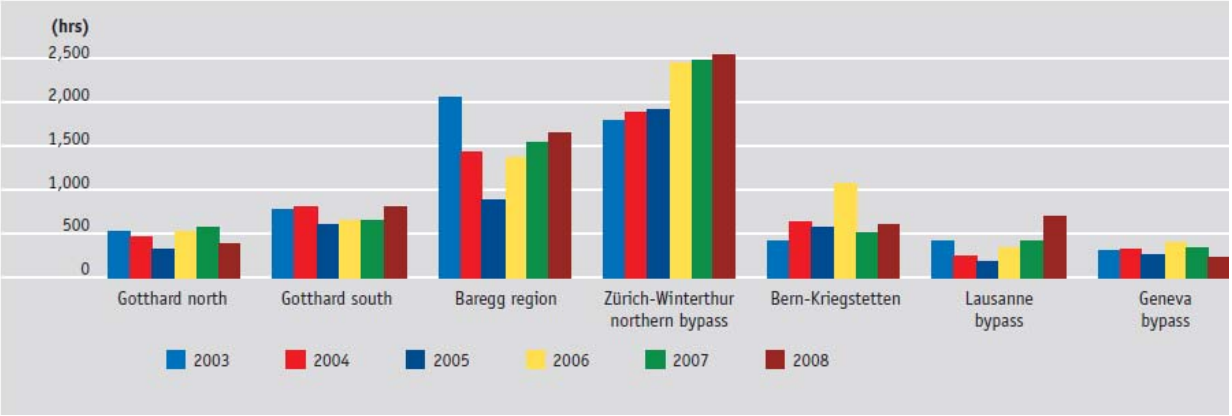

Figure 2: Traffic jam hours on selected trouble spots, from FEDRO (2009).

Swiss Federal Railways (SBB) is responsible for the planning, construction and maintenance of most of Switzerland's railway network. In addition, there are several smaller railway companies, such as BLS or RHB. The SBB network has a length of 3011 kilometers and transports 322 million passengers and about 54 million tons of goods per year (SBB, 2010). The traffic on the network is increasing constantly. In many places the capacity has been reached or is exceeded. In Figure 3 the average number of trains per day per kilometer on the SBB network is presented. On average, there were almost 93 trains per day per kilometer. There are 6027 bridges, 305 tunnels and 757 stations on the network (2008 figures). In addition, SBB owns about 170 km of sound insulating walls. From 2016, Swiss Federal Railways will operate the 57 km long Gotthard Base Tunnel, the longest tunnel in the world.

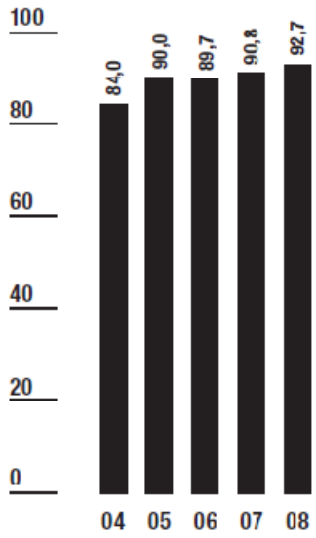

Figure 3: Trains per day per kilometer, from SBB (2008).

Many roads and railway lines in Switzerland are exposed to geohazards, like avalanches, landslides, rockslides etc. (Figure 4). This requires a large number of protective structures, such as retaining walls or avalanche galleries.

Figure 4: Rockfall on the Gotthard motorway (A2) during 2006, photograph from canton Uri (2010).

Typical examples of structures made of concrete and asphalt are concrete bridge decks and road pavements. There are many different designs for bridge decks. A common type (Figure 5) is a concrete layer covered with a layer of asphalt that has a thickness 0.04-0.08 m. Beneath the asphalt there is a sealing membrane consisting of a textile mesh, bitumen and additives with a thickness of about 0.005 m. The concrete surface is in many cases treated with primers or liquid sealings before the sealing membrane is added. The concrete has a thickness of about 0.3 m and is equipped with rebar. In many cases the rebar consists of several layers of steel mesh with single bars having diameters between 0.01 and 0.03 m. The dis-

tance between the rebar and the concrete surface is called the concrete cover (of rebar). Its size is relevant because if it is too small there is an increased risk of corrosion and if it is too big there may be static problems. Tendons are cables under high stress that are vital for the stability of the structure. They are encased in metal or plastic tendon ducts. The hollow space within the duct is grouted with cementeous material to ensure the transmission of forces between cable and concrete.

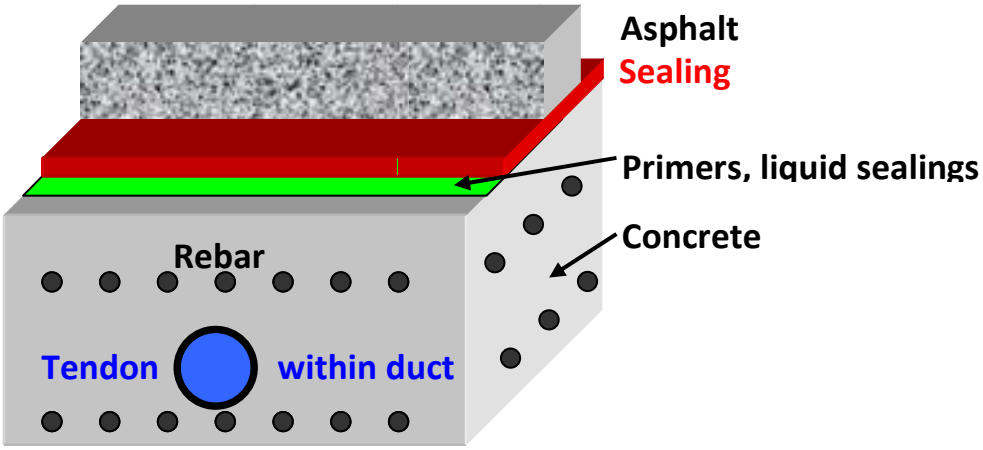

Figure 5: Concrete bridge deck.

Most concrete bridges are equipped with girders or girder boxes. Girders or girder boxes are in many cases fitted with tendons. An example in simplified form is presented in Figure 6, where the girder boxes are marked with red arrows.

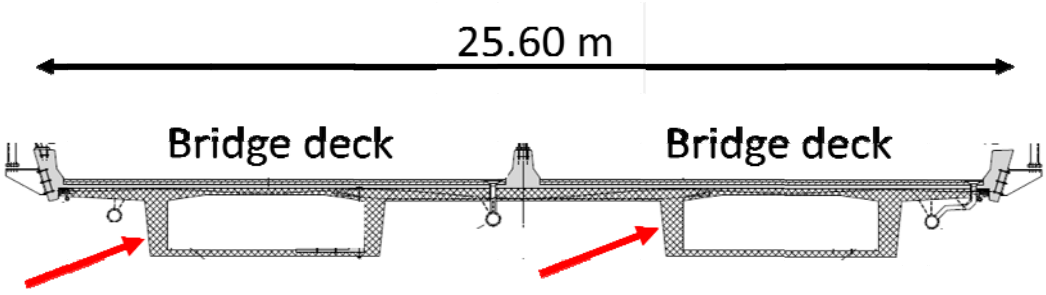

Figure 6: Concrete bridge (Sihlhochstrasse, motorway A3, Zurich) with girder boxes (arrows).

The design of road pavements in Europe is governed by European and national standards. Based on traffic loads and climatic conditions, different materials are used and pavement layers have different thicknesses. In Figure 7 the road and pavement structure for a high performance road according to Swiss standards is shown in simplified form. The thicknesses of layers may vary depending on the material used. From top to bottom there is a wearing

course with a thickness of 0.03 m followed by a base course and the road base with thicknesses of 0.07 m and 0.08 m, respectively. The top three layers are constructed of bituminous mixtures with increasing size of aggregates from top to bottom. The subbase, having a thickness of 0.11 m is in many cases stabilized with bitumen or cement. The capping layer consists of either soil or substituted material. Its thickness is not defined and it may be compacted and/or stabilized with cement or bitumen.

Definition	Thickness
1. Wearing Course	30mm
2. Base Course	70mm
3. Road Base	80mm
4. Subbase	110mm
5. Capping Layer	Not defined
6. Natural Ground	Not defined

Figure 7: Pavement and road structure of a high performance road according to Swiss Standards SN640430 and SN640302.

1.2 Geophysics and non-destructive testing of transport infrastructure

Several methods that are commonly used in solid earth geophysics have their counterparts in non-destructive testing (NDT). The main differences between the earth and transport infrastructure are the size and materials involved. The smaller scale of transport infrastructure requires an adaption of the geophysical methods. Accordingly, ultrasonics is used for NDT rather than seismics. The most important building materials used for transport infrastructure consist mainly of mineral aggregates, such as concrete (mineral aggregates, cement, additives) or asphalt (mineral aggregates, bitumen, additives). Soils and rocks are also mineral aggregates. Accordingly, it makes sense to use geophysics designed for studying the earth to study transport infrastructure.

Testing problems in civil engineering can be classified in different ways. With regard to the time of inspection, testing can be used for quality control of new structures, for the monitor-

ing of existing structures or for gaining information for the planning of repair work. The focus of inspections can be on structural information, such as layer thicknesses or positions of fittings (e.g. tendon ducts) or on material properties (e.g. chloride content in concrete or compaction of asphalt pavements).

Seismic–like methods

The acoustic emission method can be considered as small scale seismology, in which the sensors are mounted on a structure (e.g. a reinforced concrete bridge) for the monitoring of cracks or the rupture of single wires in tendons (Schechinger and Vogel, 2007; Yuyama et al., 2007). Ultrasonics using center frequencies between 50 and 300 kHz (Schickert et al., 2010; Krause et al., 2008) can be considered as high-frequency reflection seismics. It is used for the detection of fittings in concrete, the inspection of the thickness of structures and for locating voids and cracks. The terms A-Scan, B-Scan, C-Scan and SAFT (Synthetic Aperture Focusing Technique) used in ultrasonics correspond to trace, seismic section, time-slice and migration in reflection seismics. In Figure 8 an ultrasonic C-scan (time-slice) from a concrete test slab showing seven tendon ducts embedded in concrete is presented (Krause et al., 2008).

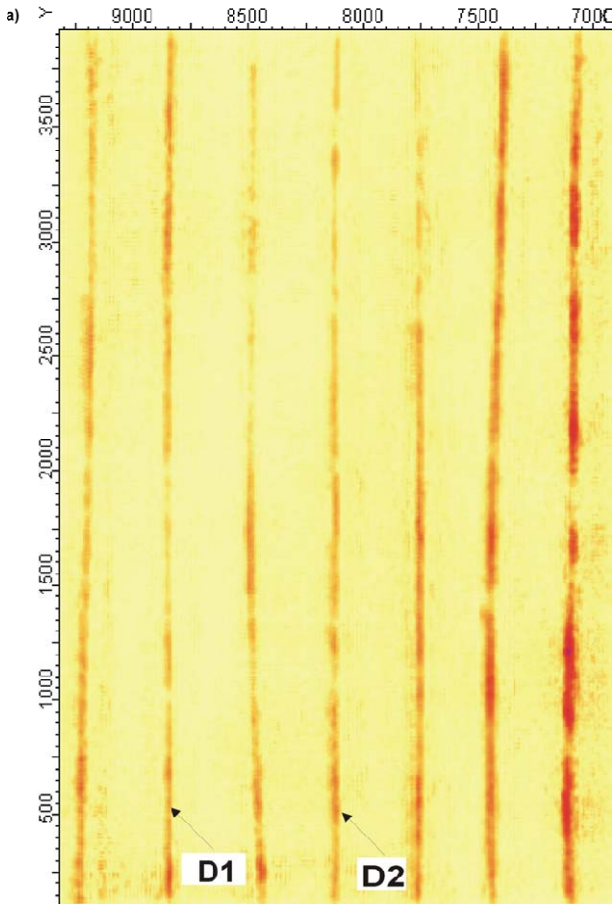

Figure 8: C-scan (time-slice), depth 0.08 to 0.21 m, from concrete specimen showing tendon ducts (from Krause et al., 2008).

Impact-Echo is another method based on mechanical waves. There, the receiver signal is transferred to the frequency domain for evaluation (Wiggenhauser, 2003). Several methods closely related to seismics are used for the testing of asphalt pavements. The falling weight deflectometer (FWD) is a mobile device (Figure 9) consisting of a variable weight that can be dropped from different heights, a loading plate for uniform force distribution, a load cell for measuring the applied pulse, one or several deflection sensors (most FWDs use geophones) and a system for recording and displaying the deflection data (NCHRP, 2008; ASTM, 2005a). The weight is dropped onto the loading plate and the deflection of the pavement caused by the impact is recorded. The basic idea of this test is to simulate a passing wheel load. The recorded data are used to evaluate the structural capacity of the pavement. The seismic pavement analyzer (SPA) and the portable seismic pavement analyzer (PSPA) (Figure 10) employ spectral analysis of surface waves (SASW) for the determination of material moduli and layer thicknesses in pavements (Baker et al., 1995; Nazarian and Milind, 1993; Yuan and Nazarian, 1993). The method is based on the construction of a dispersion curve for surface waves followed by inversion for stiffnesses. Changes in stiffness are attributed to different pavement layers. This method has been adopted and significantly modified in solid earth geophysics for near surface applications (Xia et al., 1999).

Figure 9: Falling weight deflectometer (FWD).

Figure 10: Portable seismic pavement analyzer (PSPA).

Electric and electromagnetic methods

GPR for NDT uses the same equipment as in geophysics, but in most cases with higher frequency antennas (Hugenschmidt and Kalogeropoulos, 2009) with center frequencies between 0.5 and 2 GHz. The self-potential method (Elsener et al., 2003) is used for investigating the corrosion of reinforcement steel in concrete. An example of a commercial self-potential unit is presented in Figure 11. DC electrical methods (Morris et al., 2002; Figure 12) are used for investigating humidity in concrete or other materials. Cover meters based on AC

electrical methods are widely used for the inspection of reinforced concrete, particularly for locating near surface metal structures such as rebars. There is a wide range of such equipment with various product names available on the market (Proceq, 2010; Elcometer, 2010; Hilti, 2010).

Figure 11: Self-potential equipment.

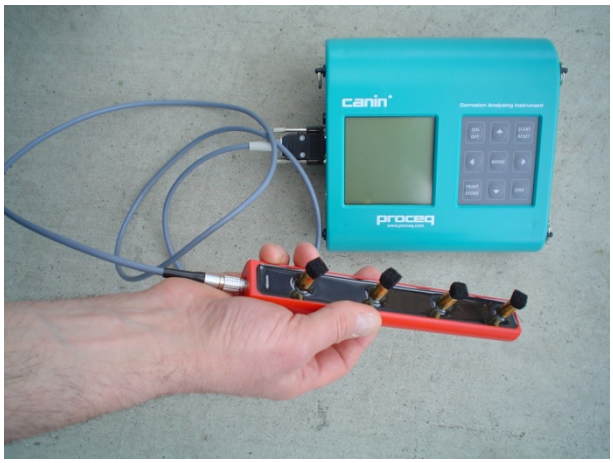

Figure 12: Resistivity equipment .

Other methods

A simple way of testing the concrete cover is using small magnets that either stick to a concrete surface or not which, together with the known diameter of the rebar, leads to estimations of the concrete cover.

Infrared thermography (IR) is a technique that operates in the infrared range of the electromagnetic spectrum. Cameras recording in this range are used to take single pictures or movies. IR is used for mapping the surface temperature of objects and, using this information, for detecting defects that influence temperature (e.g. delaminations or blisters). An example of a mobile system for IR inspections on large surfaces (e.g. bridge decks) is shown in Figure 13. The IR-camera (Agema THV 900LW, red arrow) is mounted at a height of 3.11 m. This leads to an image size of 1.21 m x 2.40 m. A GPS antenna (yellow arrow) is mounted on top of the camera. In a study carried out to evaluate the possibilities and risks of porous asphalt on bridge decks (Rodriguez et al., 2008), thermography data were recorded once per hour on one lane of the "Pont sur l'Arnon" on the motorway A5 near Yverdon, Switzerland. The aims of this campaign were to determine if the temperatures measured by stationary probes in the middle of the bridge were representative for the whole surface, to extrapolate the temperatures measured by the probes onto the whole surface and to compare between surface temperatures on and off the bridge. In Figure 14 the infrared emissions during 20 hours are displayed. The results are closely related to surface temperatures, but they are not necessarily identical because the infrared emissions also depend on the emissivity of the surface. This is shown in Figure 15 where the road-marking (arrow A) and the joint (arrow B) have lower infrared emissions. The IR survey proved that there are only minor temperature

variations on the bridge, which means that the stationary probes are representative and that there are no relevant temperature differences between on and off the bridge, even during a temperature drop from about 14^{o} C to about 2^{o} C.

Figure 13: EMPA's mobile IR-system.

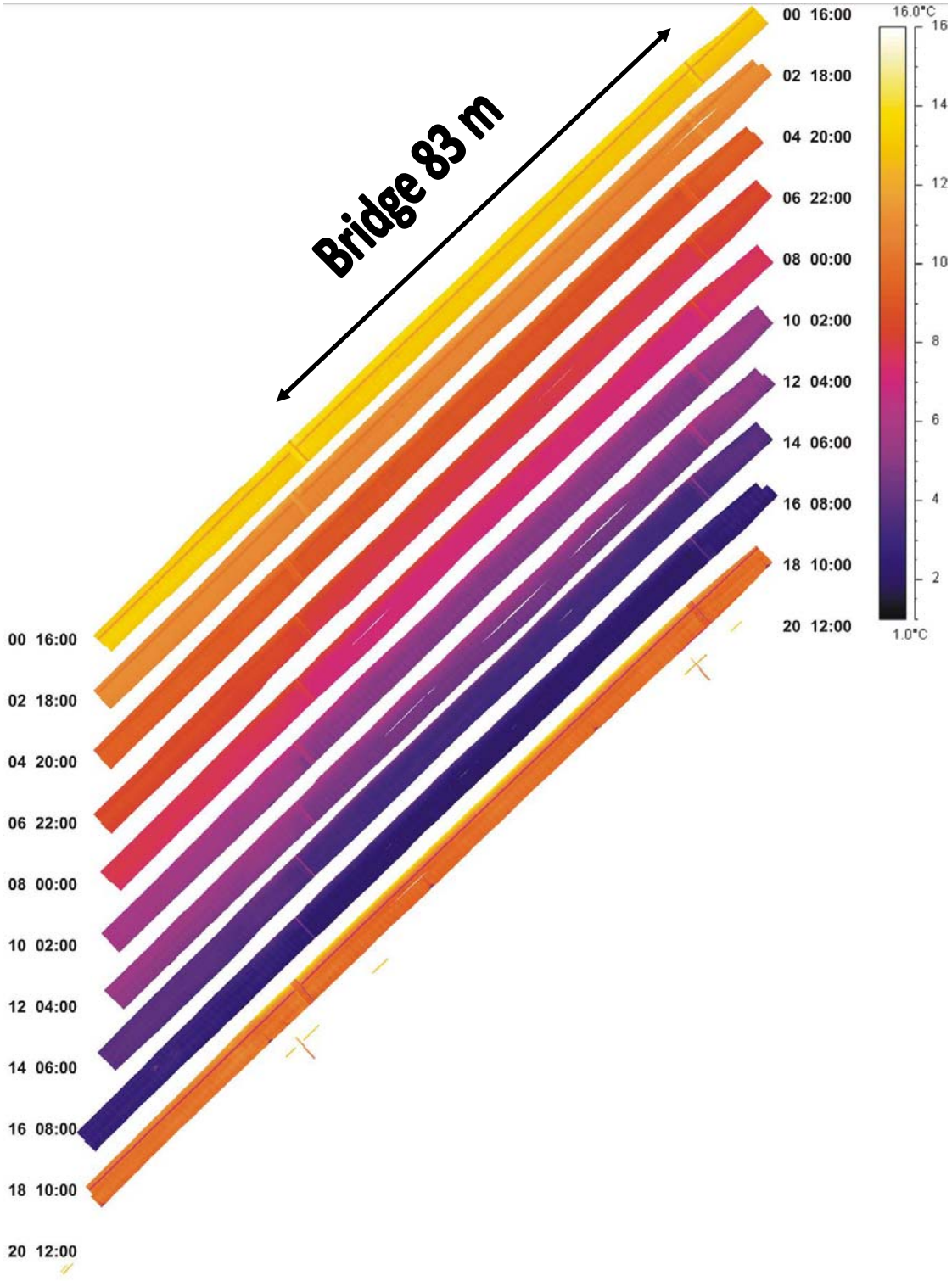

Figure 14: Surface temperatures during 20 hours.

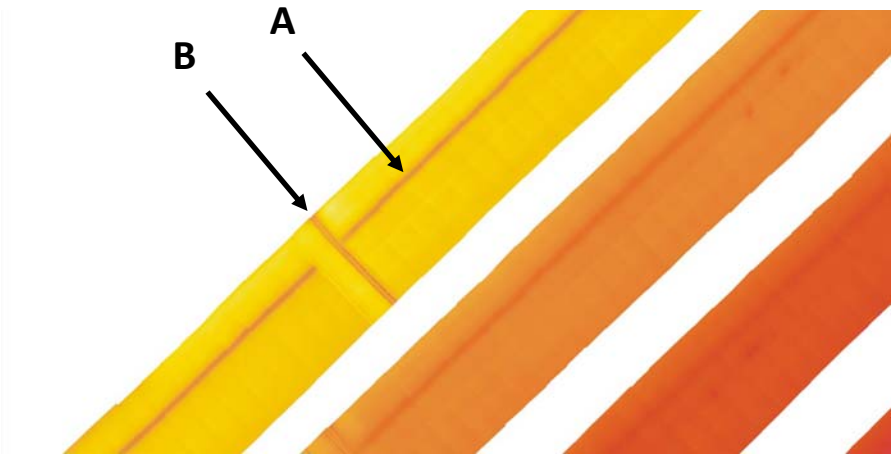

Figure 15: Surface temperatures, enlarged section, 4 p.m., 6 p.m., 8 p.m.

An overview of the relation of some geophysical methods to NDT ones is given in Table 1.

Table 1: NDT and Geophysical methods.

Geophysics	**NDT**	**Testing Problem in Civil Engineering**
Seismology	Acoustic emission	Crack propagation, long-term monitoring of structures
Seismics	Ultrasonics	Layer thicknesses, position of built-in components
Seismics	Impact-Echo	Layer thicknesses, position of built-in components
Ground penetrating radar	Ground penetrating radar	Layer thicknesses, position of built-in components, material properties
Self-potential	Self-potential	Corrosion of steel in concrete
DC electrical methods	DC electrical methods	Humidity
AC electrical methods	Cover meter	Position concrete cover and diameter of single rebars
Magnetics	Magnetics	Concrete cover of rebar
Heat flow	Infrared thermography (IR)	Defect detection, position of built in components, temperature control
Seismics	Falling-weight deflec-tometer	Structural capacity
Seismic surface waves	Seismic pavement ana-lyzer, portable seismic pavement analyzer	Elastic moduli and layer thicknesses

1.3 Ground penetrating radar

Radar principles

Ground Penetrating Radar (GPR) is an electromagnetic method. It is thus governed by Maxwell's equations (Maxwell, 1865; Crawford, 1968; Gerthsen et al., 1982), which can be written in their differential or integral forms:

Differential	Integral	
$curl\ \boldsymbol{H} = \boldsymbol{j} + \dot{\boldsymbol{D}}$	$\oint_{\delta A} \boldsymbol{H}\, d\boldsymbol{s} = I + \int_A \dot{\boldsymbol{D}}\, d\boldsymbol{A}$	[1]
$curl\ \boldsymbol{E} = -\dot{\boldsymbol{B}}$	$\oint_{\delta A} \boldsymbol{E}\, d\boldsymbol{s} = -\int_A \dot{\boldsymbol{B}}\, d\boldsymbol{A}$	[2]
$div\ \boldsymbol{D} = \rho$	$\oint_{\delta V} \boldsymbol{D}\, d\boldsymbol{A} = Q$	[3]
$div\ \boldsymbol{B} = 0$	$\oint_{\delta V} \boldsymbol{B}\, d\boldsymbol{A} = 0$	[4]

with volume V, area A, displacement current D, electric current I, electric current density j, electric charge Q, charge density ρ, magnetic field H, electric field E and temporal derivatives $^{\bullet}$. B and D are proportional to H and E respectively:

$$\boldsymbol{D} = \varepsilon\varepsilon_0\, \boldsymbol{E} \quad [5]$$

$$\boldsymbol{B} = \mu\mu_0\, \boldsymbol{H}. \quad [6]$$

Equation [1] is a generalized version of Ampère's law, in which an electric current and/or a time-varying electric field generate a magnetic field. The first part is the normal Ampère's law and the second part takes into account effective current flow (displacement currents) across insulators or dielectric media. Equation [2] is Faraday's law, which states that a time-varying magnetic field produces an electric field. The basis for equation [3] is that electric fields can begin and end on electric charges (for GPR ρ can be taken to be 0). Finally, equation [4] effectively states that lines of magnetic induction are continuous and there are no single magnetic poles where fields could terminate.

Several conclusions can be drawn directly from Maxwell's equations. Based on equations [3] and [4] it can be concluded that electromagnetic waves are transversal (B and D are orthogonal to the direction of propagation), because otherwise there would be temporal

sources and sinks (Figure 16), which is generally not consistent with equation [4] and in vacuum not with equation [3].

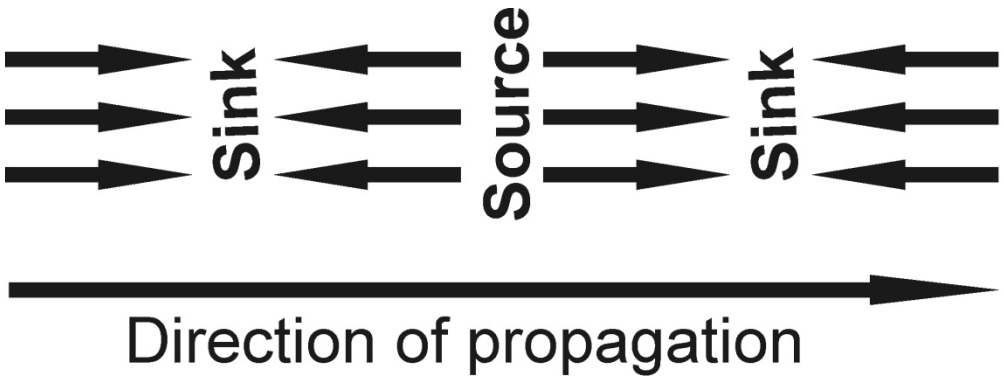

Figure 16: Sources and sinks in a longitudinal wave.

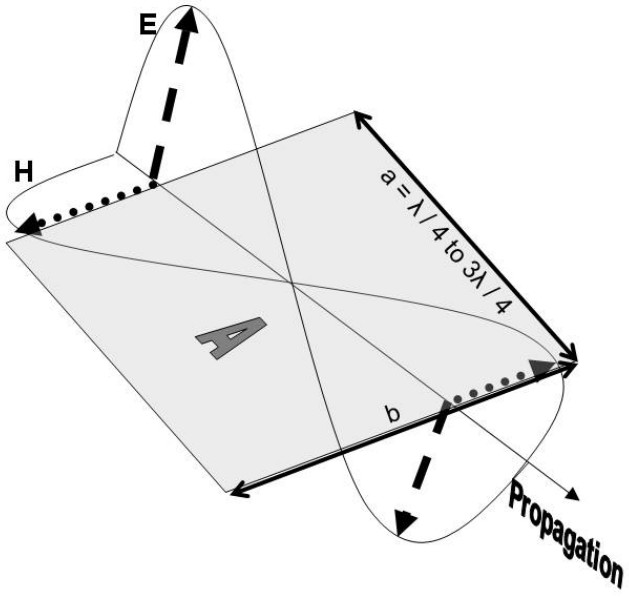

Figure 17: Electromagnetic wave with area A.

Another conclusion is that E and H are orthogonal to each other because of equation [1]. The integral of $\dot{D}$ over an area A (Figure 17) reaches its maximum value if A is orthogonal to $\dot{D}$. According to [1], the integral of H around the edges of area A will also reach its maximum value which implies that H is parallel to A and hence orthogonal to $\dot{D}$. Another important conclusion is that electromagnetic waves are travelling in vacuum with the speed of light. Substituting equation [5] in equation [1] and taking $I=0$ in free space gives

$$\oint_{\delta A} \boldsymbol{H}\, d\boldsymbol{s} = \int_A \varepsilon\varepsilon_0\, \dot{\boldsymbol{E}}\, d\boldsymbol{A}. \qquad [7]$$

Assuming a plane harmonic wave

$$E = E_0 \sin \omega\,(t - \frac{x}{v}), \qquad [8]$$

with direction of propagation *x*, velocity of propagation *v* and angular frequency ω. Assuming $t=2x/v$ equation [7] can be written as

$$\oint_{\delta A} \boldsymbol{H}\, d\boldsymbol{s} = \varepsilon\varepsilon_0\, E_0\, \omega \int_A \cos\ (\omega \frac{x}{\mathrm{v}})\, d\boldsymbol{A}. \qquad [9]$$

For the rectangular area A with sides b and a in Figure 17 and wavelength λ parallel to *a* (*a* extends from $\lambda/4$ to $3\lambda/4$), equation [9] can be written as

$$\oint_{\delta A} \boldsymbol{H}\, ds = b\, \varepsilon\varepsilon_0\, E_0\, \omega \int_{\lambda/4}^{3\lambda/4} \cos\ (\omega \frac{x}{\mathrm{v}})\, dx. \qquad [10]$$

Integration of equation [10] leads to

$$\left| \oint_{\delta A} \boldsymbol{H}\, d\boldsymbol{s} \right| = \left| b\, \varepsilon\varepsilon_0\, E_0 2\, \omega\, (\frac{\mathrm{v}}{\omega}) \right|. \qquad [11]$$

The absolute value sign will be omitted during the next steps. Using the fact that H and E are in phase, the left side of equation [11] can be written as

$$\oint_{\delta A} \boldsymbol{H}\, d\boldsymbol{s} = 2\, b\, H_0. \qquad [12]$$

The comparison of equations [11] and [12] leads to

$$H_0 = \varepsilon\varepsilon_0\, \mathrm{v}\, E_0. \qquad [13]$$

Starting with equation [2] and proceeding analogously to equations [5–13] it can be shown that

$$E_0 = \mu\mu_0 H_0 \text{ v.} \qquad [14]$$

Substituting [14] into [13] leads to

$$\text{v} = \frac{1}{\sqrt{\varepsilon\varepsilon_0\mu\mu_0}} \cdot \qquad [15]$$

In a vacuum ($\mu=\varepsilon=1$), equation [15] can be written as

$$\text{v} = \frac{1}{\sqrt{\varepsilon_0\mu_0}} = 3 \cdot 10^8 \frac{m}{s} = speed\ of\ light\ c. \qquad [16]$$

For materials in which the GPR method is applicable, it can be assumed that $\mu \approx 1$ (in ferromagnetic materials this is not valid but ferromagnetic materials can not be investigated with the GPR method) and hence

$$v = \frac{c}{\sqrt{\varepsilon}} \cdot \qquad [17]$$

This means that the signal velocity within materials is mainly defined by its relative permittivity. For practical purposes it can be assumed that relative permittivities of materials are in the range 1 (air) to 84 (water), which leads to signal velocities between $3 \cdot 10^8$ m/s (air) and $0.33 \cdot 10^8$ m/s (water). The high velocity of the GPR signal is responsible for one of the main advantages of GPR. As the signal travels with such a high velocity, a single measurement takes very little time and therefore the potential number of measurements per second is extremely high.

If an electromagnetic wave hits an interface, part of the energy will be transmitted and part will be reflected. For a plain electromagnetic wave in a low loss material hitting at vertical incidence an interface between two materials with relative permittivities ε_1 and ε_2, the reflected wave can be described as

$$Reflected\ wave = R\ \cdot Incident\ wave, \qquad [18]$$

with the reflection coefficient

$$R = \frac{\sqrt{\varepsilon_1} - \sqrt{\varepsilon_2}}{\sqrt{\varepsilon_1} + \sqrt{\varepsilon_2}}. \qquad [19]$$

Clearly, there would be no reflection if $\varepsilon_1 = \varepsilon_2$ (materials with identical relative permittivities) and the reflection amplitude becomes negative (phase shift by 180 degrees) if $\varepsilon_2 > \varepsilon_1$.

The time that a GPR signal requires to travel through a material layer, get reflected and travel back through the layer is

$$t = \frac{2\ \cdot d}{v}, \qquad [20]$$

where d is the thickness of the layer. The velocity v, necessary to compute depths or thicknesses from t is a priori unknown. It can be estimated using experience or velocity tables, calibrated by comparison of t with known thicknesses or by special setups during GPR data acquisition. Equation [20] is valid only if the distance between transmitter and receiver is zero or small enough to be neglected.

The ability of the GPR or any wavefield-based method to separate single objects (i.e. the lateral resolution) is limited by the size of the Fresnel zone, which characterizes the area where reflected waves add together constructively. Single points within this area cannot be distinguished by the GPR signal. The radius of the Fresnel zone is described approximately by

$$r = \sqrt{\frac{d \cdot v}{2f}} \qquad [21]$$

with frequency f. A larger Fresnel zone corresponds to a lower resolution. Thus, lateral resolution increases with frequency and decreases with the depth of the target.

Equipment

Today, a wide range of GPR equipment from different manufacturers is available. A GPR system consists of one or several antennas, a central unit usually including a monitor for real time data display and accessories, such as cables and an energy supply. Most systems that are available on the market work in the time domain. There are systems that work in the

frequency domain, usually referred to as stepped frequency systems, but in a commercial sense those systems are not very relevant. All data presented in this thesis were recorded with a system working in the time domain.

Antennas

The frequency content of the emitted and recorded GPR signal is mainly defined by the antenna. As a general rule of thumb it can be said that the higher the center frequency of the antenna, the better the resolution but the lower the depth of penetration of the GPR signal and the possible depth of investigation. This means that the choice of the appropriate antennas is crucial for the success of GPR investigations. Today, antennas with center frequencies between several MHz (low resolution and high depth of penetration for geological applications) and several GHz (high resolution and low depth of penetration for non-destructive testing) are available. Antennas can be monostatic (transmitter and receiver at fixed distance usually in the same box) or bistatic (transmitter and receiver as separate units). Depending on the antenna type and characteristics, antennas are coupled to the object or used in a non-contact mode (e.g. horn antennas). The data presented in this report were acquired using the following GSSI (Geophysical Survey Systems Inc., Salem, NH, USA) antennas:

Table 2: Antennas

Model	Nominal center frequency*	Remarks
4205 horn	2.5 GHz	
2600	2.6 GHz	
5100	1.5 GHz	Off-the-shelf
5100	1.5 GHz	Purpose built with transmitter – receiver rotated by 180 degrees for CMP measurements
3101D	900 MHz	
5103	400 MHz	

* as provided by manufacturer

The model 4205 horn antennas were purchased in 1995 as 2.5 GHz antennas (manufacturer's specification). To examine this specification a laboratory test was carried out. The antennas were hung on opposing strings with a distance between the antenna casings of 0.31 m (Figure 18). One antenna was used as the transmitter and the other as the receiver. Data were recorded, Fourier-transformed and stacked. The result is shown in Figure 19. The center frequency is far below 2.5 GHz at about 1.2 GHz.

Figure 18: Experimental setup.

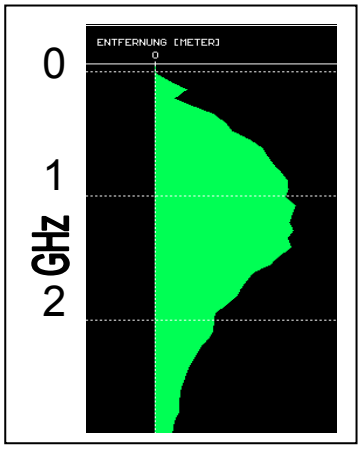

Figure 19: Frequency content of the model 4205 antennas.

Central acquisition unit

Central acquisition units have one or several channels for using one or several antennas at the same time. The possible data acquisition rate (number of measurements per second) depends mainly on the central acquisition unit and can reach up to several hundred measurements per second. Data storage and real time display are other tasks performed by the central unit. Data can be processed in real time for enhanced displays. The data presented in this thesis were acquired with two different GPR units. Between 1995 and 2001 a GSSI SIR-10A was used and since 2002 a GSSI SIR-20 has been in operation.

Accessories

Since GPR is a fast and potentially non-contact method, it can be used for the inspection of large structures, such as roads or bridges. In this context, knowledge of the position of each measurement is essential. Modern surveying equipment such as GPS or automated theodolites (Lehmann, 1999) provide the means for efficient position control.

The following description focuses on the approach used on bridge decks with an RTK (real-time-kinematic) GPS system. The equipment used consists of two Trimble model 5700 receivers (one for the base station and one for the acquisition vehicle; Trimble, 2001a), two GPS antennas, two radios for the connection between the base station and the receiver on the acquisition vehicle and a Trimble TSCe controller (Trimble, 2001b) for data display, data storage and control of the GPS data acquisition. The example used for this description is the inspection of the Felsenauviadukt, a 1116 m long bridge on the A1 motorway near Berne. The GPR inspection had to be carried out over the whole length of the bridge along parallel lines with a distance of 1.0 m between lines. For the navigation and position control on the

bridge, groups of 22 points with a distance of 1.0 m within each group and 100 m between groups were provided by the construction department of canton Berne (Figure 20).

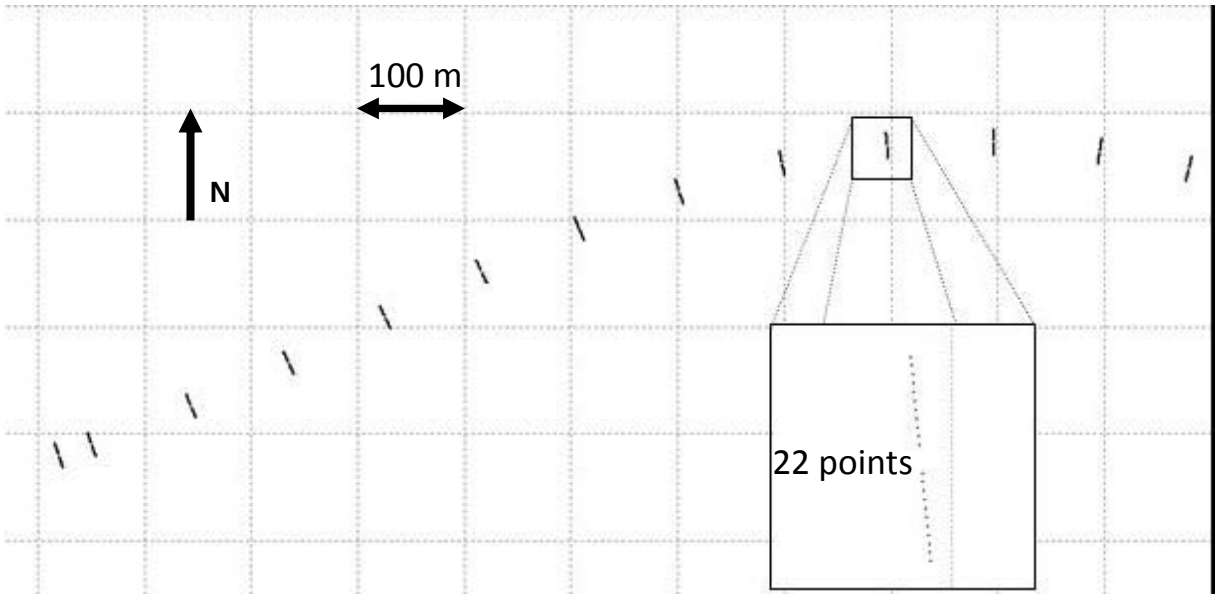

Figure 20: Groups of 22 points as provided by the construction department of canton Berne.

In order to allow navigation in between the groups, lines were interpolated and stored on the GPS-controller (Figure 21 and Figure 22).

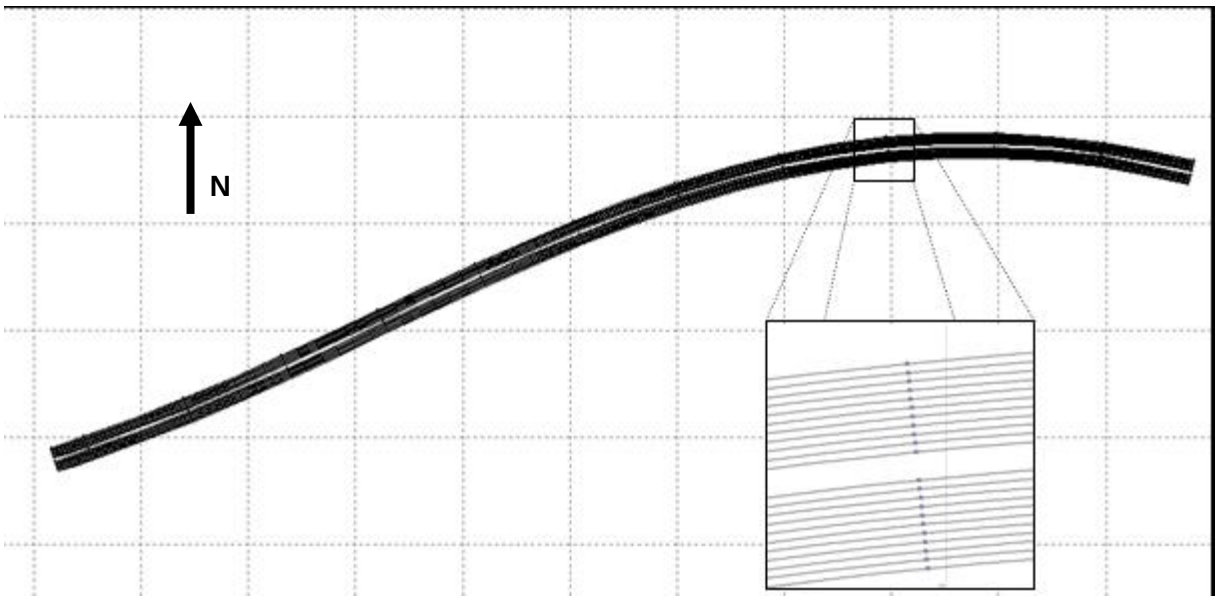

Figure 21: Lines interpolated between groups.

Figure 22: A single line displayed on the GPS-controller.

Figure 23: The GPS antenna centered above the horn antennas.

During data acquisition on the bridge, the GPS-controller was used in the vehicle to control and correct the GPS antenna position with respect to the interpolated lines. As the relevant position is that of the GPR antennas, the GPS antenna was centered above them (Figure 23). Position data were recorded continuously to document the precision of the positioning (Figure 24).

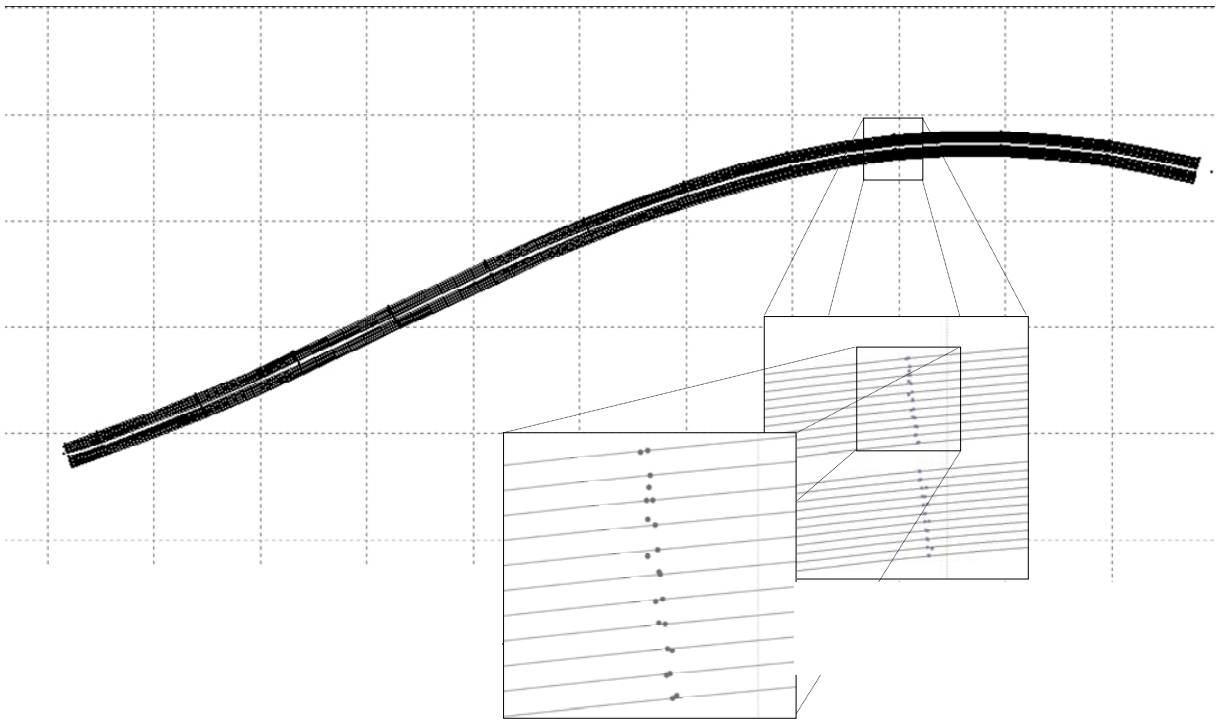

Figure 24: Actual vehicle positions during data acquisition compared to interpolated lines.

Data acquisition is only one step of a GPR survey. The other steps involve data processing and interpretation. The availability of appropriate software is essential for performing these steps satisfactorily. Unless stated otherwise, the data presented in this thesis were processed and displayed with various versions of the REFLEXW software package (Sandmeier, 2010).

1.4 GPR and non-destructive testing of transport infrastructure, with emphasis on contributions of the author

I have been involved in the development and application of GPR methods for approximately 15 years while working with EMPA (Swiss Federal Laboratories for Materials Science and Technology). To demonstrate my scholarship in this regard prior to officially commencing the PhD thesis, I have included 3 papers that were published in international journals between 1998 and 2002 in appendices B to D. The main part of the submitted thesis comprises 4 papers published between 2006 and 2010 that constitute chapters 2 to 5. In the following, I attempt to put my scientific contributions since 1998 into context. I briefly review how each of the problems was either identified or addressed by others and then mention my own contributions.

Ulriksen (1982) described the application of GPR to problems in civil engineering (locating pipes and cables, detecting of salt damage in concrete). He concluded that GPR can be used for the detection of damaged zones in concrete by evaluating the reflection amplitude at the concrete surface and that pipes can be located and pipe leakage detected. During the Strategic Highway Research Program (SHRP) that was authorized by the U. S. Congress in 1987 as a five year research program to combat the deteriorating conditions of highways, studies on non-destructive testing of asphalt pavements were carried out. One of the resulting reports (Smith and Scullion, 1993) described the development and calibration of a GPR system for the assessment of asphalt pavements. In addition, Maser (1994) described the application of GPR for the testing of asphalt pavements. Reflection amplitudes were used to obtain the dielectric permittivities of pavement layers, which were then used to determine layer thicknesses. A comparison between GPR and coring thicknesses demonstrated an accuracy of ± 8% for surveys without calibration cores and ± 5% for surveys with calibration cores. Originally, the reflection amplitude-based approach for calibration was suggested by Roddis et al. (1992) and criticized by Parry and Davis (1992) as being based on assumptions that are not valid under field conditions. A very limited amount of GPR data was shown in these earlier reports. Hugenschmidt et al. (1998, Appendix B - GPR inspection of a mountain motorway in Switzerland) describe a GPR inspection of a Swiss motorway. They present GPR data from different motorway sections, such as in tunnels, on bridges and on pavements before and after repair.

Swiss Federal Railways (SBB) inspect their railway lines at regular intervals. The first step of track renewal planning is a geotechnical study focusing on ballast thickness, on subsoil material penetrating into the ballast and on geotechnical properties of subgrade and subsoil materials. Until the mid-nineties of the last century, the inspection was mainly achieved by digging trenches at evenly spaced intervals and in locations of special interest. Taking into account the fact that the Swiss railway system has in many places reached or exceeded its capacity (SBB, 2008), this approach has seemed more and more inappropriate. Göbel et al. (1994) investigated the influence of various parameters on GPR signal velocity in railway ballast. Depending on the ballast condition they found velocities ranging from 0.8 to $1.2 \cdot 10^8$ m/s for soiled ballast and from 1.2 to $2.1 \cdot 10^8$ m/s for clean ballast. From a practical point of view, the use of a constant GPR signal velocity for depth and thickness estimation would be desirable. In a pilot study commissioned by Swiss Federal Railways (Hugenschmidt, 2000b, Appendix C - Railway track inspection using GPR), it is demonstrated that a constant GPR signal velocity of $1.4 \cdot 10^8$ m/s results in satisfactory accuracy for the ballast thickness estimates. In addition, it is proved that subsoil material penetrating into the ballast can be reliably detected.

Most of Switzerland's motorways were built between 1960 and 1980. Many motorway bridges have reached an age where repair work is necessary. For planning such work, detailed knowledge of the bridge is essential. On the other hand, traffic has risen to a level where obstruction to traffic flow and road or lane closures should be kept to a minimum. This situation has led to increased interest in methods capable of providing detailed informa-

tion at affordable cost and with reduced obstruction to traffic. In a series of case studies Hugenschmidt (2002, Appendix D - Concrete bridge inspection with a mobile GPR system) shows the practical application of the GPR method for the inspection of motorway bridges using a mobile data acquisition system.

The accuracy and reliability of GPR results on concrete bridges is an important issue, particularly for civil engineers who are responsible for the planning of repair and reconstruction projects. Today, there are standards (ASTM, 2005b) and guidelines (DGZFP, 2008) available for NDT. However, the choice of equipment, of acquisition parameters and particularly the interpretation of GPR data are the responsibility of the team carrying out the GPR survey. They can have a crucial influence on the quality of the results. Unfortunately, an assessment of this quality under realistic circumstances is in most cases impossible or restricted to few points. Laboratory experiments (e.g. Watanabe et al., 2003) provided information on the accuracy of inspections carried out under controlled conditions, but their value is limited for estimating the quality of results under field conditions. To evaluate the accuracy and reliability of GPR results on bridge decks under realistic conditions, Hugenschmidt and Mastrangelo (2006, Chapter 2 - GPR inspection of concrete bridges) initiated and carried out appropriate research. GPR inspections were carried out on five bridges designated for demolition. The results were made public before the bridges were dismounted. During and after demolition, the GPR results were verified with the help of the bridge parts where parameters such as the concrete cover of rebar were measured directly. In addition, a statistical analysis was carried out on the GPR data acquired during a survey that aimed at estimating the position of tendons in a bridge deck. This leads to information on the reliability and accuracy of GPR results on concrete bridges under field conditions.

Corrosion of reinforcement is a main cause of structural concrete deterioration and is therefore responsible for a large share of the cost for repairing concrete structures (Guettala and Abisi, 2006). This is not only a major problem in countries where structures are in contact with sea water, but also in countries where salt is applied to roads for de-icing. Periodic visual inspections of concrete structures carried out periodically are an established method for monitoring their condition. Moreover, there are accepted methods based on the self-potential method for detecting active corrosion in reinforced concrete (Van Deveer, 1975; Elsener et al., 1993). However, bridge decks covered with asphalt pavements are not accessible for visual inspection or self-potential measurements. Moreover, in most cases probing is very restricted due to traffic. As a result, maintenance planning for bridges is usually based on experience rather than on measured data. A method for detecting zones of increased chloride content and/or moisture is desirable in order to enable a better planning of repair work with respect to costs and scheduling. GPR has been suggested as a possible inspection method for condition assessment of bridge decks by several authors (Cardimona et. al., 2000; Scheff and Chen, 2000; Roberts, 2002; Shin and Grivas, 2003; Barnes and Trottier, 2004). Most of these studies were carried out on actual bridges. The conclusions from different studies were inconsistent, ranging from promising to discouraging. A laboratory experiment focused on the detection of chlorides and moisture in concrete only and excluding

other effects such as delamination is described by Hugenschmidt and Loser (2008, Chapter 3 - Detection of chlorides and moisture in concrete structures with ground penetrating radar). Using nine concrete specimens with different controlled chloride and moisture contents, they demonstrate that chlorides and moisture have a significant influence on GPR amplitudes.

In hilly countries, numerous retaining walls are needed along roads and railway lines. Although GPR inspections of various concrete structures have been frequently reported, limited literature was available on the inspection of retaining walls. Hugenschmidt and Kalogeropoulos (2009, Chapter 4 – The inspection of retaining walls using GPR) describe the data processing and interpretation of GPR data acquired on two walls using an apparatus especially developed for this purpose. A standard approach and an advanced approach are presented with the benefits and limitations of both options being presented.

Inversion and data fusion can significantly support and improve the evaluation of GPR and other NDT data. During inversion, a numerical model is adjusted until it produces a model output that is consistent with a measured data set. Data fusion combines data from different sources into a single composite data set. The sources can be different GPR antennas, different polarizations or different methods (e.g. GPR and ultrasonics). Kohl et al. (2003) described the fusion of GPR data with different polarizations and a combination with ultrasonic data. Langenberg et al. (2006) described a theory of modelling and imaging using electromagnetic and elastic waves for the non-destructive testing of concrete. Capizzi and Cosentino (2008) investigated different dipole configurations in experimental tests using long objects in a homogeneous medium. The application of an inverse scattering algorithm to GPR data was suggested by Soldovieri et al. (2006, 2007, 2009) and Solimene et al. (2007). A practical application of standard data processing, data fusion and inversion is demonstrated by Hugenschmidt et al. (2010, Section 5 – Processing strategies for high-resolution GPR concrete inspections). Two data sets acquired with different antenna polarizations on a concrete structure are treated with different strategies. In addition, it is shown that the concrete structure acts as a low-pass filter. A comparison of results obtained with different processing strategies demonstrates that advanced techniques offer considerable advantages for near surface structures. However, for greater depths, the low-pass characteristics of the concrete becomes the limiting factor and the benefit of the advanced methods is reduced substantially.

2 GPR inspection of concrete bridges

Johannes Hugenschmidt and Roman Mastrangelo

Cement & Concrete Composites 28 (2006) 384–392

Abstract

Ground Penetrating Radar (GPR) has become an important method for the non-destructive testing of concrete bridges. Although there are standards and guidelines available today, the quality of results does not only depend on the object inspected but also on the qualification and experience of the team carrying out the radar survey. This situation is unsatisfactory for engineers that have to decide whether a radar survey is suitable to solve their problem.

EMPA has been active in the field of non-destructive testing of concrete structures for more than ten years. During this time, procedures for efficient data acquisition, processing interpretation and reporting have been developed. In addition, a large number of concrete structures has been inspected for research and services.

In a research project completed in 2005, radar inspections using the EMPA approach were carried out on bridges designated for demolition. Results were laid open before the bridges were taken down. After the demolition radar results were verified with the help of the bridge parts. Thus, the accuracy and reliability of radar surveys was quantified under realistic circumstances.

Keywords: Concrete bridges, non-destructive testing, ground penetrating radar

Introduction

Ground Penetrating Radar (GPR) has become a valuable tool for the non-destructive testing of concrete bridges. Today there are standards (ASTM, 2005c) and guidelines (DGZFP, 2008) available. However, the choice of equipment, the setup of acquisition parameters and particularly the interpretation of radar data are within the responsibility of the team carrying out the radar survey and have a crucial influence on the quality of the results. Unfortunately, an assessment of this quality under realistic circumstances is in most cases impossible or restricted to few points. Laboratory experiments (Watanabe et al., 2003) provide information on the accuracy of inspections carried out under controlled conditions but their value is limited for estimating the quality of results under real field conditions.

This situation is unsatisfactory for engineers that have to decide whether a radar survey is suitable to solve their problem. In order to evaluate the accuracy and reliability of radar results on bridge decks under realistic circumstances, EMPA has carried out a research project sponsored by the Swiss Federal Roads Authority. Radar inspections were carried out on five

bridges designated for demolition. Results were laid open before the bridges were taken down. During and after demolition radar results were verified with the help of the bridge parts where parameters such as the concrete cover of rebar were measured manually with a ruler. In addition, a statistical analysis was carried out on radar data acquired during a survey aiming at the position of tendons in a bridge deck. This paper summarizes the results published in the research report (Hugenschmidt, 2005).

Radar principles

Ground Penetrating Radar is an electromagnetic investigation method. It is also known as Surface Penetrating Radar or Electromagnetic Reflection Method. Mostly it is used in reflection mode where a signal is emitted via an antenna into the structure under investigation. Reflected energy caused by changes in material properties is recorded (Figure 25) and analysed.

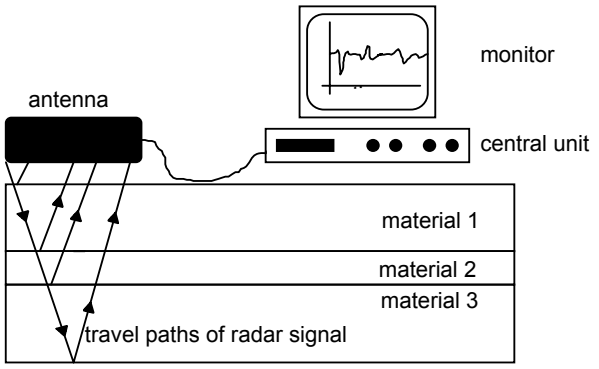

Figure 25: Radar principles.

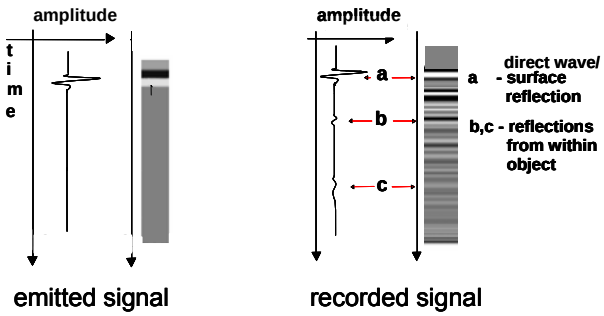

Figure 26: Emitted and recorded signal.

A sketch of the emitted and recorded signal in wiggle and grey scale mode is presented in Figure 26. The signal recorded is usually referred to as a scan or a trace. The vertical axis is a time axis, its length in non-destructive testing of concrete bridges is typically less than 30 nanoseconds (ns). In order to obtain depths the signal velocities in the different materials under investigation have to be known. There are several different ways to obtain these velocities. In the examples presented below signal velocities were defined by a comparison between radar data and borehole information.

Radar data can be displayed in different ways. In all the examples shown below data are displayed in grey scale mode with two different configurations, as radargrams and as time slices. Radargrams consist of a large number of traces lined up according to their acquisition position as sketched in Figure 27 where the antenna is moved in the X-direction recording data continuously. The radargram presented in Figure 28 represents a data set acquired

along a line in the x-direction. The horizontal axis corresponds to the length in the x-direction and the vertical axis is a time axis.

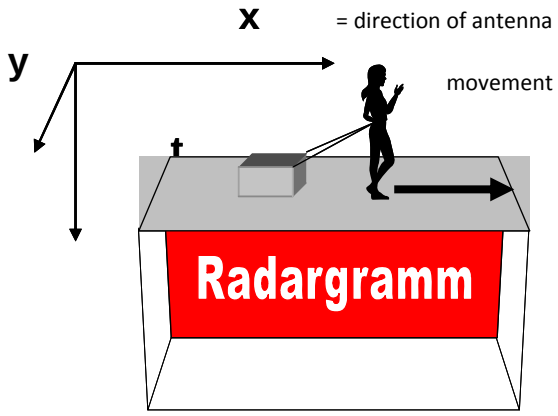

Figure 27: Schematic sketch of a radargram.

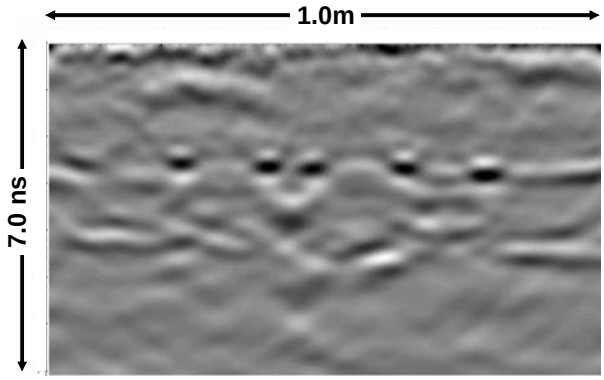

Figure 28: Example of a radargram from concrete floor.

When data are acquired not only along single lines but covering a whole area, for example by measuring along many parallel lines, slices from different times/depths can be plotted (

Figure 29). The time slice presented in Figure 30 corresponds to the data acquired on a surface along several parallel lines. Only signals recorded during a defined time-window are shown. Thus, the two axis correspond to the surface on which data were acquired.

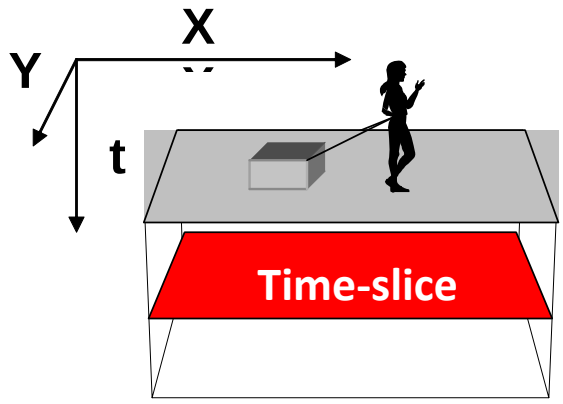

Figure 29: Schematic sketch of a time slice.

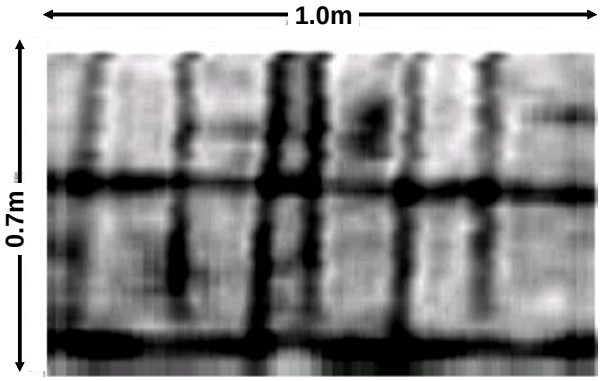

Figure 30: Example of time slice from concrete floor.

Daniels (2004) gives a detailed description of the concepts of Ground Penetrating Radar and its application on various problems from different fields of work.

Data acquisition

Obviously, when inspecting bridge decks or other large structures, the use of a mobile acquisition system is advantageous because of the reduction of acquisition time and the reduced obstruction to traffic flow. In Figure 31, EMPA's mobile acquisition system is presented. It consists of a GSSI SIR-20 system, GSSI model 4205 horn antennas and additional equipment such as a survey wheel or additional antennas that can be mounted if required. A Trimble model 5700 RTK system is used for controlling the position.

Figure 31: EMPA's mobile acquisition system for pavements and bridge decks.

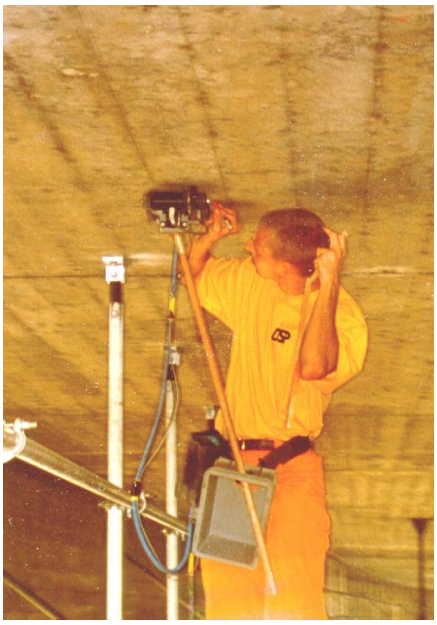

Figure 32: Manual data acquisition on bottom side of bridge deck.

If the use of the mobile acquisition system is not possible, data have to be acquired manually. In Figure 32, a GSSI model 5100 antenna is moved manually over the bottom side of a bridge deck for the detection of tendon ducts.

An overview of set-ups used for the examples presented in this paper is shown in Table 3. The center frequencies listed are the result of investigations at EMPA. Two antennas (transmitter, receiver) of the same type were placed opposite to each other in air. The signal recorded with the receiver antenna was Fourier transformed and stacked in order to obtain the frequency range and center frequency (Hugenschmidt, 2000a).

Table 3: Acquisition parameters for examples presented.

Nr.	Application	Acquisition mode	Antenna type; center frequency*	Traces/meter; samples/trace	Data processing during data acquisition
1	Wyssenried bridge	Mobile, 10 km/h	GSSI Model 4205 horn; 1.2 GHz	200; 512	none
2	Ramp Sihl flyover	Mobile, 10 km/h	GSSI Model 4205 horn; 1.2GHz	40; 512	none
3	Bridge deck, tendons	Manual	GSSI Model 5100; 1.2 GHz	300; 512	Bandpass filter, Gain
4	3-D survey on concrete girder	Manual	GSSI Model 5100; 1.2 GHz	400, spacing between acquisition lines 0.02 m; 512	none

*as defined by the author's group

Processing

Data processing is an essential step within a radar survey. The optimal processing sequence depends on the radar data, the object under inspection and the problem to be solved by the radar survey. Some common aims of data processing are:

- Improvement of signal/noise ratio
- Correction of surface reflection to time/depth zero
- Migration (correction of the position of reflection energy that has been reflected sideways)
- Gain correction (amplification of signals depending on traveltime)

An example of a simple processing sequence applied to data acquired on an industrial railway track embedded in concrete is presented in Figure 33 to Figure 38. The length of the Chapter shown is 3.0 meters, the vertical time scale is 12 nanoseconds. The application of a bandpass filter (Figure 34) results in this example only in a minor improvement of the signal/noise ratio. The correction of the surface reflection to time zero (Figure 35) introduces the surface of the object under inspection as a reference plane for future depth calculations. It is also a necessary step before applying migration (Figure 36), a processing step correcting the position of energy that has been reflected sideways. Migration is also referred to as Synthetic Aperture Focussing Technique (SAFT). Gain correction (Figure 37) results in an amplification of energy reflected at greater depth.

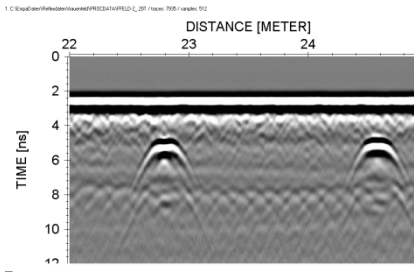

Figure 33: Raw data before processing.

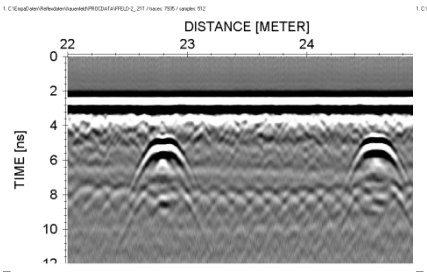

Figure 34: Data after bandpass filtering.

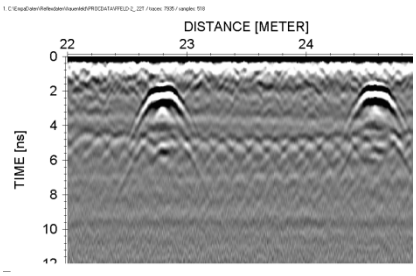

Figure 35: Data set after correction of surface reflection to time zero.

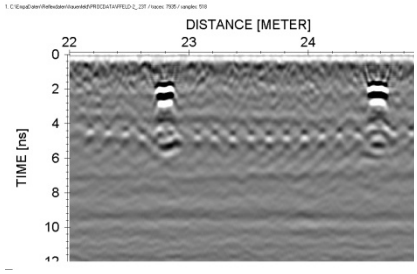

Figure 36: Data set after Migration.

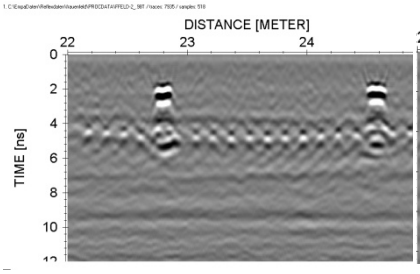

Figure 37: Data set after gain correction.

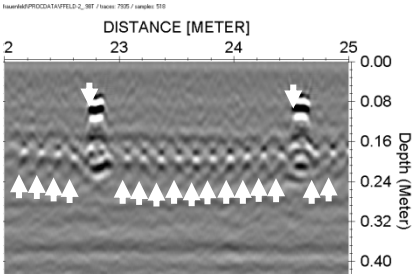

Figure 38: Processed data set with interpretation.

In general it can be stated that the processing of radar data has many similarities to the processing of seismic and ultrasonic data. A comprehensive description of the techniques used in seismic data processing can be found in Yilmaz (1987).

Interpretation

During interpretation, reflections within radar data are related to physical structures within the object under inspection. Additional information such as building plans or borehole information is often necessary and always desirable to support the interpretation of radar data. In Figure 38 the original time scale has been transformed into a depth scale using an estimated signal velocity within concrete of 0.08 m/ns. The two reflections at around 0.1 m were interpreted as sleepers and marked with arrows pointing downwards. The numerous reflections between 0.18 and 0.20 m were interpreted as single bars of a layer of rebar and marked with arrows pointing upwards.

Accuracy and reliability of results

In Figure 39 a small bridge (Wyssenried bridge) is shown that had become redundant. Data acquisition was performed with EMPA's mobile GPR-unit. The acquisition parameters are

listed in Table 3 (Nr. 1). A data set after processing is shown in Figure 40. The horizontal axis is 25 m long and corresponds to the length of the bridge, the vertical axis has a length of 14 ns. The interpretation of the radar data and the calibration of the time to depth/thickness conversion were supported by one borehole. A schematic view of the interpretation of the reflections marked with white lines is shown in Figure 41. From top to bottom the reflections were interpreted as:

- Asphalt concrete interface
- Top layer of rebar
- Tendon duct
- Bottom of concrete slab

The radar result for the concrete cover of rebar using a constant signal velocity within concrete of v=0.082 m/ns is presented in Figure 42 (dashed line). Note that there are two gaps in the radar result, one at 4.0 m and one at 21.0 m due to the fact that the reflections from the top layer of rebar and the tendon duct are overlapping in these areas. After the bridge deck had been sawed (Figure 43), the concrete cover was measured manually with a ruler in distances of 1.0 m along the cut. The results of these manual measurements will be referred to as “reality” within this paper. The comparison between the results obtained by the radar survey (dashed line) and reality (solid line) is presented in Figure 44 together with the absolute differences (solid circles) between those two results. The general course of the concrete cover over the length of the bridge is mapped quite appropriately; the mean difference between the radar results and reality is 12 mm. However, it has to be mentioned that the maximum difference is 41 mm at 17.0 m.

Work on the other bridges has been carried out in accordance with the approach described above leading to an estimate for radar results for the concrete cover of the top layer of rebar. The mean difference between radar and reality for all bridges was 10 mm, ranging between 3 mm and 17 mm for single objects. A result for the concrete cover was obtained on 77% of the sections inspected. No result was obtained on 33% of the sections inspected. This is mainly due to zones with a small concrete cover of rebar leading to an overlap of the reflections at the top layer of rebar and the asphalt-concrete interface, interpretation uncertainty in complex environments (for example when reflections from tendons or other structures can not be clearly distinguished from rebar reflections) and on and near joints.

In addition, the signal velocities minimizing the absolute differences between radar and reality were computed for all objects. Those velocities which can be expected to be close to the true signal velocities are ranging from 0.058-0.104 m/ns.

On none of the five bridges included in the project, information on deeper layers of rebar was obtained when using the mobile acquisition unit.

Figure 39: Wyssenried bridge.

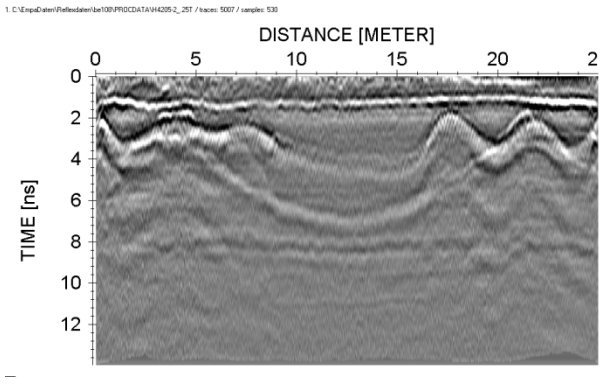

Figure 40: Data set from Wyssenried bridge.

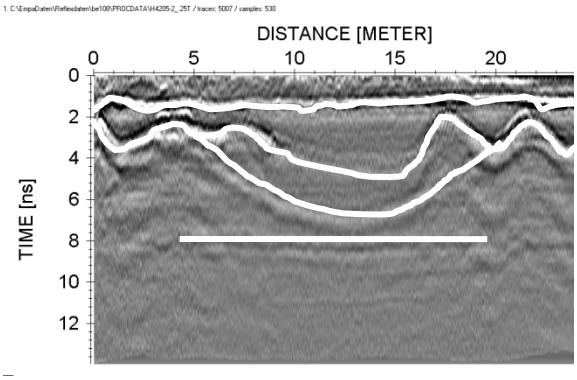

Figure 41: Data set with interpretation.

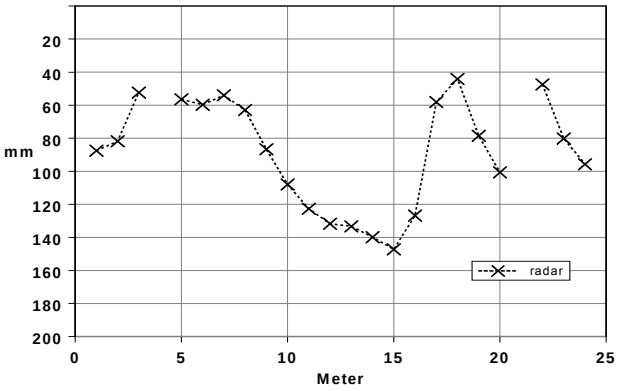

Figure 42: Radar result for concrete cover of top layer of rebar.

Figure 43: Sawed bridge deck.

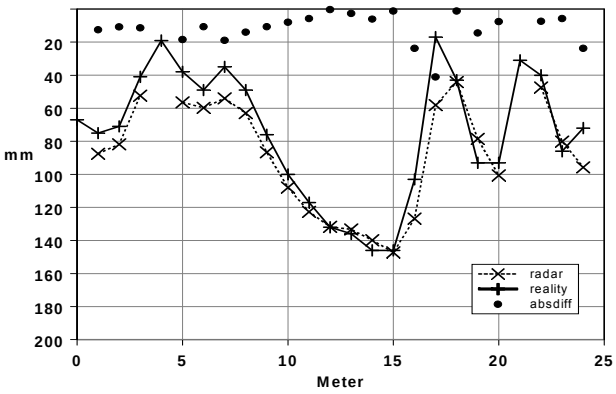

Figure 44: Comparison between radar result and reality for concrete cover of rebar.

The thickness of the asphalt pavement on concrete bridge decks is an important information for the planning of rehabilitation work and was therefore also included in this research project. On two of the bridges the pavement was removed with a milling machine (Figure 45) and in one case the pavement was opened along lines with an excavator (Figure 46) before the bridge deck was sawed. On two of the bridges a verification of the radar results for the pavement was not possible because the pavement had been removed before the radar survey or because it was destroyed with an excavator in an uncontrolled manner. The ramp of Sihl flyover (Figure 47) was a temporary structure that had been built to enable access during major rehabilitation work on the main structure and the ramps. Radar data on this structure were acquired with the mobile unit using the acquisition parameters listed in Table 3 (Nr. 2). A data set after processing is shown in Figure 48. The horizontal axis is 40 meters long. The reflection interpreted as resulting from the pavement-concrete interface is marked with a white arrow. The radar result for the pavement thickness using a constant signal velocity of v=0.143 m/ns is shown in Figure 49. The comparison between radar result (dashed line) and reality (solid line) together with the absolute differences (solid circles) is presented in Figure 50. The mean difference between radar and reality for the three bridges was 9 mm, ranging between 5 mm and 11 mm for single objects. A result for the thickness of the asphalt pavement was obtained on 95% of the sections inspected.

In addition, the signal velocities minimizing the absolute differences between radar and reality were computed for all objects. Those velocities which can be expected to be close to the true signal velocities are ranging from 0.117 and 0.143 m/ns.

Figure 45: Pavement removal with milling machine.

Figure 46: Pavement opening with excavator.

Figure 47: Ramp of Sihl flyover.

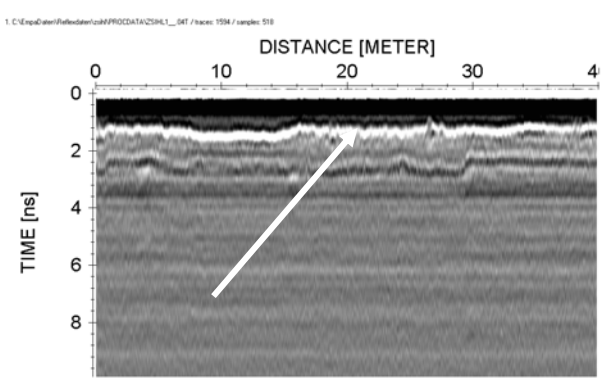

Figure 48: Data set from Sihl flyover ramp.

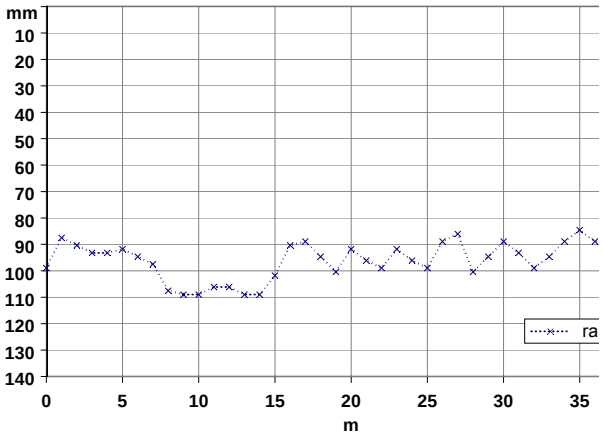

Figure 49: Radar result for thickness of asphalt pavement.

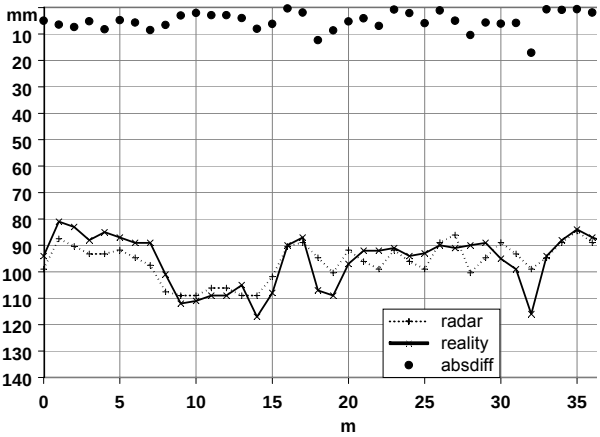

Figure 50: Comparison between radar result and reality for thickness of asphalt pavement.

A radar survey was carried out on the bottom side of a concrete bridge deck (Figure 32) to localize the position of tendons. Acquisition parameters are listed in Table 3 (Nr. 3). The length of the bridge was 1500 m and it had been put into service in 1974. The radar survey was carried out because the knowledge of the tendon positions was necessary for carrying out major rehabilitation work. Data interpretation was carried out on site in real time placing marks directly onto the concrete surface. As tendons were running orthogonal to the bridge axis, two lines parallel to the bridge axis were inspected. In order to evaluate the accuracy of the radar results a statistical test was carried out on 9 sections with a total length of 105 m. A comparison of tendon positions between the two parallel lines led to a mean difference of 0.05 m.

In Figure 51 two sections, each 5.0 m long from parallel lines are presented. Tendon positions are marked with vertical arrows. Please note that those positions are identical to those

marked in real time onto the concrete. Obviously the distance between tendons is varying and not constant as indicated in the building plans. One tendon was missed in the upper section.

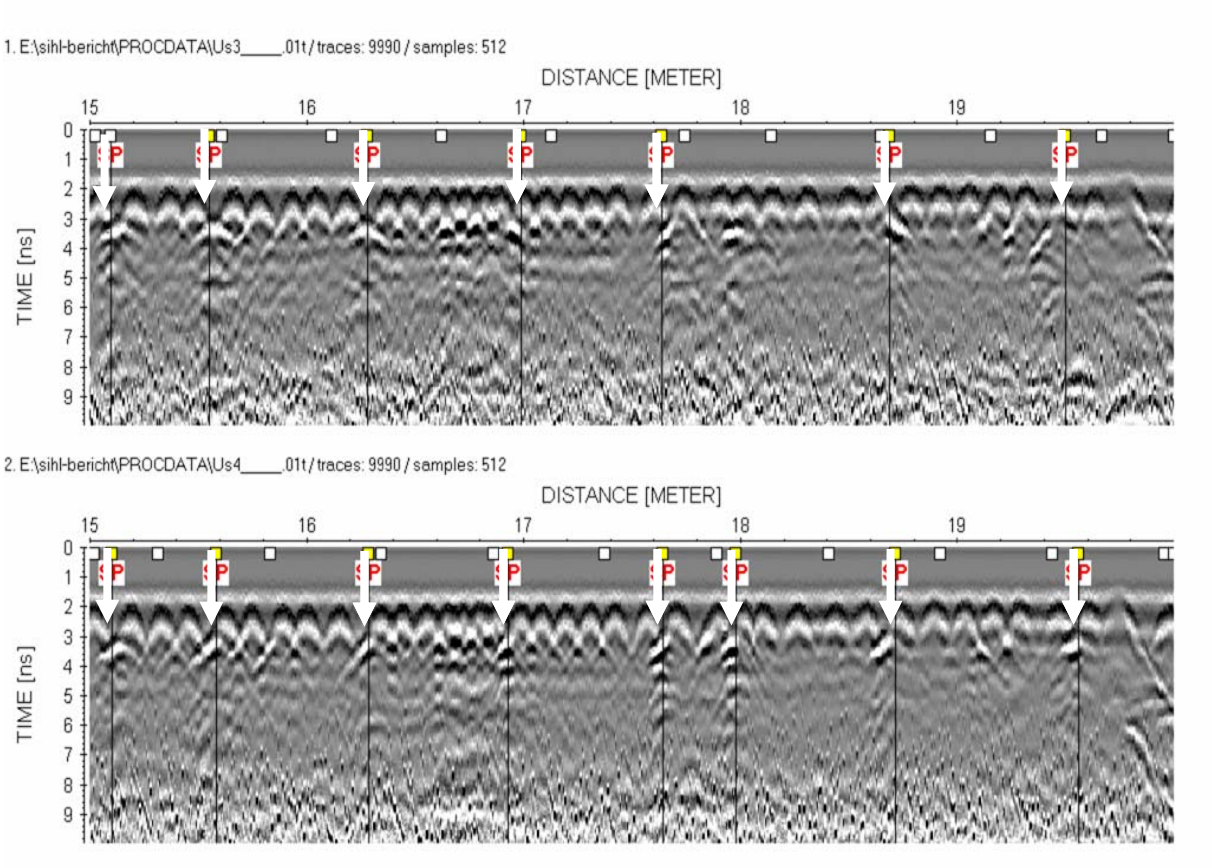

Figure 51: Two radargrams acquired on parallel lines.

3-D surveys

3-D surveys on concrete structures have the potential to reveal a detailed picture from the interior of concrete structures. In order to demonstrate this, a 3-D laboratory survey was carried out on a concrete girder (Figure 52) of a bridge that had been demolished. Data were acquired manually with parameters listed in Table 3 (Nr. 4) both along horizontal and vertical lines on the area marked in Figure 52. The cross section of the girder along the dotted line in Figure 52 is presented in Figure 53.

Data acquired in longitudinal and vertical direction were processed separately with a two-dimensional processing sequence. Figure 54 presents a time slice from the longitudinal data set at 0.51 ns corresponding to a depth of about 0.02 m. The dimensions of area shown in this and the following time slices are 8.05 m in the horizontal and 0.66 m in the vertical direction. Reflections from rebars orthogonal to the direction of data acquisition are clearly

visible. The time slice shown in Figure 55 is from 1.13ns corresponding to a depth of about 0.05 m. In addition to the reflection from the two tendon ducts running from top left to bottom right an additional nearly vertical reflection of unknown origin (white arrow in Figure 55) can be spotted. The time slice presented in Figure 56 from 2.15 ns corresponds to a depth of about 0.1 m. At this depth the reflection from the second layer of rebars can be seen between 1.4 m and 8.0 m. Please note that the bars in Figure 56 appear to be less focussed than those in Figure 54 due to the damping of the high frequencies of the signal. Also, there are no bars visible between 0.0 and 1.4 m because the girder is thicker there as can bee seen in Figure 53.

3-D data can provide a detailed insight into concrete structures. However, the acquisition of 3-D data sets is time consuming when using a single antenna. Antenna arrays (Eide and Hjelmstad, 2002) or automatic scanner systems (Taffe et al., 2003) can make the acquisition of 3-D data easier and thus encourage a wider use of 3-D techniques.

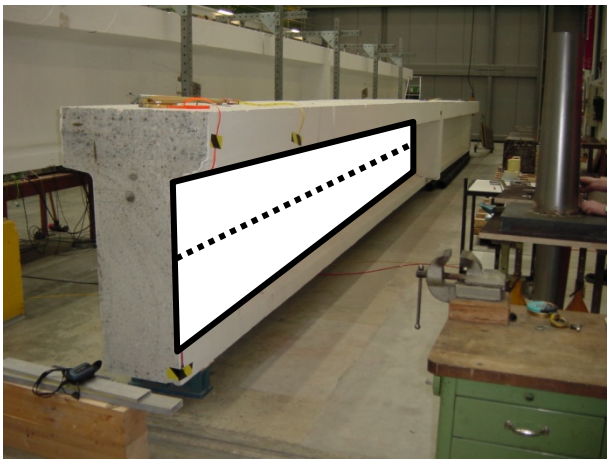

Figure 52: Bridge girder with marked acquisition area.

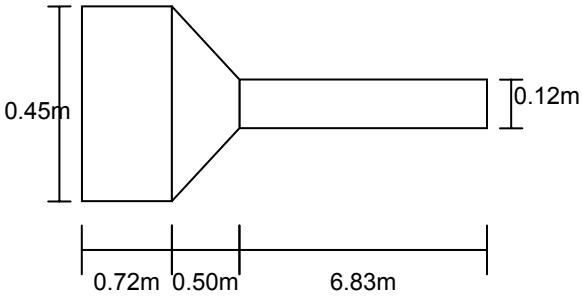

Figure 53: Cross section of bridge girder (not to scale).

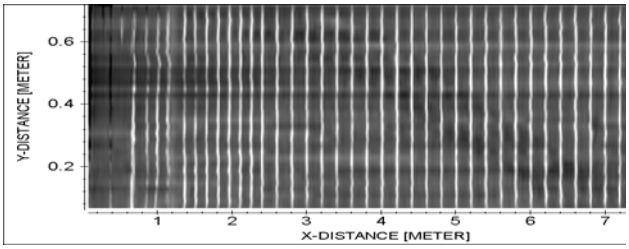

Figure 54: Time slice from 0.51 ns, depth approximately 0.02 m.

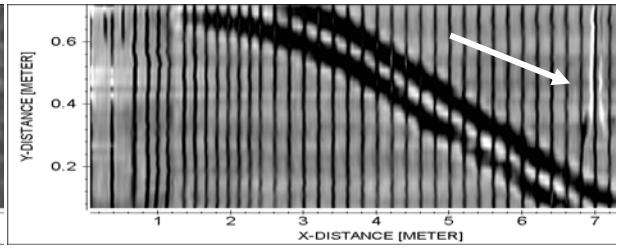

Figure 55: Time slice from 1.13 ns, depth approximately 0.05 m.

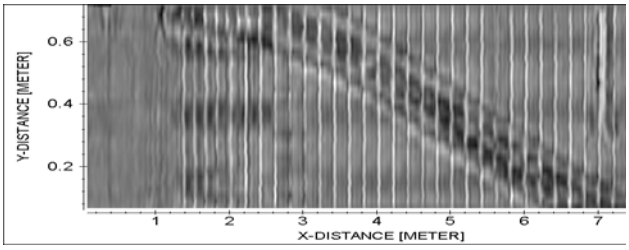

Figure 56: Time slice from 2.15 ns, depth approximately 0.1 m.

Conclusions

The concrete cover of the top layer of rebar was determined on 77% of the inspected sections. The mean difference between radar results and reality was 10 mm. In addition, the spacing between single bars was determined in many places. Gaps in the result for the concrete cover were mainly the result of resolution problems in sections with a small cover and of interpretation uncertainties in areas with additional structural complexity.

No information about deeper layers of rebar was obtained when the mobile acquisition unit was used.

The pavement thickness was determined on 95% of the inspected sections. The mean difference between radar results and reality was 9 mm. Gaps in the result for the pavement thickness were mainly due to a too small concrete cover resulting in overlapping reflections from bottom of pavement and rebar.

In addition to the signal velocities obtained with the help of the boreholes which were used for the computation of pavement thickness and concrete cover of rebar, signal velocities minimizing the absolute difference between radar results and reality were calculated. These velocities were varying between 0.058 and 0.104 m/ns for concrete and 0.117 and 0.143 m/ns for asphalt.

The positions of tendon-ducts in a bridge deck were determined with errors of less than 50 mm. The percentage of ducts that can be localized depends on the amount of effort and on the object under inspection.

3-D inspections provide a detailed insight into concrete structures. The use of antenna arrays or automatic scanner systems can encourage the wider use of 3-D techniques.

Acknowledgements

The project “Assessment of the condition of bridges with GPR” was sponsored by the Swiss Federal Roads Authority.

3 Detection of chlorides and moisture in concrete structures with ground penetrating radar

Johannes Hugenschmidt and Roman Loser

Materials and Structures 41 (2008): 785–792

Abstract

Corrosion of rebar within reinforced concrete is a major problem in countries where salt is applied to roads for de-icing. Concrete structures are periodically inspected in order to monitor possible damage caused by chloride induced corrosion of the reinforcement. However, bridge decks covered with asphalt pavements are not accessible for visual inspection and probing is limited. As a result, the planning of rehabilitation of bridge decks is usually based on a small number of probes. Consequently, the condition of bridge decks can only be assessed with low certainty. Therefore, a method enabling to study the conditions of concrete bridge decks covered by asphalt pavements is desirable.

This paper describes a laboratory experiment aiming at the investigation of the effects of moisture and chloride content on the amplitudes of radar signals. It can be shown that both, moisture and chloride content have a measurable influence on signal amplitudes. This may enable the future use of Ground Penetrating Radar for the planning of probing campaigns or for the extrapolation of results obtained at single probing points.

Keywords: bridge decks, chloride content, ground penetrating radar, corrosion, non-destructive-testing

Introduction

Under normal conditions, the reinforcement in concrete is protected from corrosion mainly due to the high pH-value of the pore solution. Under such conditions, a stable film forms on the steel surface which passivates the reinforcing steel and prevents the electrochemical processes taking place during corrosion (Pourbaix, 1996). However, this protective passivity layer can be destroyed due to carbonation of concrete or penetrating chlorides (Neville, 1995). As soon as a certain threshold value of chlorides is exceeded, the protective passivity layer on the steel surface is locally destroyed and, in combination with water and oxygen, corrosion of the reinforcement can take place (Montemor et al., 2003). There are two consequences of chloride induced corrosion of steel. Firstly, the products of corrosion occupy a volume several times larger than the original steel which results in cracking and spalling of the concrete cover. Secondly, due to the highly localized chloride-induced corrosion at a small anode, pitting of the steel takes place which reduces the cross-sectional area of the steel decreasing its load-carrying capacity (Neville, 1995). Corrosion of the reinforcement is

the main cause of structural concrete deterioration and is therefore responsible for a large share of the cost for the rehabilitation of concrete structures (Guettala and Abisi, 2006).

Chloride induced corrosion of rebar within reinforced concrete is not only a major problem in countries where structures are in contact with sea water but also in countries where salt is applied to roads for de-icing. Visual inspections of concrete structures carried out periodically are an established method to monitor their condition. Moreover, there are established methods based on the measurement of the potential of steel in concrete to detect active corrosion in reinforced concrete (Van Deveer, 1975; Elsener et al., 1993). However, bridge decks covered by asphalt pavements are not accessible for visual inspection or potential measurements and in most cases probing is very restricted due to traffic. As a result, maintenance planning for bridges is usually based on experience and not on data of the real condition of such decks. A method for detecting zones of increased chloride content and/or moisture is therefore desirable to enable a better planning of repair work with respect to costs and scheduling.

Ground penetrating radar (GPR) has been suggested as a possible inspection method for condition assessment of bridge decks by several authors. Cardimona et. al. (2000) mapped the degradation of the radar signal (loss in amplitude and/or increase in travel time) as an indication of whether or not the region above the rebar is compromised in some fashion. Scheff and Chen (2000) describe a comparison between GPR and chain drag results in a delamination survey on a concrete bridge deck and find that the results of the two methods do not fit very well. Roberts (2002) compares results of GPR deterioration surveys on several New Hampshire bridge decks with ground truth and conventional (destructive) survey techniques and finds that results compare favourably. Shin and Grivas (2003) evaluate the accuracy of condition assessments using GPR based on thresholds for the rebar reflection and dielectric permittivity and suggest multi-sensor fusion techniques to provide improved capabilities in assessing the condition of bridge decks. Barnes and Trottier (2004) provide a description of nine bridge deck deterioration surveys where radar data were searched manually for excess signal attenuation and reflectivity from the asphalt/concrete interface. Their comparison of the radar results with chain drag and half-cell potential results leads to the conclusion that GPR can present a viable option for estimating concrete deterioration repair quantities. Hugenschmidt (2005) describes the application of a method based on the damping of the signal within the concrete of a bridge deck in Switzerland possibly caused by increased moisture and chloride content. However, a verification of the results obtained was not possible as the bridge is still in service. Finally, radar equipment manufacturers (GSSI, 2006; Sensors & software, 2006) are promoting their products as a tool for condition assessment of bridge decks and an ASTM Standard (2005c) describes the detection of delaminated areas on bridge decks based on variations of the deck bottom echo.

This paper describes a laboratory experiment investigating the effects of moisture and chlorides in concrete on radar amplitudes. The changes of the quotient of reflection amplitudes

are evaluated as a possible approach for mapping problem zones on concrete bridge decks covered with asphalt pavements.

Experimental program

To study the influence of moisture and chloride content on radar amplitudes, nine concrete slabs were produced, each with dimensions of 0.90 x 0.75 x 0.08 m (Figure 57). Three concrete mixtures with maximum aggregate size of 32 mm, constant volume of paste (cement + water + NaCl) but differences in chloride content were used. The different chloride contents were 0.0, 0.4 and 1.0 mass-% chloride referred to cement content. The chloride was added as NaCl dissolved in the mixing water. A chloride content of 0.4% is the upper limit accepted under normal circumstances (temperature, ph-value, no prestressed structures, etc.) by Swiss experts. Workability of fresh concrete was determined with flow table test (EN 12350-5, 2001) and the pressure method was used for determining air content (EN 12350-7, 2001). All mixtures had comparable fresh concrete properties. The concrete was cast in three moulds per mixture. An overview of the nine specimens is presented in Table 4.

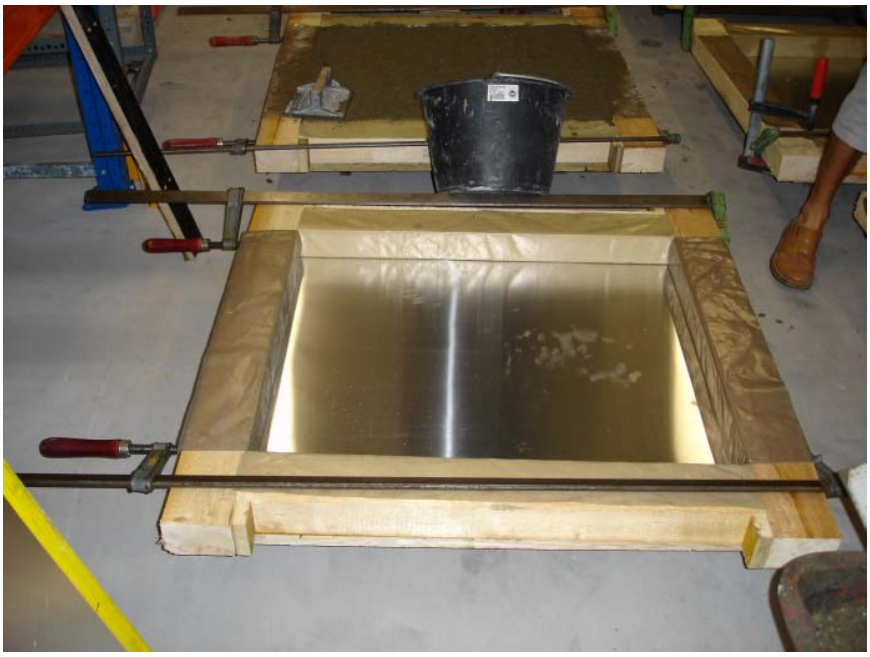

Figure 57: Mould for the production of the specimens.

Table 4: Storage, composition and workability of the different mixtures.

mixture [%]	storage [% r.h.]	aggregate [kg/m^3]	Cement CEM I 42.5 N [kg/m^3]	water [kg/m^3]	water/cement ratio [-]	NaCl [kg/m^3]	vol. of paste [l/m^3]	flow [cm]	air content [%]
0.0 Cl 0.0 Cl 0.0 Cl	35 70 90	1'937	310	155	0.50	0.00	254	43	1.0
0.4 Cl 0.4 Cl 0.4 Cl	35 70 90	1'937	306	155	0.50	2.02	254	44	1.1
1.0 Cl 1.0 Cl 1.0 Cl	35 70 90	1'937	301	155	0.51	4.96	254	44	1.0

The base of the mould was covered with an aluminium sheet simulating the reflecting reinforcement. After compaction, the specimens were stored at 20°C and 90% relative humidity (r.h.) for two days. Afterwards, the four sideboards of the mould were removed and one specimen of each mixture was moved to climates of 35% r.h., 70% r.h. and 90% r.h. until the radar measurements were carried out. Additionally, two prisms (360 x 120 x 120 mm) of each mixture were produced and stored at 20°C and 90% r.h.

There are differences between the slabs produced for the laboratory experiments and the situation on a real bridge. On bridges there is no aluminium sheet but a layer of rebar consisting of separate bars. The use of an aluminium sheet reduces the sensitivity of the experimental results to variations of the antenna position and orientation during radar data acquisition. As this is a desirable simplification of the experiment it was decided to use an aluminium sheet instead of single bars. On bridge decks, chlorides and moisture will rather penetrate into concrete during the life-span of the structure than being added during concrete production or absorbed during hydration. The experimental equivalent of the situation on bridge decks would be a mature specimen that is exposed to a chloride solution. However, this would introduce several factors such as concentration of chloride solution or duration of exposition that are difficult to estimate. In addition, chloride profiles in several locations would be necessary to control the progress of water and chlorides within the concrete. It was therefore decided to simplify and accelerate the experiment by adding the chloride to the mixture and storing the specimens at different relative humidities. The results of the concrete testing suggest that this simplification is acceptable.

At different concrete ages (up to 127 days), the change of weight of the nine slabs was determined by weighing. This change in weight is caused by the absorption (90% r.h.) and loss of water (70% and 35% r.h.) and therefore it is an indicator for change in moisture content of the concrete. In order to characterize the concrete of the three mixtures, compressive strength was measured on prisms at the age of 28 days according to EN-12390-3 (2002). Furthermore, one core sample (68 mm in diameter) was taken from each slab after 136 days in order to determine compressive strength.

Radar data were acquired 99 days after the production of the specimens. The acquisition parameters are shown in Table 5.

Table 5: Data acquisition parameters.

Radar unit	GSSI SIR-20
Antennas	GSSI model 4205 horn
Antenna height above specimen	0.25 m
Data processing during acquisition	none

The model 4205 antennas were chosen as they are part of EMPAs's mobile radar acquisition system for asphalt pavements and bridge decks. As the signal of the model 4205 antennas is known to drift, the radar unit with the antennas connected was switched on one hour before the start of the actual data acquisition. In addition, data were acquired on a metal plate before and after the measurements on each specimen. The antennas were placed in the center of the specimens and in four locations close to the center to avoid edge effects. Data were acquired in continuous mode while the antennas were left stationary above the specimens. A photograph of the radar antennas placed above one of the specimens during data acquisition is shown in Figure 58.

Figure 58: Antennas positioned above specimen during data acquisition.

Results and discussion

As it can be seen in Figure 59, compressive strength of the concrete after storage of 28 days at 90% r.h. is decreasing with increasing chloride content. The maximum decrease is 10% (in relation to the maximum value).

The differences in w/c-ratio and cement content (Table 4) are too small to explain the variations in compressive strength. Since the main systematic difference of the three mixtures is chloride content (same mix design, same storage), chlorides in fresh concrete directly affect compressive strength in a negative manner.

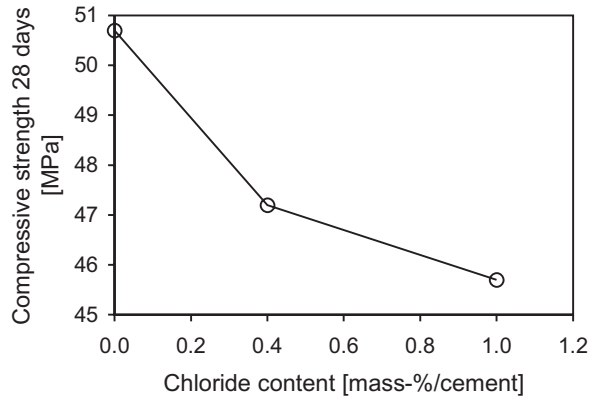

Figure 59: Compressive strength after 28 days storage at 90% r.h. versus chloride content.

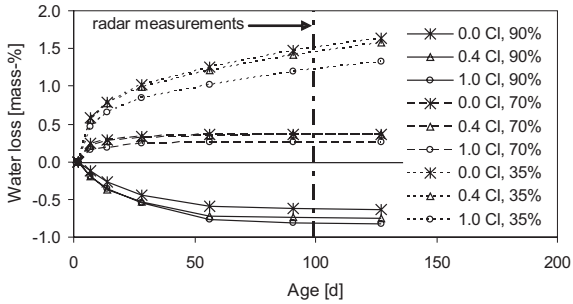

Figure 60: Water loss (mass-% of the total concrete weight) of the slabs stored at different relative humidities.

The change in weight of the different slabs is shown in Figure 60. While the slabs stored at 35% r.h. and 70% r.h. loose weight, the slabs at 90% r.h. absorb moisture and gain weight. Moisture content in concrete is additionally influenced by the addition of sodium chloride. Due to the hygroscopic properties of the salts formed, the moisture loss at constant relative humidity is decreasing with increasing sodium chloride content. On the other hand, the absorption of moisture at 90% r.h. is increasing with increasing sodium chloride content.

However, the differences in weight caused by the changing relative humidity are considerably higher than the differences caused by the hygroscopic salts. The equilibrium for 90% r.h. and 70% r.h. is already reached after 99 days and therefore, the on-site conditions for real structures are well represented.

Compressive strength of concrete after 136 days of curing is dependent on the relative humidity of storage (Figure 61). With increasing humidity, the compressive strength is increasing as well. Since only one core sample for each slab was tested, there is a certain variance in the results. Compressive strength after 136 days seems to be almost independent of chloride content. This is different from the results obtained after 28 days in 90% r.h..

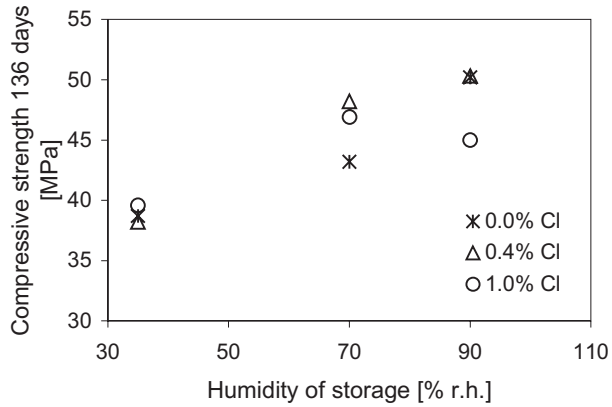

Figure 61: Compressive strength after 136 days versus humidity of storage.

After the data acquisition, data were stacked fifty fold (50 neighbouring traces were added together for noise suppression). No further processing steps were applied to the data. A plot of the signals obtained in the centers of four of the specimens is presented in Figure 62. The reflections from the top of the concrete (marked with an arrow) with a two-way-traveltime (twt) in between 6 and 8 ns and the reflections from the aluminum sheet with a twt between 8 and 10 ns are clearly visible.

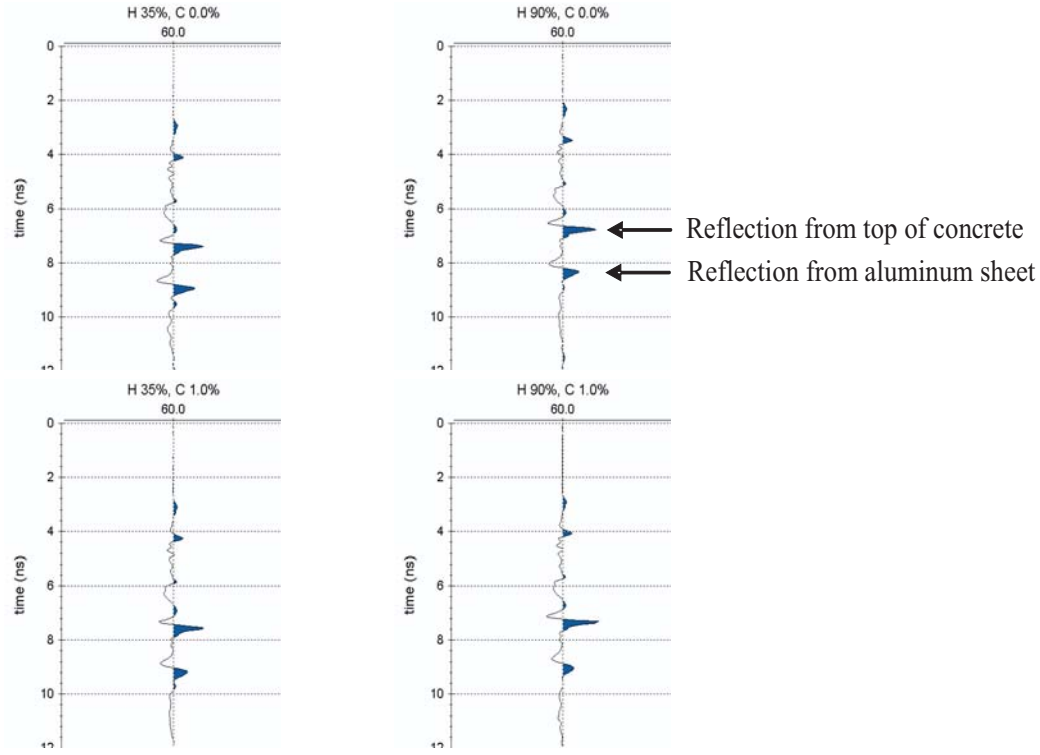

Figure 62: Signals from 4 specimens, top left 0.0% Cl-35% r.h., top right 0.0% Cl-90% r.h., bottom left 1.0% Cl-35% r.h. and bottom right 1.0% Cl-90% r.h..

When comparing the data from the 0.0% Cl-35% r.h. specimen (top left) with the 1.0% Cl-90% r.h. specimen (bottom right) the reduced reflection amplitude at the aluminum sheet is obvious for 1.0% Cl-90% r.h. concrete. In addition there seems to be a slight increase of the top of concrete reflection amplitude for the 1.0% Cl-90% r.h. specimen. The 0.0% Cl-90% r.h. and the 1.0% Cl-35%r.h. specimens seem to have slightly reduced reflection amplitudes for the aluminum sheet when compared to the 0.0% Cl-35% r.h. specimen.

In order to quantify the effects of moisture and chloride content on the signal amplitudes, mean values of the reflection amplitudes for the concrete surface and the aluminum sheet were computed for all specimens. For the concrete surface reflection the results for the nine specimens are summarized in Table 6.

Table 6: Concrete surface reflection amplitudes.

relative humidity / chloride addition	35%	70%	90%
0.0%	10675	11374	11986
0.4%	10832	11638	12204
1.0%	10824	11946	13017

A graphical chart of those results is presented in Figure 63. Obviously the reflection amplitude at the concrete surface depends both on the humidity and the chloride addition with the humidity having a stronger influence. The difference between the minimum and maximum amplitudes is 18% of the maximum amplitude.

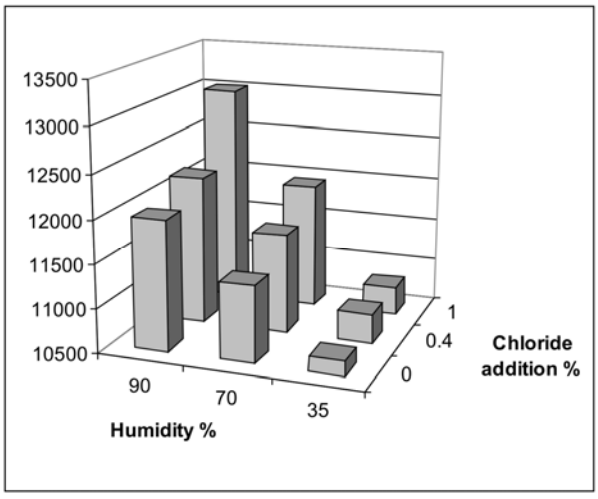

Figure 63: Concrete surface reflection amplitudes.

The results for the aluminum sheet reflection are summarized in Table 7. A graphical chart of the results is shown in Figure 64. Please note that both the humidity and the chloride content axis were turned with respect to Figure 64 to increase the readability of the chart. Obviously the reflection amplitude depends both on the humidity and the chloride content with both having a similar influence. The difference between the minimum and maximum amplitudes is 48% of the maximum amplitude and is thus considerably larger than for the concrete surface reflection.

Table 7: Aluminum sheet reflection amplitudes.

relative humidity / chloride addition	35%	70%	90%
0.0%	7812	6645	5939
0.4%	6549	5523	5137
1.0%	5540	4730	4065

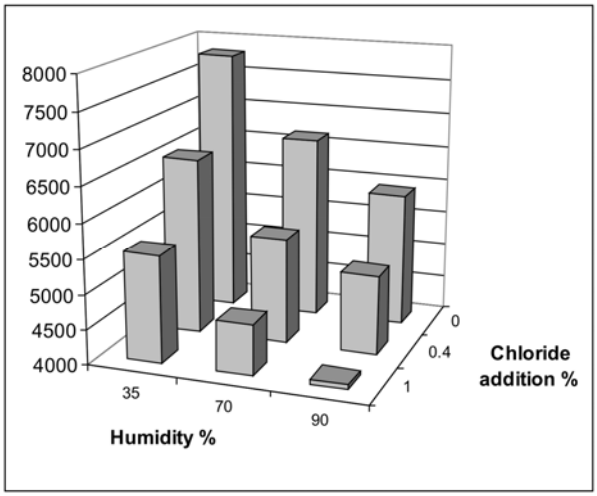

Figure 64: Aluminum sheet reflection amplitudes.

When inspecting bridge decks, the energy emitted via the antenna is submitted to damping within the asphalt pavement. Absolute amplitudes are therefore of limited use for the investigation of chloride content and humidity. The quotient of the concrete surface reflection and the rebar reflection amplitudes can be expected of being independent of the damping within the pavement. In addition, as those two amplitudes are related inversely to humidity and chloride content, an enhancement of the detectability can be expected.

In Table 8, the quotient of concrete surface and aluminum sheet reflection amplitudes as computed from Table 6 and Table 7 are presented and in Figure 65 the corresponding

graphical chart is shown. The difference between the minimum and maximum quotients is 57% of the maximum amplitude and thus larger than the differences for the concrete surface reflection or the aluminum sheet reflection alone, which should increase the stability of this approach on real bridges where numerous factors will affect the quality of results.

Table 8: Quotient of reflection amplitudes.

relative humidity / chloride addition	35%	70%	90%
0.0%	1.37	1.71	2.02
0.4%	1.65	2.11	2.38
1.0%	1.95	2.53	3.20

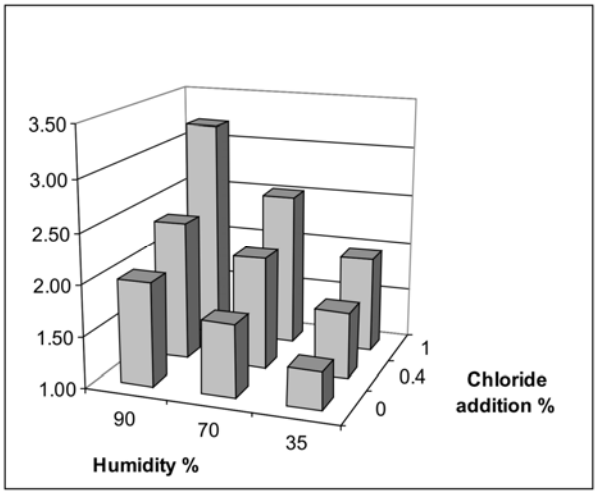

Figure 65: Quotient of reflection amplitudes.

Conclusions

In a laboratory experiment it has been shown that both moisture and chlorides have a measurable influence on the reflection amplitudes of radar signals at the concrete surface and an aluminum sheet situated below the concrete specimen.

The simplified production of the specimens (adding of chloride during production and storage at different relative humidities during hydration) does change concrete properties. The main difference is clearly caused by storage at different r.h.. This suggests that the microstructure of the concrete is not influenced substantially by the addition of chlorides during production. Thus, the simplified production of the specimens seems to be acceptable with respect to the radar results.

The computation of the quotient between the reflection amplitudes at the concrete surface and the aluminum sheet provides in the laboratory experiment a reasonable approach for the detection of both chloride content and humidity in concrete. However, further investigations are needed to transfer these laboratory results to real structures.

Acknowledgements

The work presented here is sponsored by the Building Department of Canton Vaud and the Swiss Federal Roads Authority (AGB2005/009).

4 The inspection of retaining walls using GPR

Johannes Hugenschmidt and Alexis Kalogeropoulos

Journal of Applied Geophysics 67 (2009): 335-344

Abstract

In hilly regions, retaining walls along roads, motorways and railway lines are numerous. In some cases the knowledge of the details of the construction is limited. If rehabilitation work becomes necessary, a detailed knowledge of the construction is desirable for the improved planning of maintenance and repair. This paper describes the application of Ground Penetrating Radar (GPR) for the inspection of retaining walls. The work was carried out in two steps. First, an investigation was carried out on large retaining walls at a Swiss motorway within the framework of a service contract. This included the development of an apparatus enabling high precision positioning of the antennas on the walls. Second, a pilot study was performed on a smaller wall with optimized acquisition and processing parameters. This included the use of antennas with different orientations and the fusion of the two corresponding data sets as well as true 3-D data processing. This paper describes the approaches to data acquisition and processing in the form of the two case studies. Results from different acquisition and processing strategies are compared and the benefits and limits are discussed.

Keywords: GPR, retaining walls, rock anchors, rebar, data fusion

Introduction

The Swiss A9 motorway was built in the early seventies of the last century. It runs along the northern shore of Lake Geneva where there is a steep slope from the mountains towards the lake. As a result there is a large number of retaining walls particularly on the uphill side of the motorway. After more than 30 years in service, many of those walls are in need of repair and/or inspection. In order to evaluate the benefit of GPR as an inspection tool for those walls, a pilot study was carried out on one of the walls within the framework of a service contract. After the completion of this project, a second project was carried out on a smaller wall for the purpose of testing the benefits of enhanced data acquisition and processing.

GPR inspections of various concrete structures such as bridges, bridge decks and tunnel walls have been reported frequently (Daniels, 2004; Hugenschmidt and Mastrangelo, 2006; DGZfP 2008; Taffe et al., 2003) and can, in many cases, be considered routine applications of the radar method. The inspection of retaining walls poses challenges such as the controlled positioning of the antenna(s) on the wall face or the trade-off between the time required for data acquisition and data density. Limited literature is available on this subject.

Case study 1

A photograph of the wall and the westbound lanes of the motorway is presented in Figure 66. The wall consists of 4 different levels, the heights of the different levels are varying between 6.5 m and 4.0 m. In the following text, the levels of the wall will be numbered from bottom to top with level 1 being the bottom level and 4 the top level.

Figure 66: Retaining wall.

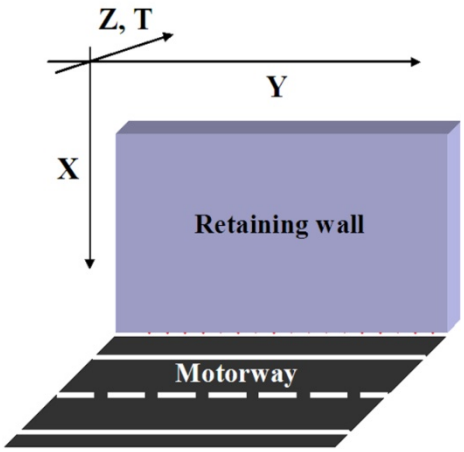

Figure 67: Coordinate system.

In Figure 67 the coordinate system used throughout this paper is shown. All data presented will be named as “A”-slices with A being the axis perpendicular to the slice.

Data acquisition

Data acquisition was carried out with a GSSI SIR-20 system in spring 2006. As this was a pilot study, three different antennas were tested. As one of the aims of this study was a test of the capability to locate the heads of rock anchors, a high accuracy of the antenna position was required. In order to achieve this, a semi-automated survey apparatus was developed. It consists of a rail system sitting on the copings of the different levels of the wall, an antenna box, a ladder-like guiding system for the antenna box, an electric motor for moving the box up and down the face of the wall, a survey wheel for controlling the vertical position of the box and triggering the data acquisition and an electronic protractor for monitoring the angle between the guiding system and the vertical line thus controlling the lateral position of the antenna. In Figure 68 the top of the apparatus is shown together with the antenna box in the guiding system on the face of the wall.

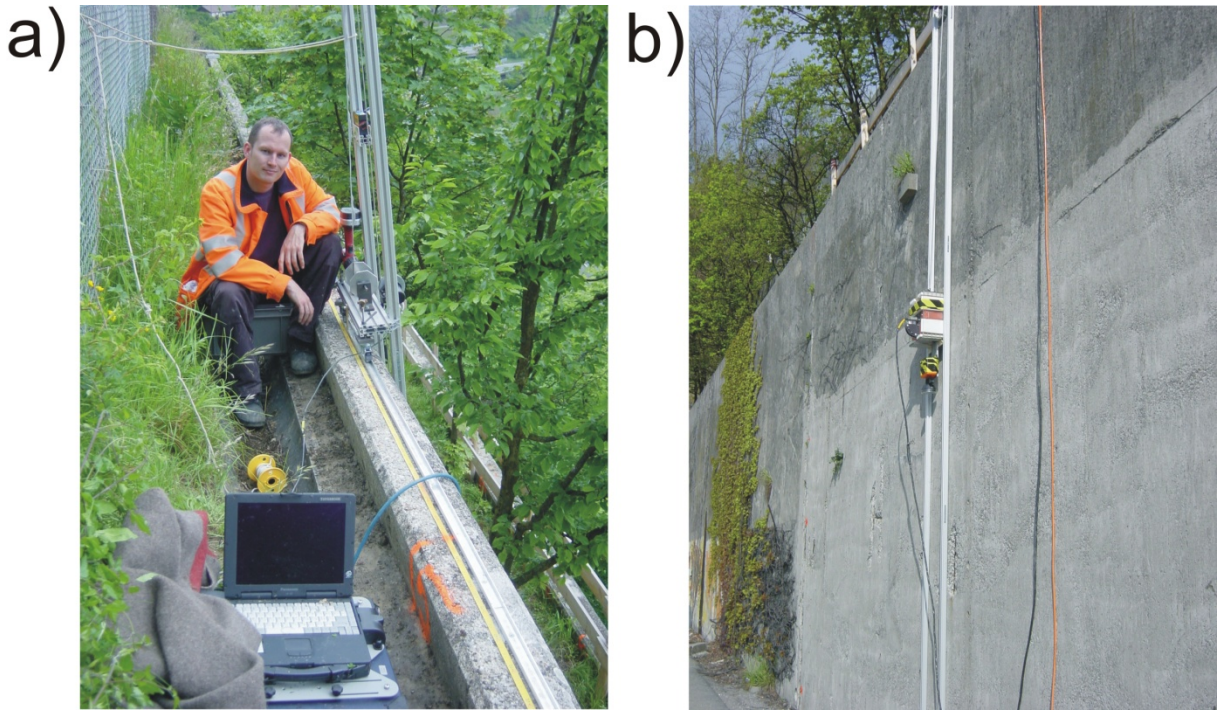

Figure 68: Semi-automated survey apparatus; a) Top of apparatus and radar system; b) Guiding system with antenna box.

Data were acquired along vertical lines corresponding to the X-direction in Figure 67 on the face of the retaining wall. All antennas were orientated such that the E-field was pointing in the Y-direction. Line spacing was varied between 0.04 and 0.1 m and the in-line sampling rate was 0.005 m. Apart from a gain function applied to ensure the optimal use of the dynamic range of the radar system, no data processing was performed during acquisition. The equipment used for data acquisition and the acquisition parameters are listed below.

Radar unit:	GSSI SIR-20
400 MHz antenna*:	GSSI model 5103
900 MHz antenna*:	GSSI model 3101-D
1500 MHz antenna*:	GSSI model 5100
Apparatus for data acquisition:	EMPA custom-built

*antenna frequencies as provided by manufacturer

Acquisition parameters:

Samples per scan:	512 (400 MHz model 5103 and 900 MHz model 3101-D antennas)
	1024 (1500 MHz model 5100 antenna)
Line spacing:	0.04 m (1500 MHz model 5100 antenna)
	0.1 m (400 MHz model 5103 and 900 MHz 3101-D antennas)
In-line sample rate:	0.005 m
Scan-length:	40 ns (400 MHz model 5103 antenna), 25 ns (900 MHz model 3101-D antenna), 20 ns (1500 MHz model 5100 antenna)

After the equipment had been set-up, up to 30 vertical lines were acquired per hour. Depending on the line spacing this corresponds to a horizontal distance between 1.2 and 3.0 m per hour.

Data processing

Data were copied to a personal computer and processed using REFLEXW software (Sandmeier, 2007). The 2-D processing sequence for the model 5100 antenna can be summarized as follows:

- Bandpass filtering (lower cutoff 200 MHz, lower plateau 400 MHz, upper plateau 2700 MHz, upper cutoff 2900 MHz)
- Static correction of picked direct wave
- Kirchhoff migration using v=0.11 m/ns
- Gain correction using a linear gain function (0 dB at 0 ns and 20 dB at 20 ns)
- Time cut to the same number of samples per scan for each data set (corresponding to 12 ns for the 1500 MHz model 5100 antenna)
- Resampling to 0.04 ns to reduce the size of the data sets
- Background Removal by subtraction of a mean trace (2-D data were transferred into 3-D data sets with and without Background Removal)

No corrections concerning the position of lines or traces were applied. This was unnecessary due to the high accuracy of the positioning made possible by the apparatus described in the section "data acquisition". Following the 2-D processing sequence data were merged into 3-D files. All interpretation was based on 3-D files.

Interpretation and results

Antennas

In general, it can be assumed that high frequency antennas provide better resolution but less depth of penetration than low frequency antennas. As far as the resolution is concerned, this assumption can be easily confirmed by a comparison of the data sets obtained with the three antennas on level 2 of the retaining wall. In Figure 69-a the time range between 0 and 4 ns of a Y-slice is shown for the 1500 MHz antenna. Three single bars can be clearly distinguished. In Figure 69-b the corresponding section acquired with the 900 MHz antenna is shown and Figure 69-c presents the 400 MHz data. Obviously, the assumption of higher frequency corresponding to higher resolution is valid for this case. Looking at data from the same location but from a time window between 4 and 8 ns (Figure 70), it becomes clear that the second assumption is not true in this case as the 400 MHz data do not offer any benefit when compared to the 1500 MHz section. This is probably due to the abundance of rebar present in the wall. As this was the case in most other locations as well, it was decided to restrict the interpretation to the 1500 MHz and 900 MHz data.

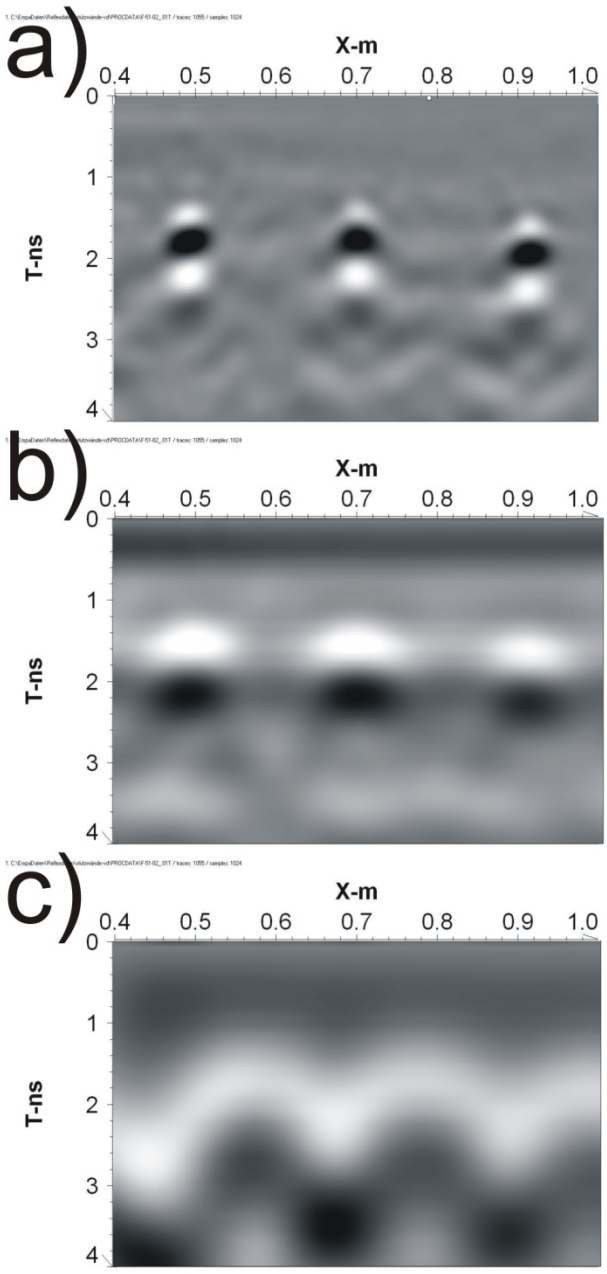

Figure 69: Y-slices, 0-4 ns; a) 1500 MHz antenna (top); b) 900 MHz antenna (middle); c) 400 MHz antenna (bottom).

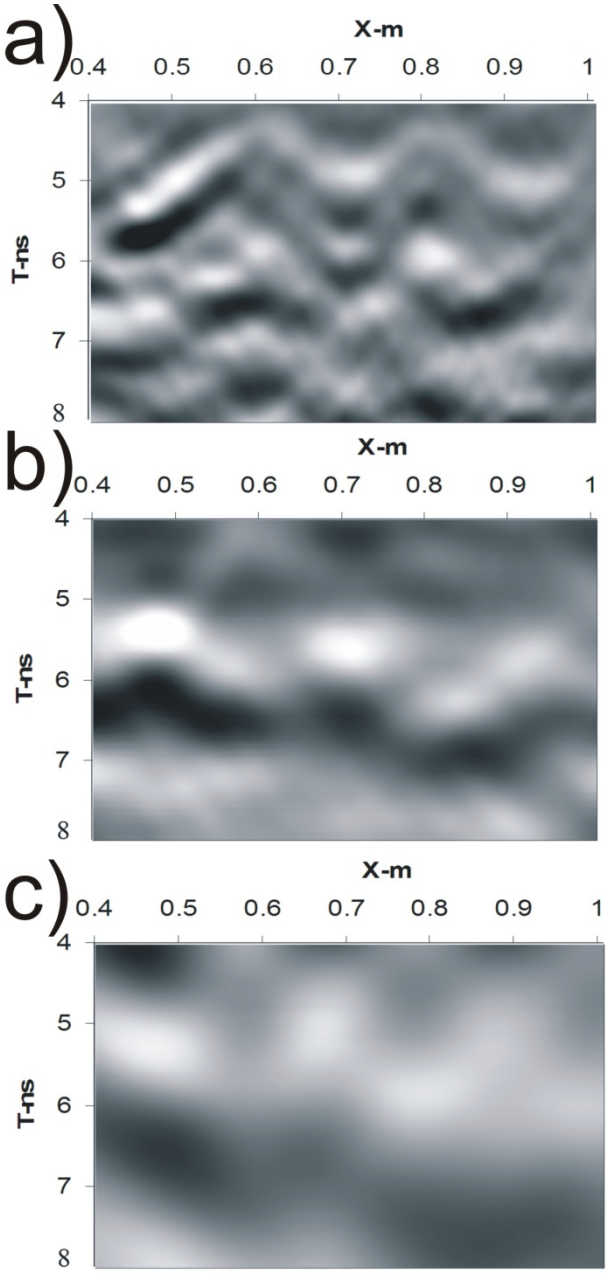

Figure 70: Y-slices, 4-8 ns; a) 1500 MHz antenna (top); b) 900 MHz antenna (middle): c) 400 MHz antenna (bottom).

Rebar

In Figure 71-a a T(ime)-slice (t=0.92 ns) from level 2 is presented. In the lower left and upper central region the first layer of rebar is visible, whereas in all other regions the rebar is at greater depth. The alternative explanation of varying signal velocities within the concrete due to changes in material properties seems rather unlikely, because the original concrete and the exposure to environmental conditions are probably similar for the same section of a single wall. Two strong reflections from structures present in addition to the rebar are marked with arrows.

In the corresponding slice at t=1.6 ns (Figure 71-b) the top layer of rebar is mapped almost completely. Vertical bars (bars parallel to the X-axis) cause weaker reflections when compared to horizontal bars because of the antenna orientation during data acquisition and because of the application of a background removal during data processing. Also, in this figure the accuracy of the acquisition apparatus becomes apparent, as only minor deviations of a maximum of about 0.02 m are visible (white arrow). These are mainly caused by the roughness of the surface of the wall. At t=5.16 ns (Figure 71-c) a second layer of rebar is visible, however it is obvious that signal quality as well as resolution have deteriorated considerably.

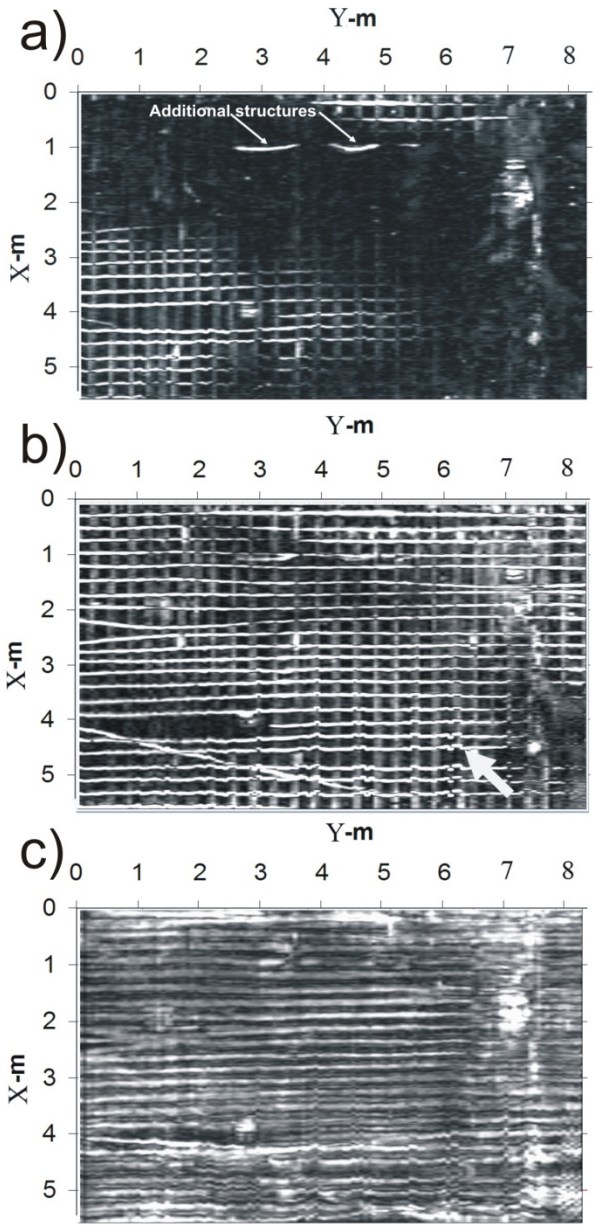

Figure 71: Level 2, 1500 MHz, T-slices ; a) t=0.92 ns corresponding to approximately 0.05 m (top); b) t=1.6 ns corresponding to approximately 0.09 m (middle); c) t=5.16 ns corresponding to approximately 0.28 m (bottom).

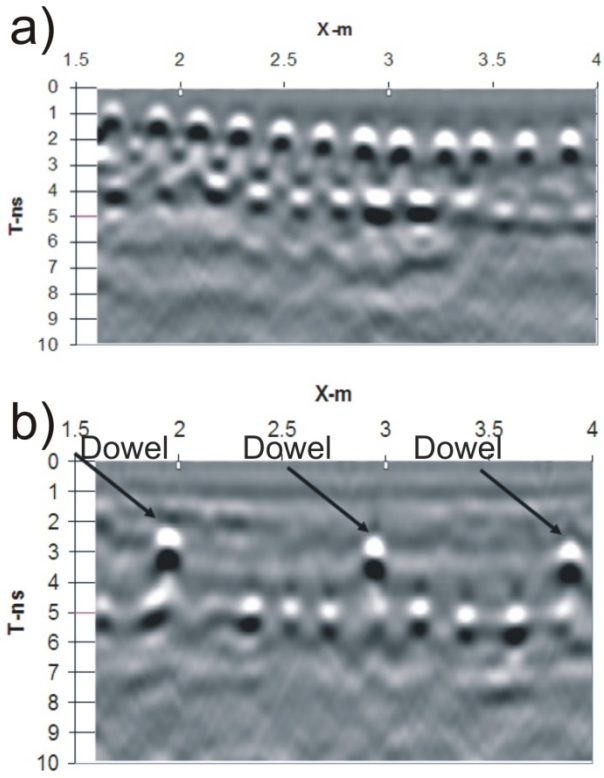

Figure 72: Y-slices from level 3, 1500 MHz; a) 4.3 m from joint (top); b) On joint (bottom).

Joints and Dowels

Two Y-slices from level 3 are presented in Figure 72. The line in the upper Figure 72(a) was acquired at a distance of 4.3 m from a joint separating two different sections of the wall. Two layers of rebar are visible. The line presented in the lower Figure 72(b) was acquired on the joint. Only one layer of rebar is present but there are three additional reflections (arrows). As it is common practice to join separate sections of concrete with dowels and, as such, these three reflections were interpreted as dowels.

Rock anchors and anchor heads

As there was no additional information such as expected depth, size or approximate position of the anchor heads available, it was not possible to decide conclusively whether a reflection present in the radar data was caused by an anchor head or not. Possible locations of anchor heads were therefore defined in two steps:

- The 3-D data sets were searched for reflections that could not be related to rebar, dowels or other structures expected to be present in the walls
- The position of these reflections was compared to structures visible on the face of the walls such as water outlets. Anomalous reflections without corresponding structures visible on the wall faces were then considered as possible positions for the anchor heads.

In the upper Figure 73 a Y-slice from level 1 is presented. A prominent reflector is marked with a white arrow. In the lower Figure 73 the Y-slice is combined with a T-slice giving an indication of the X-Y extension of the reflector.

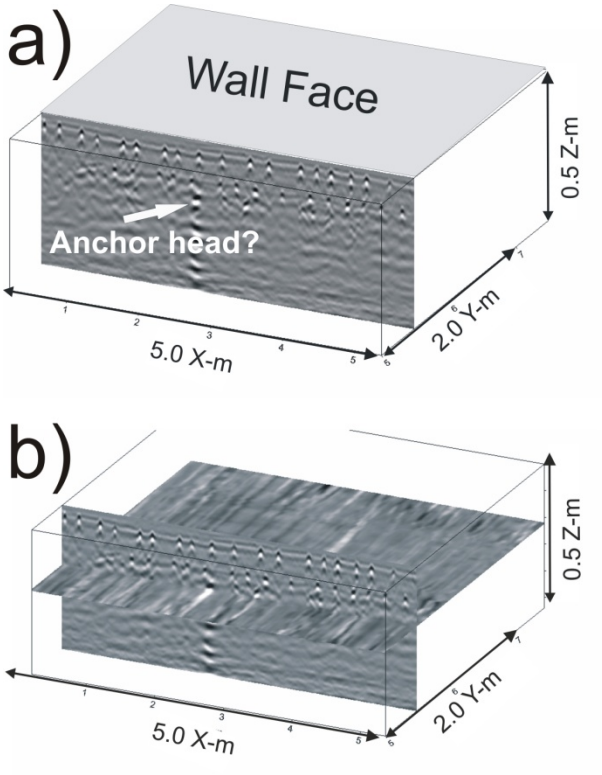

Figure 73: Level 1, 1500 MHz; a) Y-slice (top); b) Y-slice combined with T-slice (bottom).

Figure 74 shows a map of possible anchor head positions (black rectangles) for level 1. It is likely that some of those positions are the result of other reflectors than anchor heads. However, based on radar data alone a distinction between anchor heads and other reflectors is not possible.

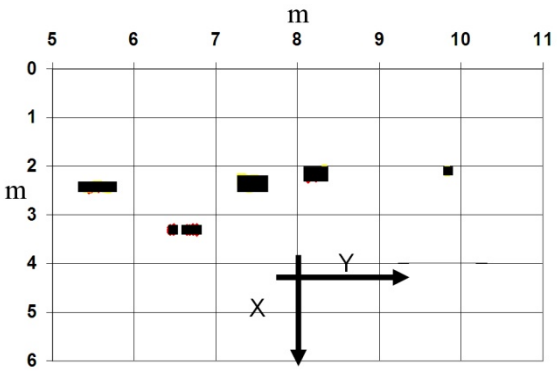

Figure 74: Possible locations of anchor heads on level 1.

Case study 2

In case study 1, it was shown that the inspection of large retaining walls with GPR can provide detailed results on structural elements. Room for improvement was spotted mainly with respect to the directionality of the results (e.g. the ability to image horizontal versus vertical rebar). It was therefore decided to carry out a second study with the focus on strategies for the reduction of the polarization dependence of radar results using two perpendicular antennas, as shown in Figure 75.

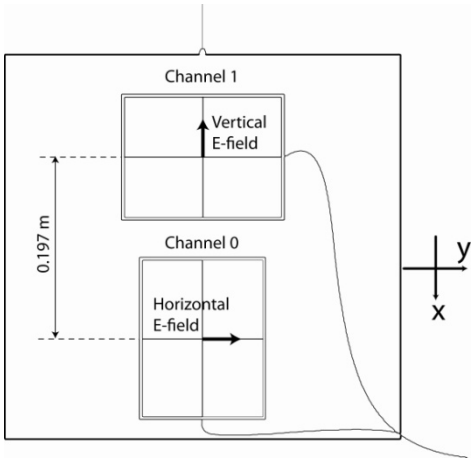

Figure 75: Antenna box with two antennas.

Figure 76: Test site 2 with apparatus for data acquisition.

Data acquisition

Case study 2 was carried out on a smaller wall (Figure 76). The same apparatus as in case study 1 was used for data acquisition. Two 1500 MHz antennas were placed perpendicular to one another in the antenna box and the data from both antennas were recorded simultaneously. The inspected part of the wall was 1.41 m long and about 2.50 m (± 0.02 m) high. The acquisition parameters can be summarized as follows:

- Scans per meter: 400 for each antenna
- Samples per scan: 512
- Line spacing: 0.01 m
- Trace length: 15 ns
- Distance between antenna centers: 0.197 m

After the system had been set up, an average of 40 lines was acquired per hour.

Data processing

Data processing was carried out in three steps. Firstly, data were processed linewise (Y-slices, 2-D processing), then data were combined into two 3-D data sets (one for each antenna) for 3-D migration and finally the two data sets were merged by adding corresponding samples together using Matlab (The Mathworks Inc., version 7.4).

The 2-D processing was applied line by line to the data sets of both antennas. The processing sequence can be summarized as follows:

- Time shift
- Dewow (mean subtraction) filter
- gain correction, using a linear gain function (0 dB at 0 ns and 20 dB at 15 ns)
- Background removal by subtraction of a mean trace
- Spiking-deconvolution: This processing was applied mainly to increase resolution. The filter wavelet was calculated using a recursive autocorrelation algorithm (Levinson) on part of the traces (0-13 ns). This filter was then convolved with the original traces with 50% white noise added.
- F-K filter: The box coordinates of the F-K filter were (0 kx, 70 MHz; -20 kx, 1000 MHz; 20 kx, 1000 MHz; 0 kx, 2700 MHz). The role of this filter was to reduce the effect of white noise added during the deconvolution.

Following 2-D processing, lines were merged into 3-D data sets. This was done for both antennas separately. The data were migrated in 3-D using Stolt's algorithm and a signal velocity of 0.105 m/ns. The Stolt algorithm was used for the 3-D migration because it is faster than the Kirchhoff algorithm (used for case study 1) and therefore well suited for large 3-D data sets (Sandmeier K., personal communication).Two lines (Y-slices) from the two data sets after processing are presented in Figure 77. Obviously the horizontal E-field antenna provides a better result for the horizontal rebars and the vertical E-field antenna is more sensitive to vertical rebars. The 2-D processing and the 3-D migration were carried out using REFLEXW software (Sandmeier, 2007).

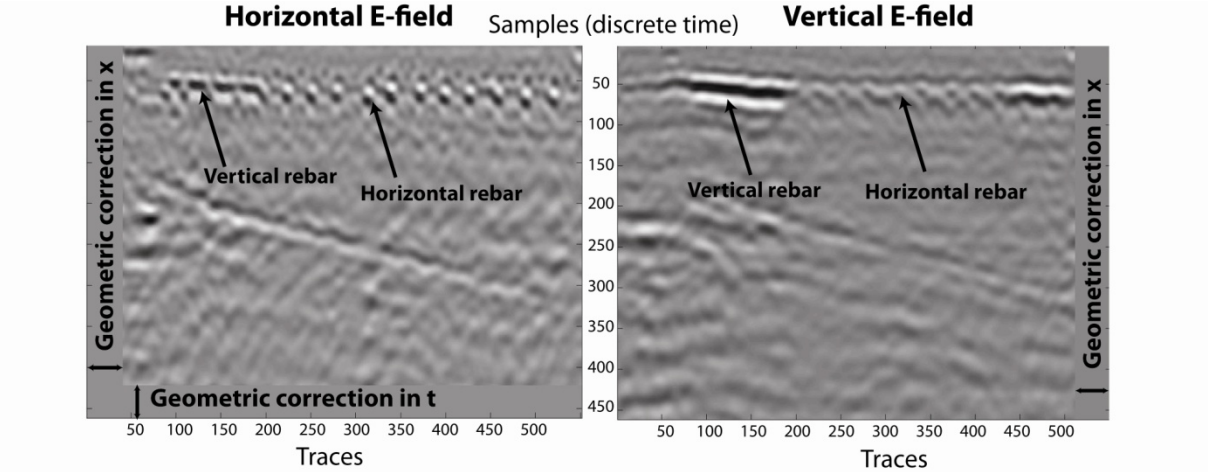

Figure 77: Y- slices; horizontal E-field (left); vertical E-field (right); 100 discrete time samples correspond to 2.93 ns, 401 traces correspond to 1.0 m.

Data fusion

Data fusion was the final step of data processing merging the data from both antennas. As this was done line by line, the 3-D data sets were split into the original number of 141 lines per antenna. All computations were carried out using Matlab software (The Mathworks Inc., version 7.4). As the antenna centers were 0.197 m apart during data acquisition and because the time window of the recordings was slightly different, a geometric correction was applied to generate Y-slices with the same number of samples in the X- and T-directions. This was done by adding samples with a value of zero (Figure 77).

In Figure 78, two sections of traces from the two antennas recorded in the same position are shown. These traces will serve as examples for the data fusion.

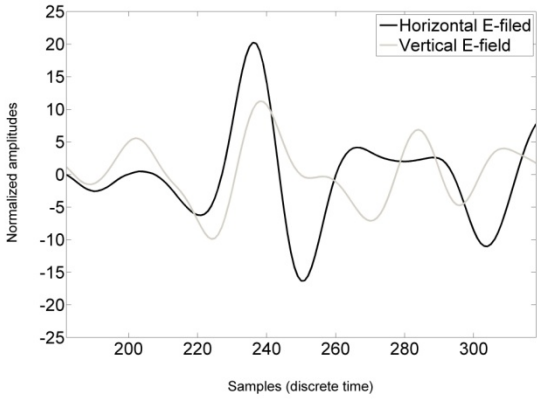

Figure 78: Two sections of traces recorded in the same position with the two 1500 MHz antennas, 100 samples correspond to 2.93 ns.

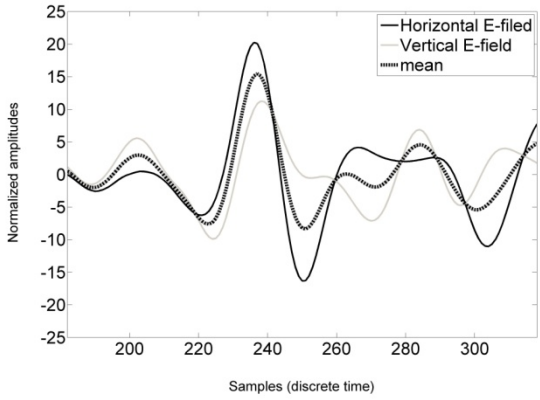

Figure 79: Traces merged with mean algorithm and original traces; 1500 MHz antennas, 100 samples correspond to 2.93 ns.

Based on the work by Kohl et al. (2003), two data fusion algorithms were tested. The first computes the average of amplitudes:

$$As,t = \sum_{i=1}^{2} A_{s,t,i} \Big/ 2 \qquad [1]$$

Where $A_{s,t}$ is the amplitude from sample *s* in trace *t*, and *i* denotes data sets 1 and 2. The application of this algorithm to the two traces shown in Figure 78 produces the result presented in Figure 79. This approach adds only little noise but leads, in many locations, to a reduction of peak amplitudes.

The second approach uses the maxima of the amplitudes:

$$As,t = \max \bigcup_{i=1}^{2} A_{s,t,i} \qquad [2]$$

Using this approach leads to the result presented in Figure 80. Here the peak amplitudes are well preserved but at the expense of an increased noise level.

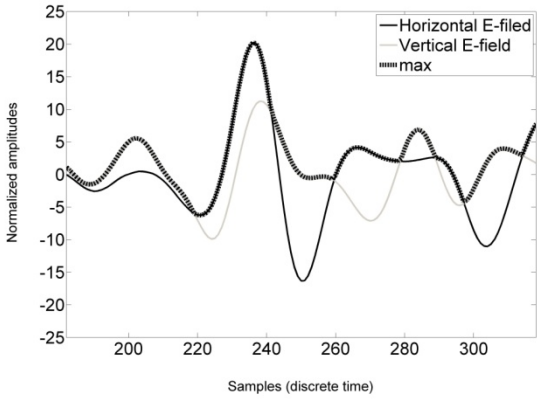

Figure 80: Traces merged with maximum algorithm and original traces; 1500 MHz antennas, 100 samples correspond to 2.93 ns.

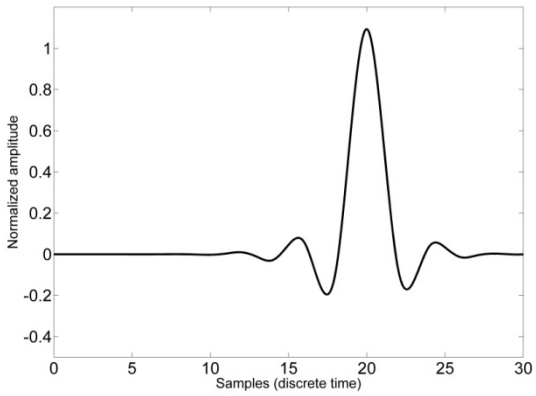

Figure 81: Coiflet wavelet.

The disadvantage of the two approaches described above is that they do not take into account the fact that both signals are not exactly in phase. This can change the amplitude of a reflected signal and the size or the position of an interpreted reflector.

Here, it is proposed to use a different approach, each trace is decomposed into sub-spaces using finite time, oscillating, zero mean signals called wavelets (Mallat, 1989). Then the corresponding sub-spaces from both traces are merged and reconstructed into a fused trace. The decomposition conducted with predefined wavelets containing frequency and time information is called continuous wavelet transform.

Continuous wavelet transform

According to continuous wavelet transform theory a function f(t) can be decomposed into a set of basic functions $\psi_{s,\tau}(t)$ [eq. 3], were the variables s and τ denote scale and translation respectively and * denotes the complex conjugate.

$$\gamma(s,\tau) = \int f(t)\psi^*_{s,\tau}(t)dt \quad [3]$$

The inverse wavelet transform is given by:

$$f(t) = \int\int \gamma(s,\tau)\psi_{s,\tau}(t)d\tau ds \quad [4]$$

The *child* or *scaled wavelets* are generated from a single basic wavelet $\psi(t)$, *mother wavelet*:

$$\psi_{s,\tau}(t) = \frac{1}{\sqrt{s}}\psi\left(\frac{t-\tau}{s}\right) \quad [5]$$

In equation [5], s is the scale factor, τ is the translation factor and $s^{-1/2}$ is the energy normalization across different scales.

As previously mentioned the wavelet used is predefined. Numerous wavelets types are mentioned in the literature. After testing several families of wavelets (Daubechies, Symlets, Coiflets, Haar) during this study it was concluded that Coiflet wavelets (Figure 81) gave the best result. This is because, according to the literature, the shape of the mother wavelet should be as close as possible to the shape of the emitted radar pulse (Perrin et al., 2000).

Discrete wavelet decomposition and fast wavelet transform

For computational reasons, the continuous wavelet equation [5] has to be changed into a discrete form, where j and K are integers and $s_0 > 1$.

$$\psi_{j,k}(t) = \frac{1}{\sqrt{s_0^j}}\psi\left(\frac{t-k\tau_0 s_0^j}{s_0^j}\right) \quad [6]$$

In this study the decomposition was carried out with an algorithm designed by Mallat (1989) using Matlab software (The Mathworks Inc., version 7.4), the Fast Wavelet Transform, which can be summarized as passing the traces through a series of filters to decompose each subspace into two smaller sub-spaces. For that the lower frequency part of the signal (low pass,

eq. 7) and the upper frequency part of the signal (high pass, eq. 8) are calculated at each decomposition level, giving approximation coefficients and details coefficients respectively (Figure 82).

$$y_{low}[n] = (x * g)[n] \quad [7]$$

$$y_{high}[n] = (x * h)[n] \quad [8]$$

Were y_{low} and y_{high} are the two resulting sub-spaces of the previous *x* signal, *g* can be considered as the wavelet low pass filter, *h* as the high pass filter and *n* is the sample number (discrete time). For computational reasons, the filter outputs are downsampled by a factor of 2 (Figure 82).

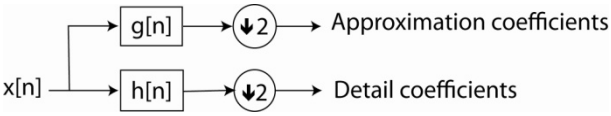

Figure 82: Generation of two downsampled subspaces (Mallat, 1989).

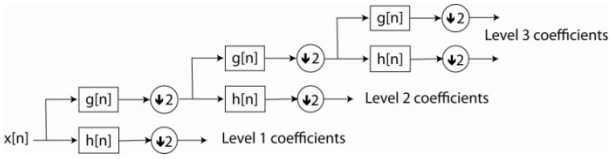

Figure 83: Fast wavelet transform decomposition tree, three levels (Mallat, 1989).

This operation is recursive and can be executed with a number of predefined levels. In this study, five levels were used after different numbers of levels have been tested. Figure 83 shows this decomposition for three levels.

With both signals decomposed into the desired levels, the fusion operation can be applied. To do so it is required to define the fusion rules. In this study it has been observed that averaging the approximation coefficients and taking the maximum of the detail coefficients gave the best result. After the coefficients of each level have been fused, equation [4] is used to recompose the merged traces.

The result of the wavelet fusion is presented in Figure 84. The wavelet fusion algorithm combines the advantages of the average and maximum methods by keeping noise low and maintaining peak amplitudes. Figure 85 shows sections of Y-slices of the two data sets (a and b) together with the results of the different fusion methodologies (c, d and e). This comparison confirms the conclusions from the comparison of single traces. The mean algorithm leads to a reduction of amplitudes, particularly visible between traces 200 and 300. The maximum algorithm leads to a high amplitude, high noise result. The wavelet fusion algorithm combines the advantages of the mean and maximum approaches, mapping both, vertical (traces 100-200) and horizontal (traces 200-300) rebar, appropriately. Obviously, the re-

sults of the mean and wavelet algorithm show some similarity. However, when focusing on the horizontal rebar (traces 200-300), the wavelet result is clearly advantageous.

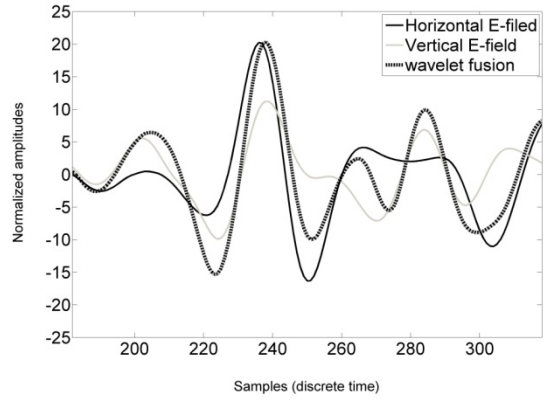

Figure 84: Traces merged with wavelet fusion algorithm and original traces; 1500 MHz antennas, 100 samples correspond to 2.35 ns.

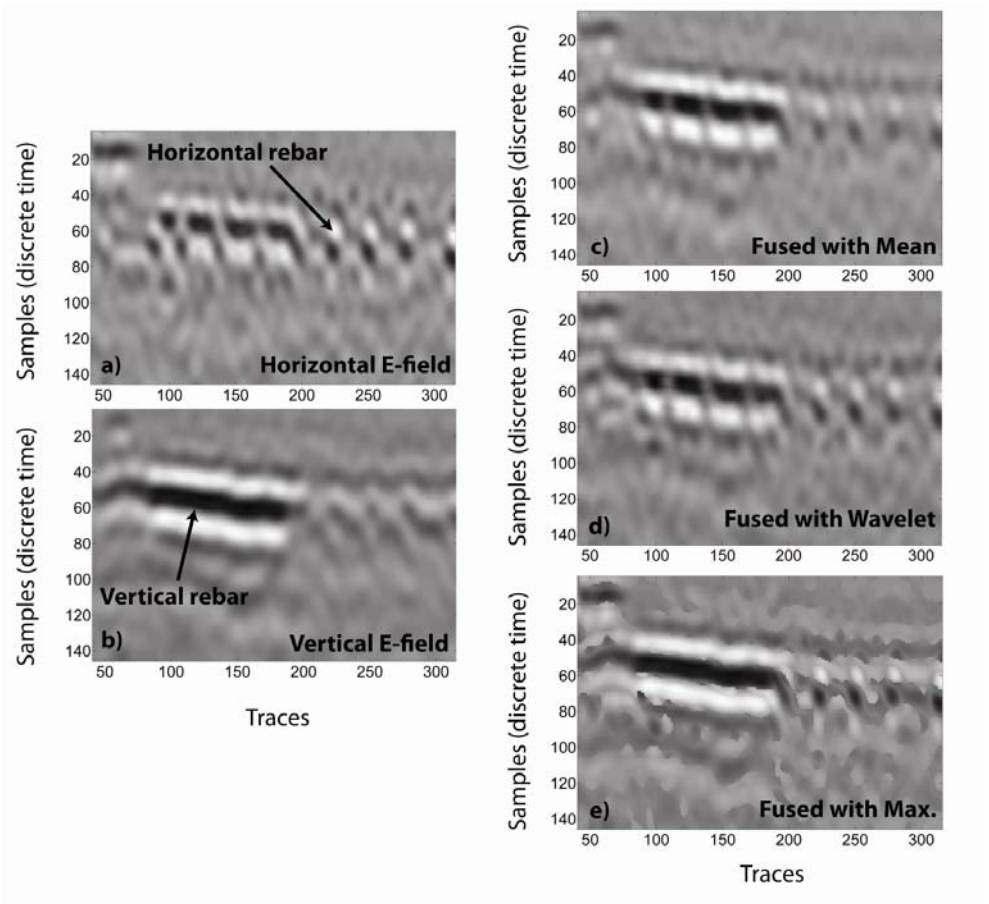

Figure 85: a) and b) Sections of original Y-slices; c)-e) Sections of fused Y-slices; 100 discrete time samples correspond to 2.93 ns, 401 traces correspond to 1.0 m, 1500 MHz antennas.

Figure 86 presents a T-slice from the data set fused with the wavelet approach ranging from 1.45 to 2.08 ns produced with Osirix software (Osirix, 2008). The fused data set maps hori-

zontal and vertical structures and therefore combines the information from the two antenna orientations. The combination of information from different sources into a single data set facilitates the interpretation of the data and enhances the accessibility for non-specialists.

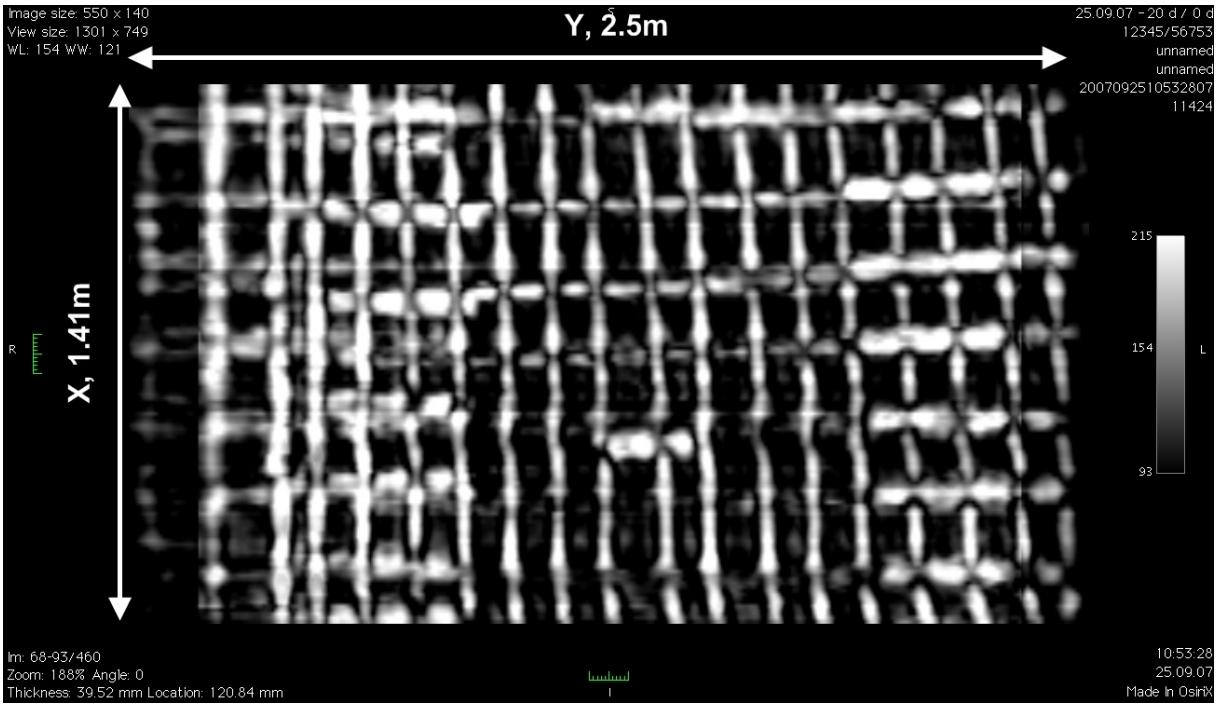

Figure 86: T-slice, data set fused with wavelet algorithm, t=1.45-2.08 ns corresponding to approximately 0.075 m to 0.11m, 1500 MHz antennas.

Conclusions

The apparatus developed for the inspection of retaining walls enables an efficient data acquisition on large and small retaining walls with a high accuracy of positioning. Depending on the height of the wall, between 30 and 40 vertical lines were acquired per hour.

In case study 1, the 400 MHz antenna did not improve the depth of penetration when compared to the 900 MHz and 1500 MHz antennas. This is probably due to the abundance of rebar within the wall.

With the 900 MHz and 1500 MHz antennas it was possible to map accurately several layers of rebar and additional structures such as dowels in case study 1.

Although, in case study 1, several anomalous reflectors were found on each level of the wall, it is not possible to decide whether those are related to rock anchors or not, based on radar data alone.

The fusion of data sets acquired with antennas with different orientations can significantly reduce the directionality of radar data. Thus, longitudinal objects with different orientations can be mapped properly. The wavelet fusion algorithm provided better results than the

maximum or average algorithms when applied to the top layer of rebar. The combination of information from different sources into a single data set facilitates the interpretation of the data and enhances the accessibility for non-specialists.

Future work will focus on advanced processing and inversion schemes applied to deeper structures and the back wall reflection.

Acknowledgements

The authors wish to express their gratitude to the building department of Canton Vaud for the permission to publish the results presented in case study 1. We thank the two anonymous reviewers and Special Edition Guest Editor Nigel Cassidy whose comments improved the quality of this paper significantly. Special thanks to Roman Mastrangelo, formerly EMPA, for building the apparatus used for data acquisition.

5 Processing strategies for high-resolution GPR concrete inspections

Johannes Hugenschmidt, Alexis Kalogeropoulos, Francesco Soldovieri and Giancarlo Prisco

NDT&E International 43 (2010): 334–342

Abstract

A high resolution multi-sensor and multi-polarization Ground Penetrating Radar (GPR) data set was acquired on a concrete retaining wall. This data set was characterised as a low pass filter with the help of a moving window spectral analysis. In order to examine the benefits and limits of innovative processing strategies, the data set was processed with three different methods, classical 2-D processing, full 3-D processing followed by data fusion and inverse scattering followed by data fusion. A comparison of the results for two layers of rebar present in the wall shows that the innovative approaches improve the results for near surface structures when compared to classical 2-D processing. For deeper structures, the benefits of the innovative approaches are limited because of the low pass properties of the concrete.

Keywords – GPR, Concrete, High-resolution, Data Processing, Inversion

I. Introduction

In many cases, concrete structures contain a complex interior of rebar, tendons, rock anchors and/or additional fixtures. Thus, three-dimensional Ground Penetrating Radar (GPR) surveys are often a necessity to obtain a clear visualization of the interior of a structure. The acquisition of three-dimensional data sets is a demanding task that has to be carried out on objects as different as retaining walls, bridge decks or piles and requires high accuracy of positioning. In addition, the directionality and size of the acquired data sets pose a challenge in terms of data processing strategies.

Several authors have suggested acquisition and processing strategies for high-resolution GPR data acquired on concrete. Hugenschmidt and Mastrangelo (2007) and Hugenschmidt and Kalogeropoulos (2009) describe the acquisition and processing of pseudo 3-D data from retaining walls at a Swiss motorway by exploiting single polarized antennas. Kohl et al. (2003) describe the fusion of radar data with different polarizations and the combination with ultrasonic data. Langenberg et al. (2006) describe a unified theory of modeling and imaging with electromagnetic and elastic waves for the non-destructive testing of concrete. Capizzi and Cosentino (2008) investigate different dipole configurations in experimental tests using longish objects in a homogeneous medium. Sbartai et al. (2008) suggest the use of an artificial neural network for solving the inverse problem related to radar data acquired on reinforced concrete. The application of an inverse scattering algorithm to radar data acquired on reinforced concrete is suggested by Soldovieri et al. (2006, 2007, 2008) and Solimene et al.

(2007). In fact, the adoption of a linear inverse scattering approach based on a simplified model of the electromagnetic scattering permits many applicative advantages in terms of fast and effective processing. This is very suitable to perform high resolution imaging using large data sets in quasi real time (Soldovieri et al., 2006).

In this paper, we deal with the inspection of a retaining wall (Hugenschmidt and Kalogeropoulos, 2009) by adopting an advanced data acquisition apparatus able to produce 3-D high resolution multi-polarization data sets thanks to the simultaneous exploitation of two antennas with different orientations. The adoption of strategies based on signal processing techniques and an inverse approach, able to exploit in an effective way the diversity in the polarization, makes it possible to map the two layers of rebar embedded in the wall.

In particular, the data set was processed with three different approaches, classical 2-D processing, 3-D processing followed by data fusion and inverse scattering followed by data fusion. This paper presents the data acquisition and the three processing strategies together with their results. The comparison of these results for two layers of rebar leads to conclusions concerning the data acquisition and processing of high resolution GPR surveys.

Therefore, the paper is organized as follows. Section II is devoted to the description of the inspected wall, data acquisition and a description of the acquired data set. In Section III, the three processing strategies are briefly depicted by referring to 2-D reconstructions of vertical profiles. In Section IV the performances of the proposed strategies are compared in terms of 3-D representations by considering the top and a deeper layer of rebar. The most important conclusions are summarized in section V.

II. Data Acquisition

Data were acquired on a retaining wall near EMPA, Switzerland (Figure 87) along vertical lines. The concrete wall (Figure 88) is increasing in thickness from top to bottom and contains two layers of rebar with overlaps near the top and the bottom of the wall. Vertical bars have a nominal diameter of 0.016 m and a distance of 0.2 m between single bars. Horizontal bars have a diameter of 0.012 m and a distance of 0.15 m. In addition, there are distance pieces with a diameter of 0.014 m connecting the two layers of rebar. Only one side of the wall is accessible as the other side is hidden by ground.

The equipment used consisted of a GSSI SIR-20 radar unit, two GSSI model 5100 antennas and an acquisition apparatus developed at EMPA for data acquisition on retaining wall (Hugenschmidt and Mastrangelo, 2007). The apparatus consists of a ladder like guiding system for the antenna box, a rail system sitting on the coping of the wall for lateral displacement and an electric motor for moving the antenna box up and down. The desired positioning accuracy of 0.01 m is achieved by the combination of a survey wheel controlling the vertical position, the rail system for an accurate position of the top of the apparatus and an electronic protractor system for the vertical alignment of the guiding system and thus the path of the antenna box. The center frequency of the antennas as examined by EMPA in a

laboratory experiment (Hugenschmidt, 2000a) is 1.25 GHz in air. Both antennas were placed in the same antenna box, recording simultaneously. The antennas were orientated with horizontal and vertical E-fields (Figure 89) thus permitting multi-polarization measurements.

Figure 87: Retaining wall with acquisition apparatus.

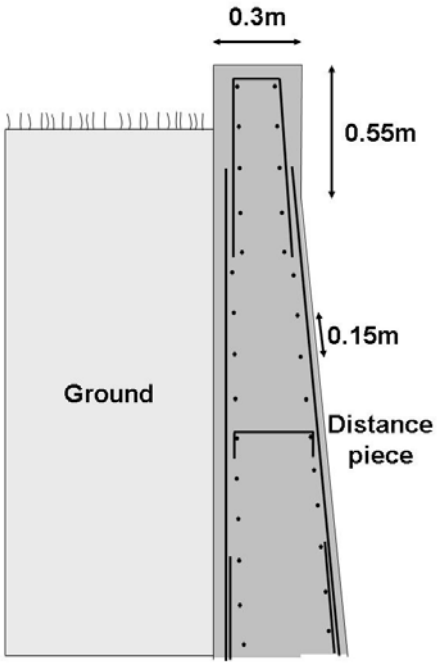

Figure 88: Retaining wall, simplified plan compiled from several original building plans.

The acquisition parameters for single antennas can be summarized as follows:

- Trace length: 15 ns
- Samples per trace: 512
- Traces per meter: 400
- Line spacing: 0.01 m
- Transmitter-Receiver offset: 0.06 m
- Data processing during acquisition: none

The coordinate system used throughout this paper is presented in Figure 90, with X and Y being parallel to the front of the wall. All data were acquired moving the antenna box along the X-axis from the top to the bottom of the wall. This is due to the acquisition apparatus which is designed for the acquisition along vertical lines parallel to the X-axis. The data set

acquired for this study covers 1.40 m in the Y-direction corresponding to 141 single lines and 2.42 m in the X-direction for each antenna.

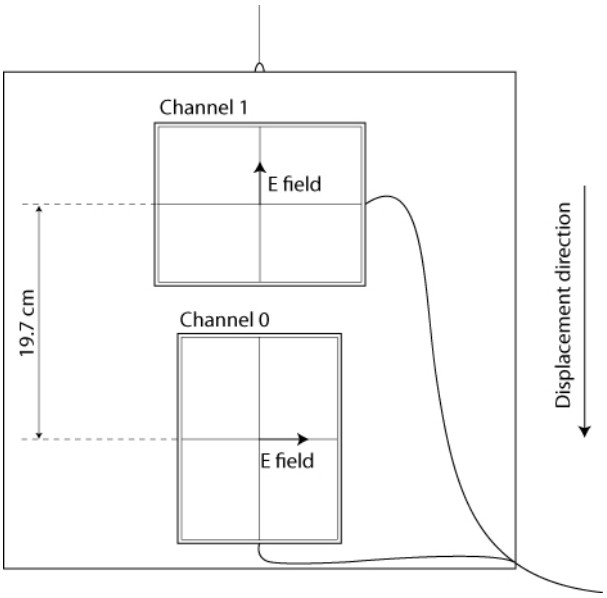

Figure 89: Antenna box.

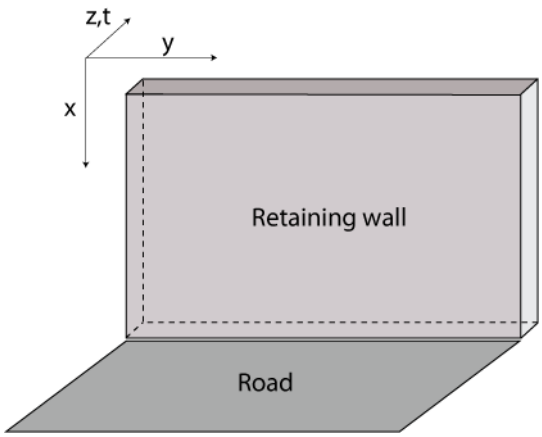

Figure 90: Coordinate system.

A comparison between the raw data sets collected with the two antenna polarizations on the same line is presented in Figure 91 and Figure 92. As expected, the antenna with the horizontal E-field is able to detect reflections in terms of hyperbolae mainly from horizontal (parallel to the Y-axis) bars whereas the antenna with the vertical E-field maps mainly vertical (parallel to the X-axis) bars (arrows in Figure 92). In order to further characterize the data, a moving window spectral analysis was applied to the two data sets shown in Figure 91 and Figure 92. The moving window spectral analysis computes amplitude spectra within time windows of a defined length via Fast-Fourier-Transform (FFT). The time window is moved along the single traces and the result of the FFT is assigned to the sample in the center of the window. Following this the amplitude spectra of all traces are added together. Before the computation of the moving window spectrum the direct wave/surface reflection was removed from the data. A time window of 2 ns was used. The result is shown in Figure 93 for the horizontal E-field data (left) and the vertical E-field data (right). In order to improve the comprehensibility of the figures, the sum of a range of 262 MHz was grouped together in one trace. In the spectrum of the horizontal E-field data, all frequencies shown have their maximum between 4.0 and 5 ns. This is due to the fact that this corresponds to the reflections from the top layer of rebar. Looking at the quotients of the maximum amplitudes between 9 ns and 12 ns divided by the maximum amplitudes between 3.8 and 4.8 ns enables an analysis of the damping with respect to two-way-traveltime. The time range between 9 and 12 ns was chosen because of the presence of a second layer of rebar (see below for details). The quotient presented in Figure 94 shows a clear decay of higher frequencies for the

later time gate and a quantitative description of the concrete structure acting as a low pass filter.

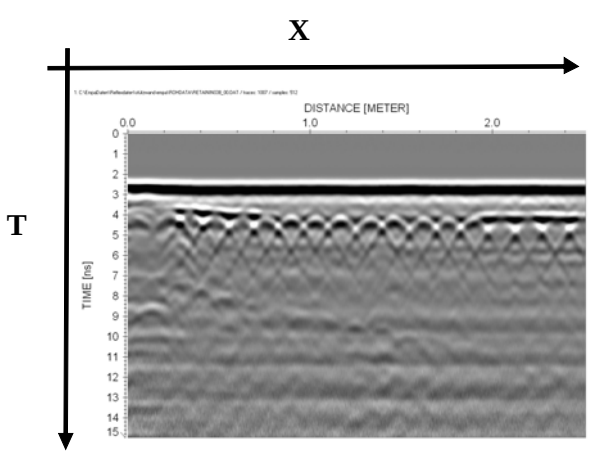

Figure 91: Raw data set, horizontal E-field, y=0.37 m.

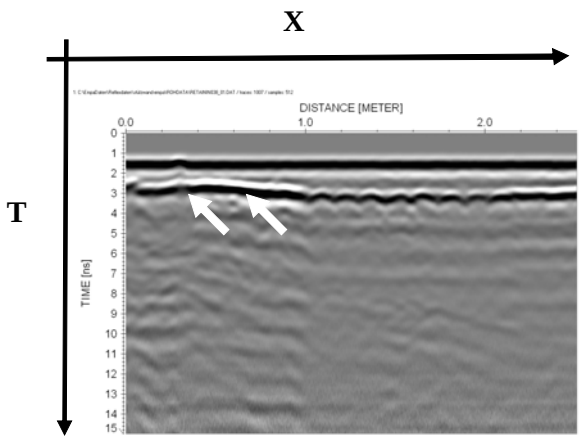

Figure 92: Raw data set, vertical E-field, y=0.37 m.

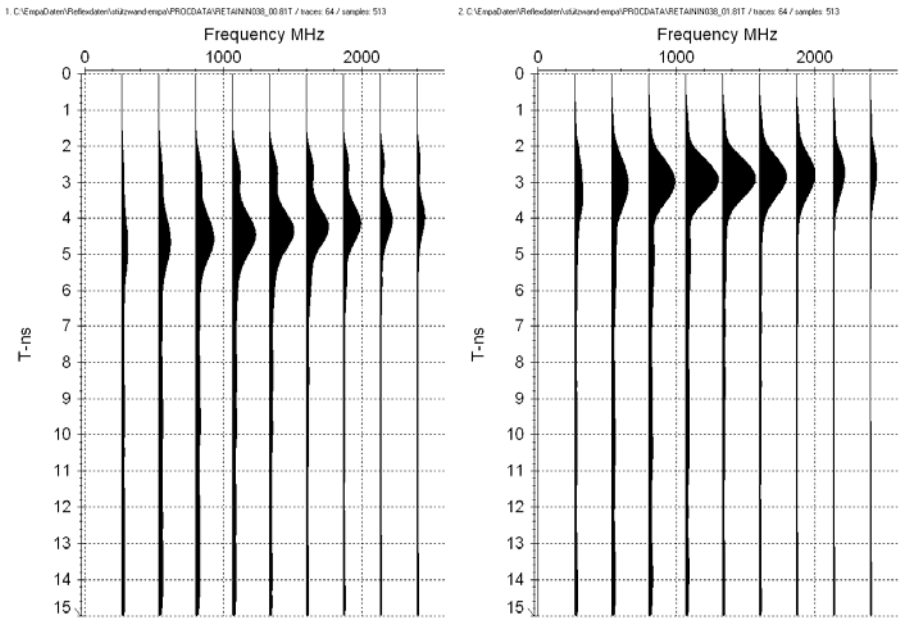

Figure 93: Moving window spectrum, horizontal E-field (left) and vertical E-field (right), direct wave/surface reflection removed, window length 2 ns.

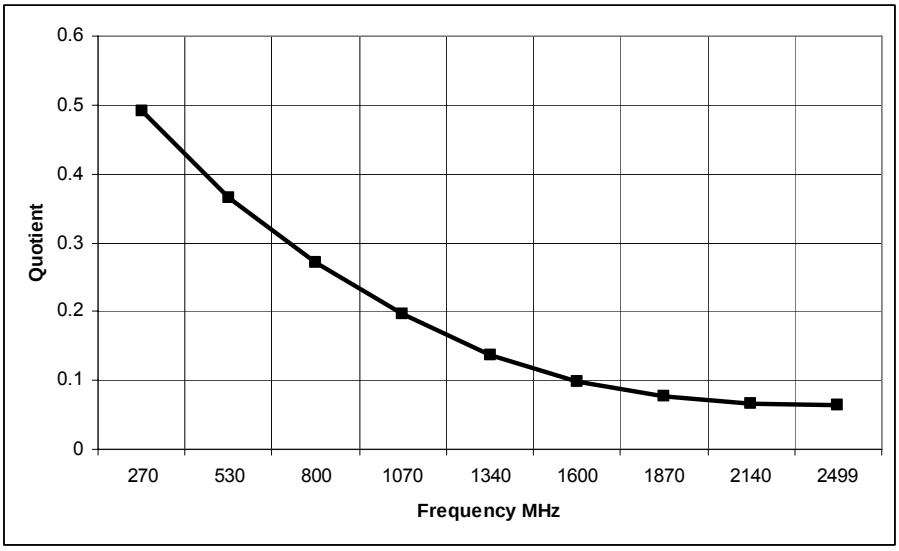

Figure 94: Quotient of maximum amplitudes in time gates 9-12 ns / 3.8-4.8 ns, horizontal E-field.

III. Processing strategies

The raw data were processed using three different strategies:

- Conventional 2-D processing using the horizontal E-field data only followed by the construction of a 3-D data set for the presentation of the data
- Full 3-D processing of the data sets collected by the two antennas followed by data fusion during which the two data sets were combined into one data set (Hugenschmidt and Kalogeropoulos, 2009)
- Inverse scattering followed by data fusion (Solimene et al., 2007)

The processing following the three processing strategies was carried out independently using the optimum processing parameters for the particular strategy.

In principle, it would have been possible to apply the data fusion also for the 2-D processing. It was decided not to fuse the data processed in 2-D to demonstrate a wide span of processing options from standard to advanced strategies.

The following section is divided in three subsections that describe the three strategies and present results for the 2-D vertical profiles.

2-D processing

The 2-D processing sequence was carried out using REFLEXW software from Sandmeier scientific software (Sandmeier, 2007; Yilmaz, 1987). Only data from the antenna with the horizontal E-field were used and processed with the following processing sequence:

- Band-pass filter applied in the frequency domain
- Correction of surface reflection/direct wave to time zero
- Kirchhoff migration assuming a dielectric permittivity of 6.25
- Background removal
- Gain

In addition all data sets were cut to the same length in the X-direction and time to facilitate the construction of the 3-D data set. In Figure 95 a vertical profile of the processed data set corresponding to the raw data in Figure 91 is presented. When comparing the processed data to the raw data it can bee seen that the signal to noise ratio has been improved and the diffraction hyperbolae caused by the rebar running in the Y-direction (horizontal bars) have been collapsed into dots.

3-D processing and data fusion

This processing strategy was implemented in three steps. First, 2-D processing was applied to each line acquired in the X-direction of the two data sets, then data were combined into two 3-D data sets (one for each antenna) for 3-D migration (Sandmeier, 2007; Yilmaz, 1987) and finally the two data sets were merged line by line.
The 2-D processing was applied line by line to the data sets of both antennas using REFLEXW software. The processing sequence consisted of a time shift, a Dewow (mean subtraction) filter, gain correction, background removal, spiking-deconvolution and an F-K filter. Deconvolution was applied mainly to increase resolution. The filter was calculated using a recursive autocorrelation algorithm (Levinson) on part of the traces (0-13 ns). This filter was then convolved with the original traces with 50% white noise added.

Following 2-D processing, lines were merged into the 3-D data sets separately for the two antennas. The data were migrated in 3-D using Stolt's algorithm and a signal velocity of 0.105 m/ns.

For the fusion of the two migrated data sets, three different strategies were tested. As the maximum and average algorithms described by Kohl et al. (2003) did not produce satisfactory results, the data sets were decomposed into five frequency ranges with the help of a Coiflet wavelet and fused as described by Hugenschmidt and Kalogeropoulos (2009). To achieve this, each trace was decomposed into sub-spaces using finite time, oscillating, zero mean signals called wavelets (Mallat, 1989). Numerous wavelets types are mentioned in the literature. After testing several families of wavelets (Daubechies, Symlets, Coiflets, Haar) it was concluded that Coiflet wavelets gave the best result. This is because, according to the literature, the shape of the wavelet should be as close as possible to the shape of the emitted radar pulse (Perrin et al., 2000). Then the corresponding sub-spaces from both traces (with the different antenna orientations) were merged using the wavelet fusion algorithm which can be considered as computing the average for the low frequency components and

the maximum for the high frequency components. This was followed by the reconstruction of the fused traces using the inverse wavelet transform. In Figure 96 the fused data set corresponding to the raw data sets in Figure 91 and Figure 92 is presented.

Inverse scattering and data fusion

In order to tackle the 3-D inverse scattering problem, a 2-D slice based inversion approach (Solimene et al., 2007) was applied separately to the two data sets acquired with the two antennas:

- Step-0: Preprocessing
- Step-1: Tomographic reconstruction of the 2-D data sets
- Following steps 0 and 1, data were transferred from 2-D to 3-D.
- Step-2: Superimposition and interpolation of the 2-D tomographic reconstructions to obtain the 3-D representation
- Step-3: The final 3-D reconstruction was obtained by "fusing" the two 3-D single polarization antenna results using a maximum algorithm

During step-0, the data were prepared for the tomographic reconstruction. First, the first part of the time domain traces corresponding to direct waves and surface reflections were set to zero. Then, data were transformed to the frequency domain before the inversion algorithm was applied Soldovieri et al., (2009, 2006, 2007) and Solimene et al. (2007).

During step-1, a microwave tomography based approach able to give focalized 2-D images of the rebar was applied to the two times 141 data sets. The algorithm is based on a linear model Born approximation for the electromagnetic scattering (neglecting the mutual interactions between the targets supposed invariant along the impinging/recording polarization direction) and works in the frequency domain. The result is given in terms of the modulus of the contrast function that accounts for the difference between the dielectric and conductive properties of the targets and those of the host medium (concrete hosting rebar). The regions where the modulus of the contrast function is significantly different from zero account for the presence, location and geometry of the buried targets. It is worthy noting that the adoption of a Born model inversion scheme allows to detect, to localize and to determine the geometry of an object also in the case of strong scattering (for which the Born model does not hold in principle), as already shown by a large number of numerical and realistic experiments (Soldovieri et al., 2006; Soldovieri et al., 2007).

The parameters used for the reconstruction are listed below.

- Model relative dielectric permittivity of the concrete: 9
- Model Conductivity of the concrete: 0.001 S/m
- Frequency band: 500-1500 MHz

- Frequency step: 50 MHz (21 frequencies exploited in the inversion)
- Investigation domain: 1.0 m (horizontal) and 0.02-0.52m (depth)

The fusion of the two 3-D data sets (step-3) was carried out by using the maximum value of modulus of the contrast function of the two separate 3-D reconstructed data sets. In Figure 97, a section of the inverted and fused data set corresponding to the raw data sets in Figure 91 and Figure 92 is presented.

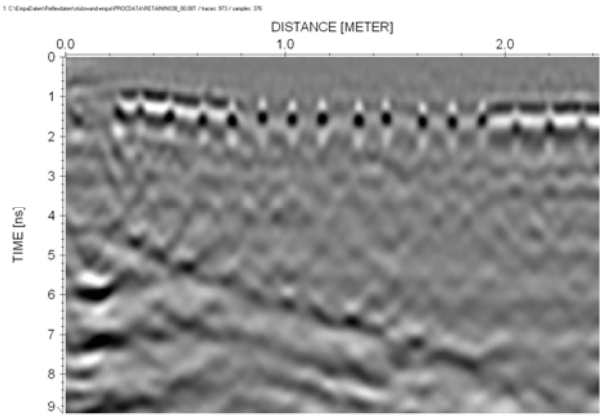

Figure 95: Data set after 2-D processing, horizontal E-field, y=0.37 m.

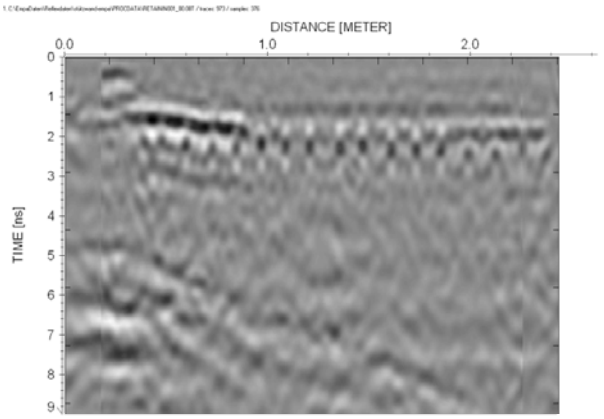

Figure 96: Data set after 3-D processing and data fusion, horizontal and vertical E-field, y=0.37 m.

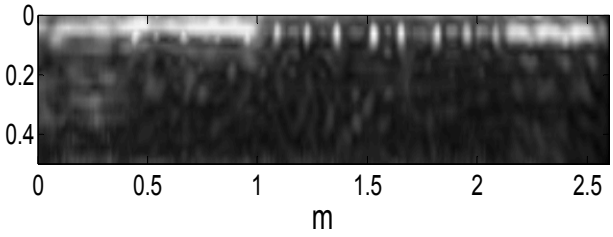

Figure 97: Data set after inverse scattering and data fusion, horizontal and vertical E-field, y=0.37 m.

IV. 3-D Results

This Section is devoted to show and compare the reconstruction results of the three strategies in terms of 3-D pseudo representations. In particular, the Section is divided in two Subsections related to the investigation of two different layers of rebar. One of those layers is at shallow depth (top layer) and a second layer it at greater and varying depth (second layer of rebar).

Top layer of rebar

The results of the 2-D processing are presented as a time-slice and a 3-D cube in Figure 98 and Figure 99, respectively. The horizontal rebar (rebar in Y-direction) is mapped reasonably whereas the vertical bars (bars in X-direction) are of low amplitude and poorly resolved. This is due to the fact that only the antenna with the horizontal E-field (E-field in Y-direction) was used and that data were migrated only in the X-direction.

In Figure 100 and Figure 101 the data after 3-D processing and data fusion are presented. When comparing Figure 100 to Figure 98, the most obvious difference is related to the vertical (X-direction) rebars which are now mapped with a similar quality as the horizontal bars due to true three-dimensional migration and the exploitation of the multi-polarization data. In addition, increased reflection amplitudes are perceptible in the top and bottom sections of the wall and an additional reflection, most likely caused by a distance piece, becomes visible (arrow).

The combination of inverse scattering and data fusion leads to the result presented in Figure 102 and Figure 103. In the depth slice presentation of the data set, the reconstruction of the vertical and horizontal bars are of the same quality and an improvement of the image quality at the top and bottom sections of the wall is evident. Accordingly, the rebar appears clearer and better focused and the reason for the increased reflection amplitudes visible in the top section of Figure 100 becomes obvious.

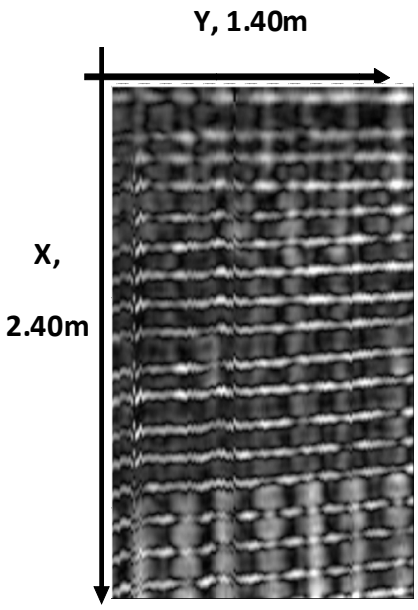

Figure 98: Time slice, t=1.45-1.95 ns, 2-D processing.

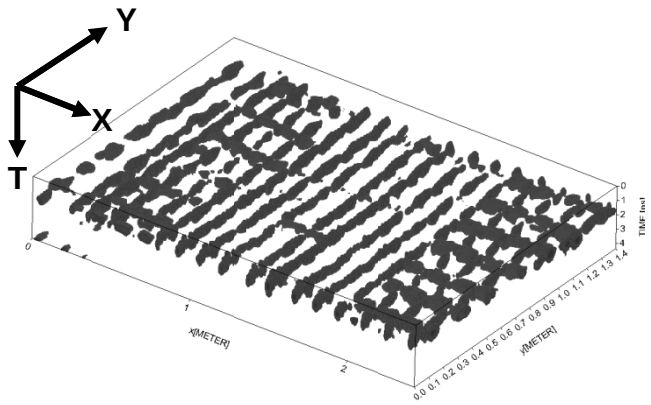

Figure 99: Data cube 0-4 ns, 2-D processing.

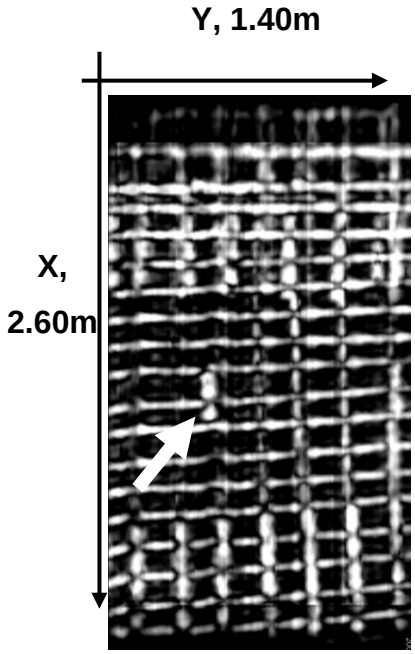

Figure 100: Time slice, t=1.45-2.08 ns, 3-D processing and data fusion.

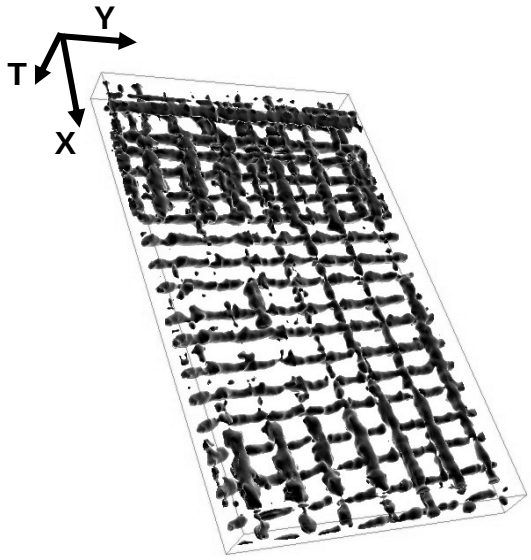

Figure 101: Fused data set after 3-D processing and data fusion, 0.5-3.5 ns.

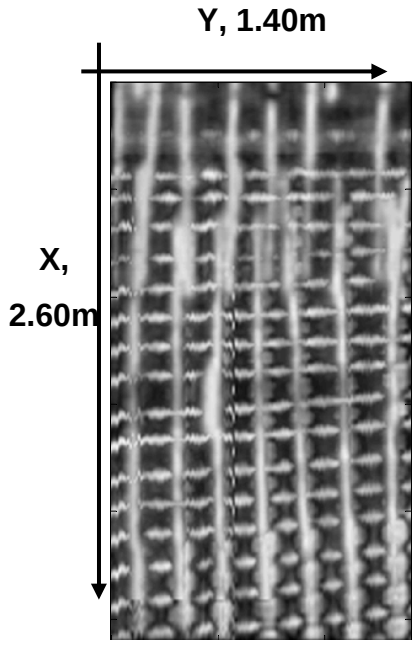

Figure 102: Depth slice, depth=6 cm, inverse scattering and data fusion.

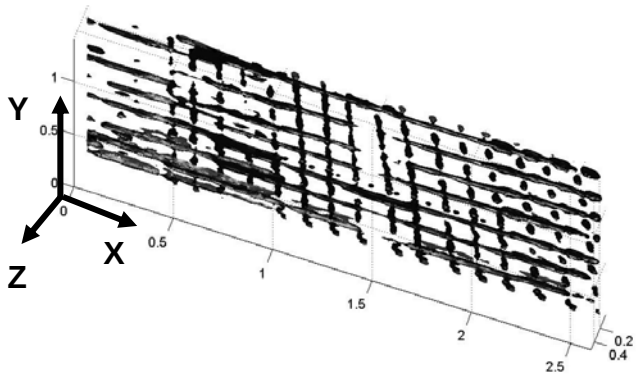

Figure 103: Data cube, 0.0-0.5 m., inverse scattering and data fusion.

Second layer of rebar

In Figure 104 the raw data set recorded with the horizontal E-field at position y=0.37 m is presented. The white line dipping from t=7.0 ns at x=0.00 m to t= 11.8 ns at x=2.40 m shows the suspected position of a second layer of rebar (see also Figure 91 and Figure 95 for comparison). This suspected position shifts to t=4.0 ns at x=0.00 m and t=8.8 ns at x=2.40 m for the processed data set because of the correction of the surface reflection/direct wave to time zero during the 2-D processing. Plotting a time slice following this line using the data that were processed with the 2-D processing sequence results in Figure 105. When comparing this time-slice to the time slice showing the top layer of rebar (Figure 98) it is obvious that resolution and focus have decreased. However, it is still possible to make out the horizontal bars of a second layer of rebar. This is confirmed by the presentation of the data cube in Figure 106 where, despite of the presence of noise, the horizontal bars are clearly visible.

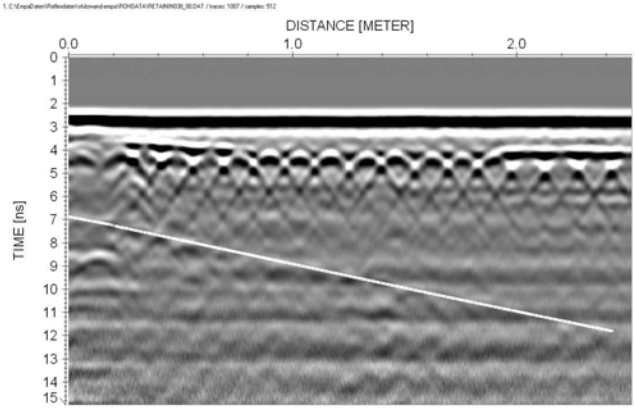

Figure 104: Raw data set, horizontal E-field, y=0.37 m, with position of time slice (white line).

In Figure 107 the time-slice after 3-D processing and data fusion corresponding to the dipping line in Figure 104 is presented. When comparing this result with the result for the top layer it becomes obvious that the signal/ noise ratio has decreased significantly. Both, vertical and horizontal bars can be made out. In addition there is an increased response from the points where vertical and horizontal bars are crossing because of the constructive interference of the data from the two antenna orientations.

In Figure 108 a depth slice after inverse scattering and data fusion is shown for the second layer of rebar. Again, the signal/noise ratio has decreased significantly when compared to result of the top layer (Figure 102) but both horizontal and vertical bars can still be made out.

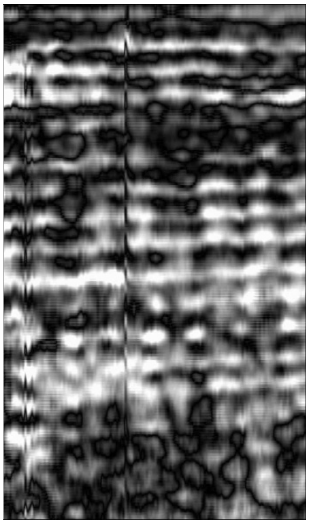

Figure 105: Time slice, 4.0–8.8 ns, 2-D processing.

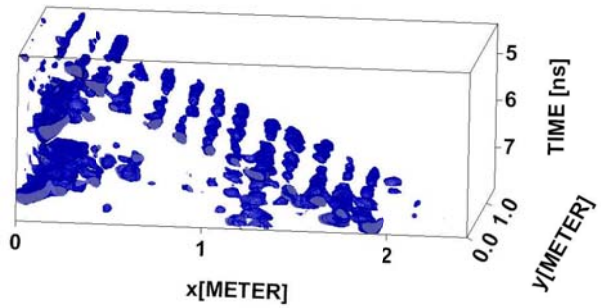

Figure 106: Data cube 4.5-8.0ns, 2-D processing.

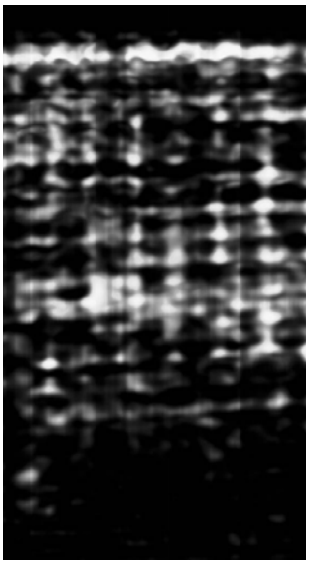

Figure 107: Timeslice, 4.0–8.8 ns, 3-D processing and data fusion.

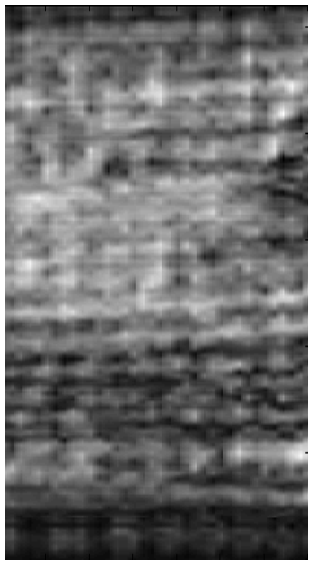

Figure 108: Depth slice, 0.18-0.40 m, inverse scattering and data fusion.

V. Summary and conclusions

A multi-sensor, multi-polarization data set was acquired on a concrete retaining wall. The decay of higher amplitudes with increasing two-way-traveltime was demonstrated thus characterizing the concrete structure as a low pass filter.

The data set was processed using three different approaches, classical 2-D processing followed by the construction of a 3-D data cube, full 3-D processing followed by data fusion and inverse scattering followed by data fusion.

The 2-D processing using the data from one antenna only provided for the top layer of rebar a detailed mapping of the horizontal rebar and a low amplitude and low focus result for the vertical bars.

The 3-D processing followed by data fusion resulted in a complete map of both, horizontal and vertical rebars for the top layer of rebar.

The inverse scattering approach followed by data fusion provided for the top layer of rebar a complete map of both, horizontal and vertical rebars. In addition, the reason for increased reflection amplitudes in some areas was elucidated.

All three processing approaches produced a result of lower quality for the second layer of rebar. It is assumed that is mainly due to the fact that the concrete structure is acting as a low pass filter for increased two-way-traveltimes and because of the masking effect of the top layer of rebar. In other words, the result for the second layer of rebar shows rather the limits of the data set than the limit of the different processing algorithms.

Acknowledgements

Special thanks to Roman Mastrangelo, formerly EMPA, for his support during data acquisition and to the building department of the city of Duebendorf for providing the original building plans of the wall.

6 Conclusions and outlook

6.1 Conclusions

Switzerland has an extensive network of roads and railway lines. The network has reached or exceeded its capacity at many locations. Due to large traffic volumes and the age of the network, there is a need for repair and reconstruction at many locations. Optimization of repair measures is of great importance for minimizing obstruction to traffic flow and costs.

In a study carried out on a Swiss motorway it was shown that the thickness of pavements can be inspected using a mobile GPR unit travelling under traffic conditions. Damage in pavements can be located and the effectiveness of repair measures can be evaluated.

An evaluation of GPR as an inspection tool for railway ballast was carried out. Three different railway lines with a total length of 15.1 km were inspected. Validation of GPR results with numerous trenches that were not available until after interpretation of the GPR data, showed that the estimates of the thickness of the ballast were of high accuracy almost everywhere. Subsoil material penetrating into the ballast was reliably identified. Thus, it was demonstrated that the use of GPR can reduce the number of trenches required for ballast inspections considerably.

Several bridges designated for demolition were inspected with the mobile GPR unit. GPR results were made public before manual measurements were carried out on exposed bridge parts. The concrete cover of the top layer of rebar was determined with GPR along 77% of the inspected sections. The mean difference between GPR results and reality was 10 mm. Gaps in the results for the concrete cover were mainly the result of resolution problems in sections with a small cover of rebar and of interpretation uncertainties in areas with additional structural complexity. No information about deeper layers of rebar was obtained when the mobile acquisition unit was used. The total pavement thickness was determined with GPR along 95% of the inspected sections. The mean difference between GPR results and reality was 9 mm. Gaps in the results for the pavement thickness were mainly due to a small concrete cover of rebar resulting in overlapping reflections from the bottom of the pavement and the rebar. During a manual GPR survey (i.e. not with the mobile GPR unit) of a bridge deck, data were interpreted directly on site. The positions of tendon ducts were determined with errors of less than 50 mm. This way, it was demonstrated that GPR is a powerful tool for bridge inspections and that the accuracy and reliability are sufficient for several applications.

An apparatus was developed for the inspection of retaining walls. It enabled an efficient data acquisition on large and small walls with a high positioning accuracy. Depending on the height of the wall, between 30 and 40 vertical lines were acquired per hour. In a study carried out on a large wall next to a motorway, it was possible to map accurately several layers of rebar and additional structures (e.g. dowels). Although several anomalous reflectors were found at each level of the wall, it was not possible to decide whether these were related to

rock anchors or not, based on the GPR data alone. This demonstrated that retaining walls can be inspected efficiently with GPR. However, for some problems additional information is required for an optimal interpretation of GPR data.

A multi-sensor, multi-polarization, high-resolution data set acquired on a concrete wall was processed using three different approaches: (I) Classical 2-D processing followed by the construction of a 3-D data cube, (II) full 3-D processing followed by data fusion and (III) inversion based on inverse scattering theory followed by data fusion. The 2-D processing using data from one antenna provided a detailed map of the near surface layer of horizontal rebar but only a low amplitude and poorly focussed result for the vertical bars. The 3-D processing followed by data fusion resulted in a complete map of both horizontal and vertical bars. The inverse scattering approach followed by data fusion also provided a complete map of both horizontal and vertical rebar. In addition, the reason for increased reflection amplitudes in some areas was elucidated. All three processing approaches produced a lower quality result for the second deeper layer of rebar. It was assumed that was mainly due to the fact that the concrete structure acted as a low pass filter and because of the masking effect of the top layer of rebar. The study demonstrated that advanced processing methods can significantly support the interpretation of GPR data acquired on concrete structures. The result for the second layer of rebar shows the limits of the data set rather than the limits of the different processing algorithms.

6.2 Outlook

In an ongoing project funded by the Swiss National Science Foundation (Non-destructive-detection of chlorides and moisture in multi-layer-structural elements such as concrete bridge decks using high frequency electromagnetic waves, grant 200021-119797/1), the detection of chlorides and moisture in concrete bridge decks is being investigated by the author's group. This includes the production of concrete probes that are exposed to chloride solutions in order to produce chloride gradients. This is a more realistic approach than the one described in chapter 3, where salt was added to the concrete mixture before casting the specimens. GPR data are being treated using advanced methods, such as inversion. A field test on an actual bridge will be used for an analysis of the benefits of different approaches.

In a research project funded by the European Union (ISTIMES - Integrated System for Transport Infrastructures surveillance and Monitoring by Electromagnetic Sensing, Joint Call FP7-ICT-SEC-2007-1, grant 225663) an autonomous mobile system for the acquisition of GPR data is being developed. The idea is to mount this system to a vehicle that is travelling on roads for other reasons, such as regular busses or lorries. This requires the implementation of an automated GPS-based positioning system and synchronization with the GPR unit. The GPR unit will collect densely spaced data which have to be processed to reduce the data volume that will be transferred to the remote control site. A data model has to be developed

for the storage and evaluation of the data. Criteria have to be defined to facilitate automated alarms with respect to unexpected changes in the target structure.

Acknowledgements

The author wishes to express his gratitude to Prof. Dr. Alan Green, Prof. Dr. Hansruedi Maurer and Prof. Dr. Eugen Brühwiler for their comments on this thesis. The case studies presented in this thesis were carried out within the framework of numerous service contracts and research projects. Thanks to the clients and awarding authorities for their trust and the permission to publish the results. Thanks to my colleagues at EMPA for their backing. Special thanks to Roman Mastrangelo, formerly EMPA, for his support during data acquisition, sometimes under harsh conditions.

References

1. ASTM (2005a) Standard Test Method for Deflections with a Falling Weight Type Impulse Loading Device, Book of Standards 04.03, D4694.96
2. ASTM (2005b) Standard Guide for Using the Surface Ground Penetrating Radar Method for Subsurface Investigation, Book of Standards 04.09, D6432 – 99
3. ASTM (2005c) Standard Test Method for Evaluating Asphalt-Covered Concrete Bridge Decks Using Ground Penetrating Radar, Book of Standards 04.03, D6087 – 03
4. Baker M. R., Crain K., Nazarian S. (1995) Determination of pavement thickness with a new ultrasonic device, Research Report 1966-1, Center for Highway Materials Research, University of Texas, El Paso, USA
5. Barnes C, Trottier JF (2004) Effectiveness of Ground Penetrating Radar in Predicting Deck Repair Quantities, Journal of infrastructure systems 10(2): 69-76
6. Canton Uri (2010) www.ur.ch, website accessed on July 28, 2010
7. Capizzi P., Cosentino P.L. (2008) GPR multi-component data analysis, Near Surface Geophysics 6: 87-95
8. Cardimona S., Willeford B., Wenzlick J., Anderson N. (2000) Investigation of Bridge Decks utilizing Ground Penetrating Radar., Int. Conf. on the Application of Geophysical Technologies to Planning, Design, Construction and Maintenance of Transportation Facilities, St. Louis, USA
9. Crawford F. S. (1968) Waves, Berkeley physics course Vol3, McGraw-Hill, New York, USA
10. Daniels D. (2004) Ground Penetrating Radar, 2nd edition, The Institution of Electrical Engineers
11. Davis J.L., Rossiter J.R., Mesher D., Dawley C. (1994) Quantitative Measurement of Pavement Structures using Radar, 5th International Conference on Ground Penetrating Radar, Kitchener, Canada, Waterloo Center for Groundwater Research: 319-334
12. DGZfP, Deutsche Gesellschaft für zerstörungsfreie Prüfung e.V. (2008) Merkblatt über das Radarverfahren zur zerstörungsfreien Prüfung im Bauwesen
13. Eide E., Hjelmstad J. (2002) 3-D utility mapping using electronically scanned antenna array, 9th International Conference on Ground Penetrating Radar, Santa Barbara, USA
14. Elcometer, www.elcometer.com, website accessed on March 30, 2010
15. Elsener B., Wojtas H., Böhni H. (1993) Inspection and monitoring of reinforced concrete structures – electrochemical methods to detect corrosion, 12th International Corrosion Congress, Houston: 3260-3270

16. Elsener B., Andrade C., Gulikers J., Polder R., Raupach M. (2003) Half-cell potential measurements – Potential mapping on reinforced concrete structures, Materials and Structures 36: 461-471
17. EN 12350-5 (2001) Testing fresh concrete – Part 5: Flow table test
18. EN 12350-7 (2001) Testing fresh concrete – Part 7: Air content – Pressure methods
19. EN 12390-3 (2002) Testing hardened concrete – Part 3: Compressive strength of test specimens
20. FEDRO (2009) Strassen und Verkehr, Zahlen und Fakten, Swiss Federal Roads Office
21. Geel L., Bosch F. (2009) personal communication
22. Gerthsen C., Kneser H.O., Vogel H. (1982), Physik, 14th edition, Berlin, Germany, Springer
23. Göbel, C., Hellmann, R., Petzold, H. (1994) Georadar-model and in-situ investigations for inspection of railway tracks, 5th International Conference on Ground Penetrating Radar, Kitchener, Canada, Waterloo Center for Groundwater Research: 1121-1133
24. GSSI (2006) www.gssi.com, website accessed on December 6
25. Guettala A., Abisi A. (2006) Corrosion degradation and repair of concrete bridge, Materials and Structures 39: 471-478
26. Hänninnen P., Hänninen, P., Koponen L., Koshkiahde A., Maijala P., Pollari R., Saarenketo T., Sutinen R. (1992) Ground Penetrating Radar, The Finnish Geotechnical Society, Finland
27. Hilti (2010) www.hilti.com, website accessed on March 30
28. Hugenschmidt J. (1996) Non-destructive inspection of roads using GPR, 2nd meeting environmental & engineering geophysics, Nantes, France: 224-227
29. Hugenschmidt, J., Partl, M. N., de Witte H. (1998) GPR inspection of a mountain motorway in Switzerland, J. Appl. Geophys. 40: 95-104
30. Hugenschmidt J. (2000a) Multi-Offset-Analysis for man-made structures, 8th International Conference on Ground Penetrating Radar, Gold Coast, Australia: 414-420
31. Hugenschmidt J. (2000b) Railway track inspection using GPR, Journal of Applied Geophysics 43: 147-155
32. Hugenschmidt J. (2002) Concrete bridge inspection with a mobile GPR system, Construction and Building Materials 16: 147 – 154
33. Hugenschmidt J. (2005) Zuverlässigkeit und Genauigkeit von Georadar-Ergebnissen auf Betonbrücken, Swiss Federal Roads Authority, Report Nr. 582
34. Hugenschmidt J., Mastrangelo R. (2006) GPR inspection of concrete bridges, Cement & Concrete Composites 28: 384-392

35. Hugenschmidt J., Mastrangelo R. (2007) The inspection of large retaining walls using GPR, 4th International Workshop on Advanced Ground Penetrating Radar, Naples, Italy: 267-271

36. Hugenschmidt J., Kalogeropoulos A. (2009) The inspection of retaining walls using GPR, Journal of Applied Geophysics 67: 335-344

37. Kohl Ch., Krause M., Maierhofer Ch. Mayer K., Wöstmann J., Wiggenhauser, H. (2003) 3-D-Visualisation of NDT-Data using Data Fusion Technique, International Symposium Non-Destructive Testing in Civil Engineering (NDT-CE), Berlin, Germany

38. Krause M., Milmann B., Mielentz F., Streicher D., Redmer B., Mayer K., Langenberg K.-J. Schickert M. (2008) Ultrasonic Imaging Methods for Investigation of Post-tensioned Concrete Structures: A Study of Interfaces at Artificial Grouting Faults and Its Verification, Journal of Nondestructive Evaluation, 27: 67-82

39. Langenberg K.J., Mayer K., Marklein R. (2006) Nondestructive testing of concrete with electromagnetic and elastic waves; Modeling and imaging, Cement & Concrete Composites 28: 370-383

40. Lehmann F. (1999) Automation in 3-D Georadar Investigations: New Acquisition and Processing Techniques, PhD thesis, Swiss Federal Institute of Technology (ETH), Zurich, Switzerland

41. Mallat S. (1989) A theory for Multiresolution Signal Decomposition: The Wavelet Representation, IEEE Trans. On Pattern Analysis and Machine Intell. 11: 674-693

42. Maser K. R. (1994) Ground Penetrating Radar Surveys to Characterize Pavement Layer Thickness Variations at GPS Sites, Strategic Highway Research Program, Report SHRP-P-397

43. Maxwell J. C. (1865) A Dynamical Theory of the Electromagnetic Field, Philosophical Transactions of the Royal Society of London, London, UK

44. Montemor M.F., Simões A.M.P., Ferreira M.G.S. (2003) Chloride-induced corrosion on reinforcing steel: from the fundamentals to the monitoring techniques, Cement & Concrete Composites 25: 491-502

45. Morris W., Vico A., Vazquez M. de Sanchez S.R. (2002) Corrosion of reinforcing steel evaluated by means of concrete resistivity measurements, Corrosion Science 44: 81-99

46. Nazarian S. Milind R. D. (1993) Automated surface wave method: field testing, Journal of Geotechnical Engineering 119: 1094 – 1111

47. NCHRP (2008) Falling Weight Deflectometer Usage, 2008, National Cooperative Highway Research Program, Synthesis 381, Transportation Research Board, Washington D.C., USA

48. Neville A.M. (1995) Properties of concrete, 4th edition, Longman, Essex

49. OsiriX Imaging Software (2008) www.osirix-viewer.com, Open source, version 3.1, website accessed on May 19

50. Parry N.S., Davis J.L. (1992) GPR Systems for Roads and Bridges, 4th International Conference on Ground Penetrating Radar, Rovaniemi, Finland: 247-257

51. Perrin S., Bibaut A., Duflos E., Vanheeghe P. (2000) Use of wavelets for Ground-Penetrating Radar Signal Analysis and Multisensor Fusion in the Frame of Landmines Detection, IEEE International Conference on Systems, Man, and Cybernetics 4: 2940-2945

52. Pourbaix M. (1966) Atlas of electrochemical equlibria in aqueous solutions, Oxford, Pergamon Press

53. Proceq (2010) www.proceq.com, website accessed on March 30

54. Roberts G. (2002) Use of ground penetrating radar to delineate bridge deck repair areas, New Hampshire Department of Transportation, Report Nr. FHWA-NH-RD-12323S

55. Roddis W. M., Maser K., Gisi A. J. (1992) Radar Pavement Thickness Evaluations for Varying Base Conditions, Transportation Research Record 1355, National Academy Press, Washington D.C.: 90-98

56. Rodriguez M., Rychen P., Dumont A.G. (2008) Applicabilité de l'enrobe drainant sur les ouvrages d'art du réseau des routes nationales, Swiss Federal Roads Office, Report Nr. 635

57. Sandmeier K. J. (2010) Reflexw manual ver. 5.5 from 25.01.2010, Sandmeier scientific software, Karlsruhe, Germany, older versions referred to as Sandmeier 2007

58. Sbartai Z.M., Viriyametanont K., Laurens S. (2008) NDE of Reinforced Concrete – Inversion of GPR Data using Neural Approach, 12th International Conference on Ground Penetrating Radar, Birmingham, UK

59. SBB – Geschäftsbericht (annual report) 2008

60. SBB – Network Statement 2010

61. Schechinger B., Vogel T. (2007) Acoustic emission for monitoring a reinforced concrete beam subject to four-point-bending, Construction and Building Materials 21: 483-490

62. Scheff J., Chen R. (2000) Bridge deck inspection using chain drag and ground penetrating radar, In: Ansari F. (ed) Condition monitoring of materials and structures, American Society of Civil Engineers

63. Schickert G., Krause M., Wiggenhauser H. (2010) ZfPBau-Kompendium – Verfahren der Zerstörungsfreien Prüfung im Bauwesen www.bam.de/microsites/zfp_kompendium/welcome.html, website accessed on March 30

64. Sensors & software (2006) www.sensoft.com, website accessed on December 6

65. Shin H., Grivas A.D. (2003) How accurate is Ground Penetrating radar (GPR) for Bridge Deck Condition Assessment?, 82nd Annual Meeting of the Transportation Research Board, Washington D. C. , USA

66. Smith S., Scullion T. (1993) Development of Ground-Penetrating Radar Equipment for Detecting Pavement Condition for Preventive Maintenance, Strategic Highway Research Program, Report SHRP-H-672

67. Soldovieri F., Hugenschmidt J., Persico R., Leone G., (2007) A linear inverse scattering algorithm for realistic GPR applications, Near Surface Geophysics 5: 29-42

68. Soldovieri F., Persico R., Utsi E., Utsi V. (2006) The application of inverse scattering techniques with ground penetrating radar to the problem of rebar location in concrete, NDT&E International 39: 602-607

69. Soldovieri F., Prisco G., Hugenschmidt J. (2009) Microwave tomography for GPR diagnostics of reinforced concrete, European Microwave Week 2009, Rome, Italy

70. Solimene R., Soldovieri F., Prisco G., Pierri R., (2007) Three-Dimensional Microwave Tomography by a 2-D Slice-Based Reconstruction Algorithm**,** IEEE Geoscience and Remote Sensing Letters 4: 556 – 560

71. Swiss Association of Road and Transportation Experts, VSS (2008) Swiss Standard SN 640430

72. Swiss Association of Road and Transportation Experts, VSS (2000) Swiss Standard SN 640302

73. Taffe, A., Borchhardt, K., Wiggenhauser, H. (2003) Specimen for the improvement of NDT-methods, design and construction of a large concrete slab for NDT methods at BAM, International Symposium Non-Destructive Testing in Civil Engineering (NDT-CE), Berlin, Germany

74. Trimble (2001a) Trimble 5700 GPS Receiver – User Guide, 2001-a, Trimble Navigation Limited

75. Trimble (2001b) Trimble Survey Controller – User Guide, Trimble Navigation Limited

76. Ulriksen C. P. F. (1982) Application of impulse radar to civil engineering, Doctoral thesis, Lund University of Technology, Lund, Sweden

77. Van Deveer JR (1975) Techniques for evaluating reinforced bridge decks, ACI Journal 12: 697-704

78. Watanabe S., Misra S., Oumoto T (2003) Nondestructive evaluation of concrete structures, International Symposium Non-Destructive Testing in Civil Engineering (NDT-CE), Berlin, Germany

79. Wiggenhauser H. (2003) Duct inspection using scanning impact-echo, International Symposium Non-Destructive Testing in Civil Engineering (NDT-CE), Berlin, Germany

80. Xia J., Miller R., Park C. (1999) Estimation of near-surface shear-wave velocity by inversion of Raleigh waves, Geophysics 64: 691-700

81. Yilmaz O. (1987) Seismic Data Processing, Society of Exploration Geophysicists, Tulsa, USA

82. Yuan D., Nazarian S. (1993) Automated surface wave method: inversion technique, Journal of Geotechnical Engineering 119: 1112-1126

83. Yuyama S., Yokoyama K., Niitani K., Ohtsu M., Uomoto. T. (2007) Acoustic emission for monitoring a reinforced concrete beam subject to four-point-bending, Construction and Building Materials 21: 491-500

7 Appendix A - Symbols and constants

B	**B** = $\mu\mu_0$**H** (not valid for ferromagnetic materials)
c	c=speed of light in a vacuum=2.998 · 10^8 m/s
d	thickness of a layer or depth of a target
D	**D** = $\varepsilon\varepsilon_0$ **E**
E	electric field
ε	relative permittivity of a medium
ε_0	absolute permittivity of free space = 8.85 · 10^{-12} C/Vm
H	magnetic field
λ	wavelength
f	frequency
R	coefficient of reflection
t	two way traveltime
ω	angular frequency
μ	relative permeability of medium
μ_0	absolute permeability of free space = 1.26 · 10^{-6} Vs/Am

8 Appendix B - GPR inspection of a mountain motorway in Switzerland

Johannes Hugenschmidt, Manfred Partl and Hans de Witte

Journal of Applied Geophysics 40 (1998): 95–104

Abstract

A radar survey was carried out to support the planning of maintenance work on Switzerland's Gotthard Motorway. This work became necessary after damaged pavement layers had been detected by visual inspection and coring. Radar data acquisition, processing and interpretation focused on the investigation of pavement damage. However, additional information such as layer thicknesses and the position of the rock surface could be extracted from the acquired data set. Results of the radar survey were verified by local coring and during repair work. The radar survey proved to be a useful complement to traditional pavement monitoring methods providing not only quasi-continuous information between boreholes but also locating previously unknown problem zones. The comparison between data sets that were acquired before and after the maintenance work suggests the success of the repair work and the suitability of GPR as a quality control tool.

Keywords: GPR; pavement inspection; non-destructive testing; pavement maintenance; quality control

Introduction

In recent years GPR inspection of roads has evolved as a powerful technique offering several advantages when compared to traditional methods (Hugenschmidt, 1996; Davis et al., 1994; Parry and Davis, 1992; Roddis et al., 1992). In particular it is non-destructive, the results are quasi-continuous and data can be acquired at high rates. Traffic obstruction can be minimized or avoided. Important applications are the inspection of pavement layer thicknesses and pavement damage, the investigation of sub-pavement structures and locating reinforcement-bars and damage in concrete structures such as bridges. The Section of Road Engineering/ Sealing Components of the Swiss Federal Laboratories for Materials Testing and Research (EMPA) is investigating roads and bridges using GPR in both research studies and routine contract work. This paper presents the GPR inspection of a section of Switzerland's National Motorway N2. The data acquisition, processing and interpretation are presented together with results to provide an example of a practical GPR application.

Gotthard motorway, GPR section

Switzerland's Gotthard Motorway (National Motorway N2) is one of the main North-South routes in Central Europe crossing the Alps (Figure 109), connecting the industrial areas of Northern Italy to Northern Switzerland and Southern Germany. In summer it is one of the main tourist routes to the summer resorts in Italy and Southern Switzerland. Since the completion of a 17 kilometers long tunnel at an altitude of 1100 meters in 1980 this road can be used all year round whereas many other North-South routes have to be closed in winter.

The inspected section is situated north of the tunnel between the villages of Amsteg and Wassen. Its northern part follows a narrow part of the Reuss valley and is characterized by tunnels and bridges whereas in the southern part the valley is wider with only some sections of the road running through avalanche galleries and over bridges.

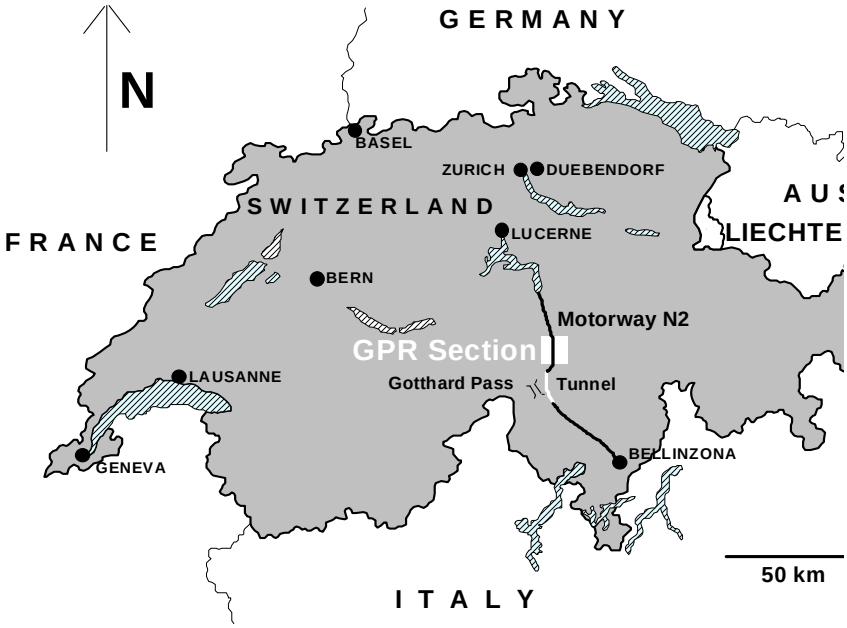

Figure 109: Geographical situation.

Problem description

The three types of asphalt pavement damage requiring rehabilitation and leading to the GPR inspection were:

a) separation between pavement layers; in Figure 110 (left) a core is shown that could be retrieved only partially due to separation between pavement layers

b) porous zones mostly filled with water leading to frost damage and pavement deterioration (Figure 110, right)

c) cracks visible on the pavement surface (the cracks had been sealed with sealing material some time before the radar survey)

Prior to the radar survey the damages had been detected and investigated by coring (damage types a and b) and visual inspection (type c). Due to the destructive nature of coring the spacing between drilling locations had been chosen as some hundred meters. This provided a detailed knowledge of the pavement conditions at the coring locations but did not give sufficient information about the horizontal extension and maximum depth of pavement damage. In addition, the possible existence of damaged pavement zones undetected by the coring campaign could not be ruled out.

The aim of the radar survey was to support the planning of maintenance work by providing additional information required for deciding where and to what depth the pavement had to be replaced.

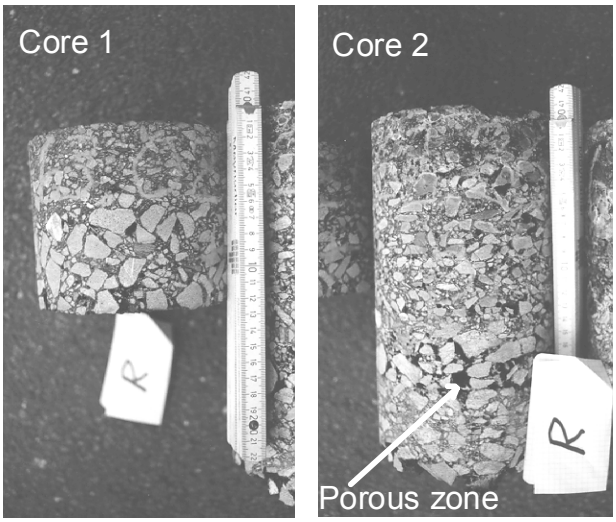

Figure 110: Two cores showing layer separation (left) and a porous zone (right).

Data acquisition

Data were acquired on February 26, 1996 along six profiles of 9.4 km each. The equipment used consists of a pair of 2.5 GHz horn antennas (GSSI Model H4205), a 900 MHz antenna (GSSI Model 3101D) and a GSSi SIR SYSTEM-10A. Figure 111 shows the vehicle with the horn antennas mounted on a plastic rack. The 900 MHz antenna is mounted at the rear. Two channels (2.5 GHz and 900 MHz) were recorded simultaneously whilst travelling at 50 km/h under traffic conditions. Data were stored on tape without any processing applied. The acquisition parameters can be summarized as follows:

- acquisition speed: 50 km/h = 13.9 m/s
- scan rate: 50 scans/s for each channel
- data word length: 16 bits

- samples per scan: 512
- antenna height: 0.25 m (2.5 GHz), 0.15 m (900 MHz)
- scan length: 15 ns (2.5 GHz), 20 ns (900 MHz)

Antenna heights were measured between the lowest point of the antenna casing and the road surface.

In June 1996, data were acquired on a 830 m long section directly after pavement repair had been completed. As the road was still closed after the repair work, the travelling speed could be reduced to 30 km/h.

Figure 111: Vehicle mounted horn antennas

Data processing

Data were copied to a personal computer for processing. As the data were zero-offset and single channel (the data of multiple antennas are handled independently) the processing sequence could be kept simple and focussed on the enhancement of the signal/noise ratio and the correction of the asphalt pavement surface reflection to time/depth zero. A typical processing sequence for 2.5 GHz data consisted of:

- editing
- horizontal inversion
- bandpass filtering
- resampling to 256 samples
- surface correction
- mean subtraction
- gain correction
- horizontal smoothing

In Figure 112 and Figure 113 a 2.5 GHz data set before and after processing is presented. There are two main differences:

- In the unprocessed data set the reflection resulting from the asphalt pavement surface is visible, showing small lateral variations in two-way-traveltime (TWT) due to changes in antenna height. During processing, the lateral variations were eliminated by conversion of this reflection into a straight, horizontal line. This step was followed by a time shift, thus establishing the pavement surface as a new reference at time zero.
- The processed data set shows an enhanced signal/noise ratio due to bandpass filtering, mean subtraction and horizontal smoothing. In addition, the signal strength of reflections arriving at later times was increased by gain correction.

To increase ease of comparison between data sets acquired in different directions, horizontal inversion was applied to southbound lane data.

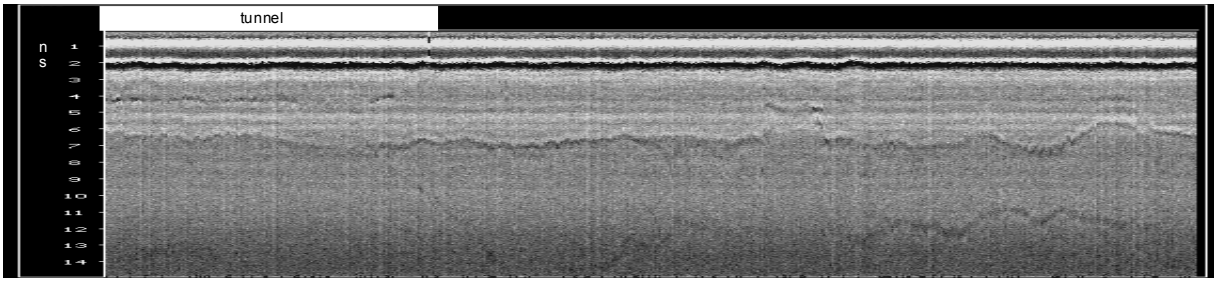

Figure 112: 2.5 GHz data set before processing, profile length 240 m.

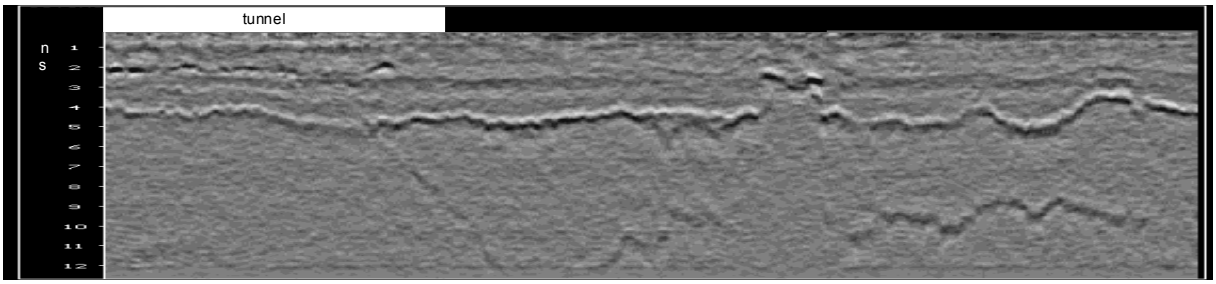

Figure 113: 2.5 GHz data set after processing, profile length 240 m.

Results

Overview

A 2000 m long 2.5 GHz profile from the northern part of the inspected section is shown in Figure 114. A prominent reflection varying between 2.7 and 4.9 ns in two-way-traveltime (TWT) is interpreted as the asphalt pavement base. Some reflections resulting from within the pavement can also be distinguished. On the bridges a prominent reflection can be seen at about 2.1 ns TWT.

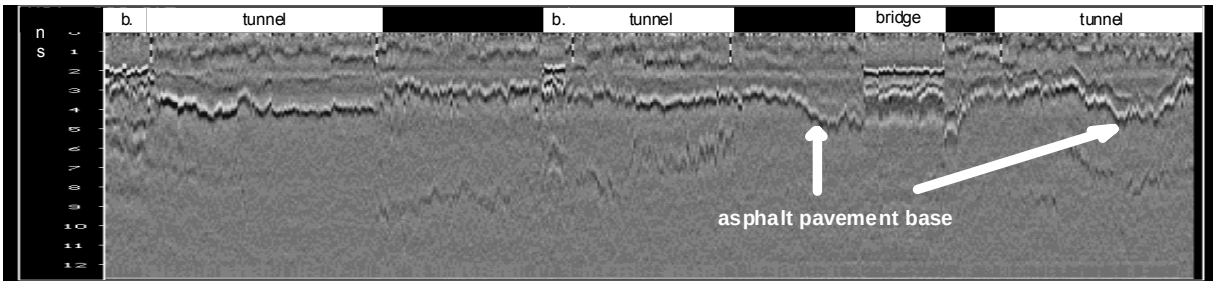

Figure 114: 2.5 GHz profile, length 2000 m, northern part, b.=bridge.

Figure 115 shows a 2000 m long interpreted section from the southern part where many cores were available. The signal velocity of $1.15 \cdot 10^8$ m/s used for the conversion from time to depth was calibrated using core information. The poor signal quality on the right hand side of the section shown could be attributed to damaged pavement (see section "pavement damage" for details).

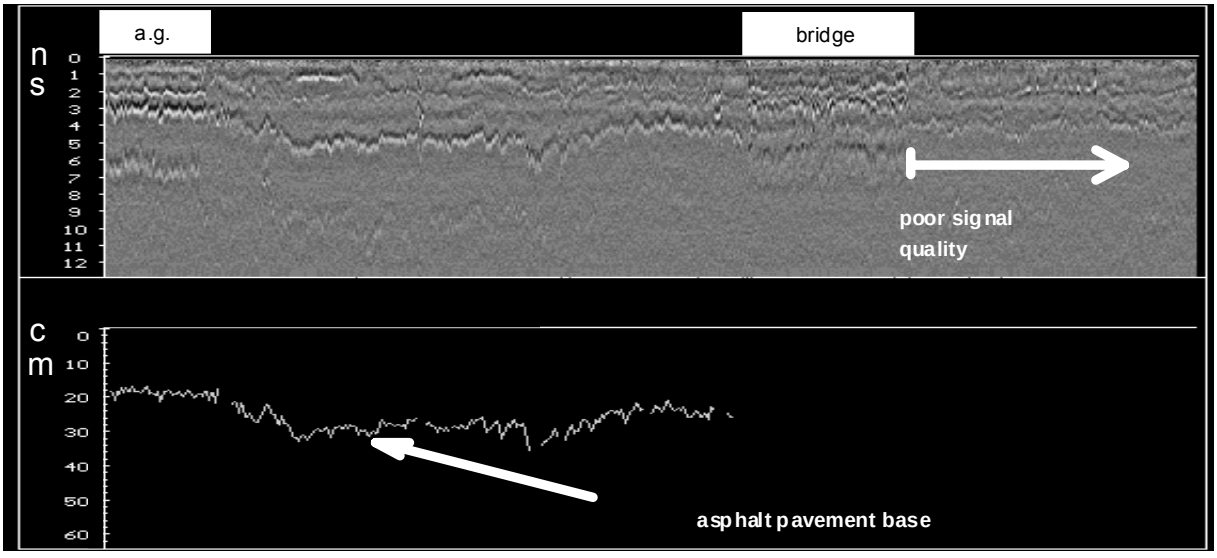

Figure 115: 2.5 GHz profile with interpretation, length 2000 m, southern part, a. g.=avalanche gallery.

Comparison between 2.5 GHz and 900 MHz results

A comparison between the 2.5 GHz and 900 MHz data sets is shown in Figure 116 and Figure 117. Please note that the road surface reflection has not been shifted to time zero in those two data sets. As the asphalt pavement thickness varies between 0.16 and 0.2 m ($v=1.15 \cdot 10^8$ m/s), the pavement base reflection can be easily distinguished from the surface reflection in both data sets. A reflection resulting from a pavement layer interface can be resolved with the 2.5 GHz antennas whereas the corresponding pattern in the 900 MHz data set is difficult to interpret because the reflections from the asphalt pavement base and the pavement layer boundary are overlapping. The rock surface reflection in the tunnel is clearly visible in both data sets. Outside the tunnel where the rock surface is dipping to greater depth the quality of the 2.5 GHz reflection deteriorates as the maximum depth of penetration is approached, on the other hand the 900 MHz antenna still provides good results. In other locations the 2.5 GHz antennas gave interpretable results for times over 12 ns, see Figure 113 for comparison.

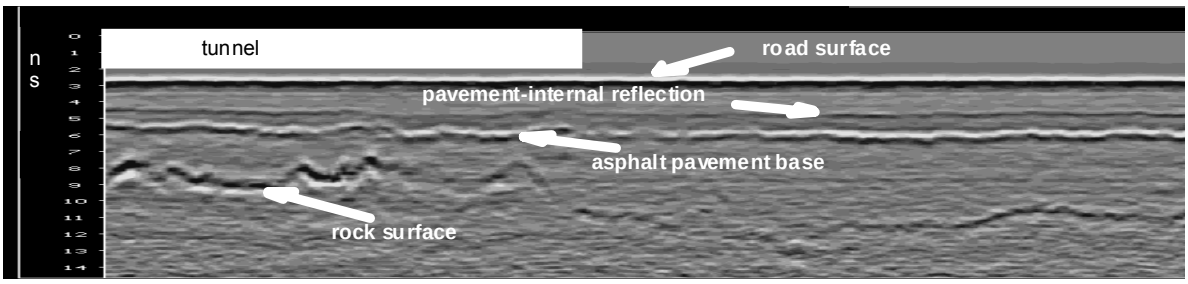

Figure 116: 2.5 GHz profile, length 120 m.

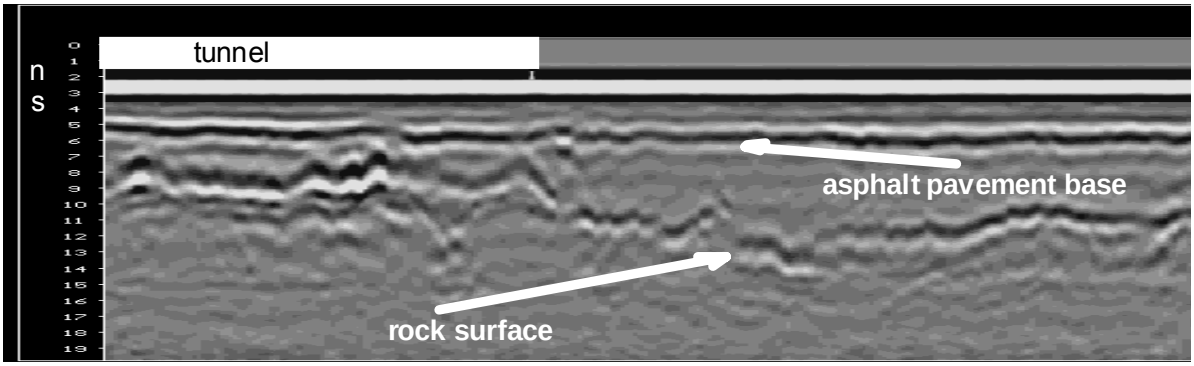

Figure 117: 900 MHz profile, length 120 m.

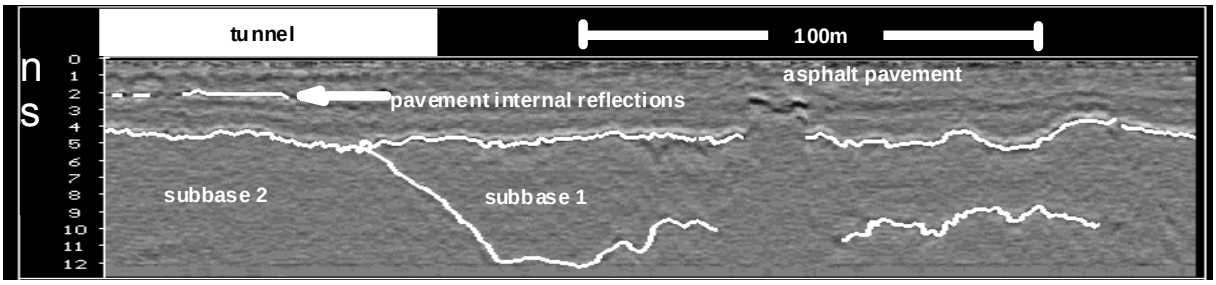

Figure 118: Interpreted 2.5 GHz profile, the uninterpreted profile is shown in Figure 113.

Pavement damage

The analysis of the radar data with respect to pavement damage was performed using two different approaches:

- The data sets were searched for sections with low intensity asphalt pavement base reflections as it was expected that saline water within pores or cracks would reduce the signal quality due to increased conductivity. De-icing salts had been applied to the road surface in the months preceeding the radar survey.
- The data sets were searched for interior pavement reflections that could be correlated with core information.

Pavement-internal reflections and low intensity pavement base reflections can be a result of other reasons than pavement damage. In Figure 118 the same data set as in Figure 113 is presented together with interpretation. A dipping reflection near the end of the tunnel is interpreted as resulting from a change in subbase. The interface between pavement and subbase 2 causes a reflection of lower intensity than the interface between pavement and subbase 1. In this case the reduced intensity pavement base reflection seems to be the result of a lateral change in subbase material and/or structure rather than pavement damage.

The pavement-internal reflection on the left of the data set presented is most likely due to a different pavement construction than pavement damage as asphalt pavements in tunnels are usually built differently than in the open.

To avoid pitfalls in interpretation, the co-operation between the geophysicist interpreting the radar data and the road engineer investigating the damages by other means was essential. The availability of additional information such as structural and material data was of great importance for the interpretation of the radar data.

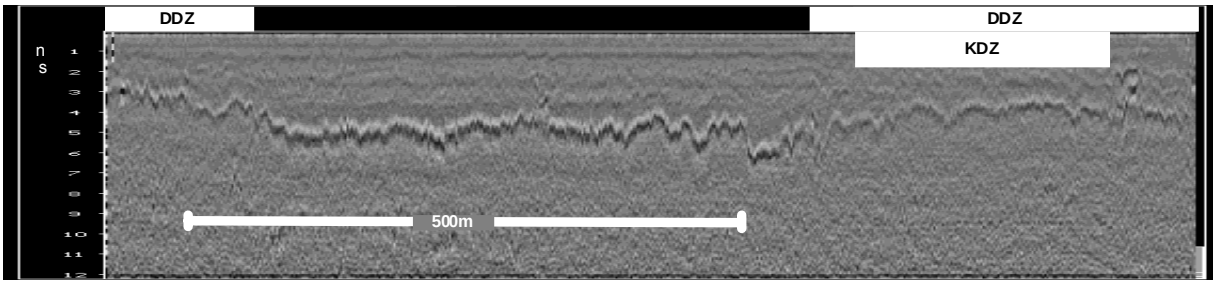

Figure 119: 2.5 GHz profile, length 980 m, a known distress zone (KDZ) and two detected distress zones (DDZ) based on the radar inspection are marked.

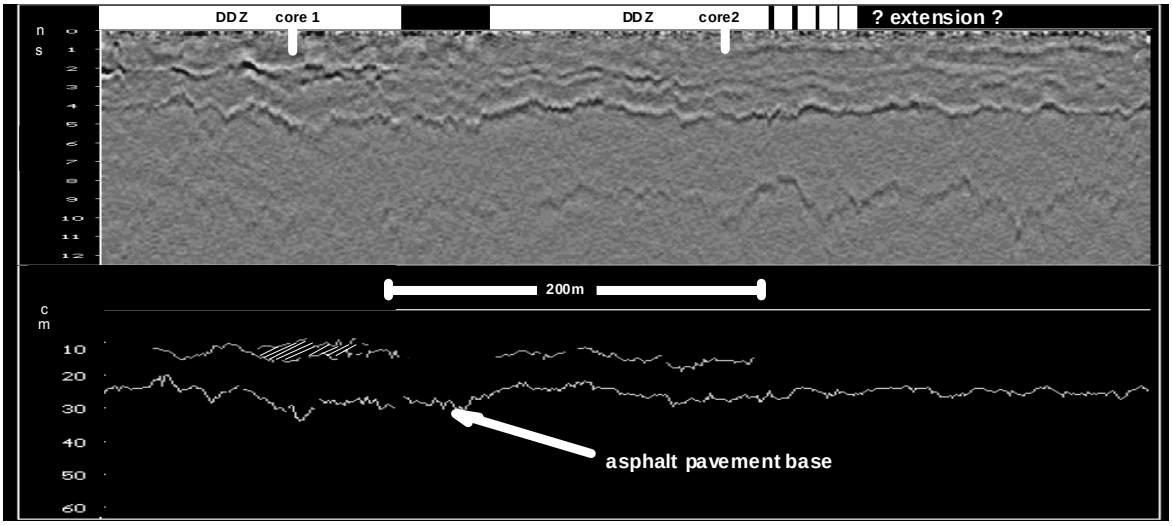

Figure 120: 2.5 GHz profile with interpretation, length 560 m, two distress zones (DDZ) are marked.

Successful applications of the two approaches described above are presented in Figure 119 and Figure 120. A zone where damages were visible on the road surface is marked as KDZ (Known Distress Zone) in Figure 119. When comparing the asphalt pavement base reflection in the distress zone with the reflection in the center of this section, a reduced reflection intensity extending beyond the known distress zone becomes obvious. Another zone showing similar characteristics marked as DDZ (Detected Distress Zone) can be seen on the left of the section. The existence of the additional distress zone on the left and the extension of the known distress zone beyond the limits defined by visual inspection were verified during repair work.

A typical example demonstrating correlation between pavement-internal reflections and cores is shown in Figure 120. Core 1 (see Figure 110, left) was retrieved only partially due to separation of pavement layers, in the data set the area surrounding the coring location shows an obvious reflection from within the pavement. Core 2 (Figure 110, right) revealed a porous zone between a depth of 16-19 cm. In the data set a reflection can be seen at the appropriate depth. In this case the extension of the problem zone to the right cannot be clearly defined without further information obtained by other methods.

A simplified version of the final map showing zones of pavement damage obtained by GPR, coring and visual inspection as drawn by the road engineer is shown in Figure 121. The length of the section shown is 3.3 km. There is a good correlation between the different results. The radar inspection provided information on the horizontal extent of damaged zones detected by coring and located previously unknown distress zones. In addition, the depth of pavement damage was determined in many locations. This was important in deciding to which depth the pavement had to be replaced.

Checks by local coring and particularly during repair work revealed a good agreement between radar results and pavement conditions.

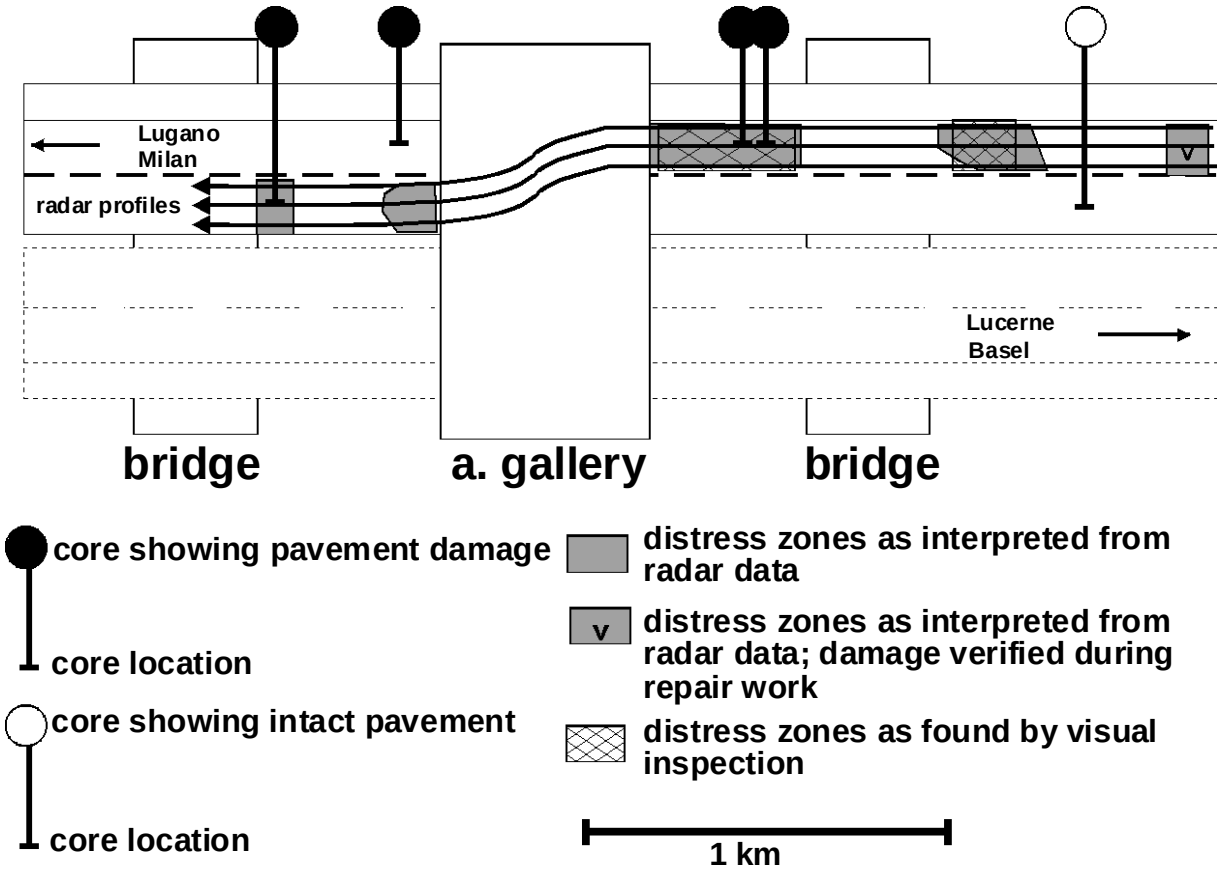

Figure 121: Simplified version of the map showing damaged pavement zones detected by GPR, coring and visual inspection as drawn by the road engineer.

Quality control

Figure 122 and Figure 123 show a comparison between two radar data sets obtained before and after the upper 15 cm of the pavement had been replaced. The pavement base is not identical in the two figures as the two profiles displayed are running parallel.

In the data set acquired before pavement rehabilitation (Figure 122) there is a heterogenous pattern of pavement internal reflections, particularly near the surface. The data set acquired after the completion of the repair work (Figure 123) shows reduced reflections from within

the pavement suggesting that the pavement rehabilitation was successful. A reflection resulting from the boundary between old and new pavement can be distinguished. The interpretation of the data set presented in Figure 123 together with a sketch of a core that was taken after the completion of repair work is shown in Figure 124. The conversion from time to depth was performed using the same signal velocity as in Figure 120 ($v=1.15 \cdot 10^8$ m/s).

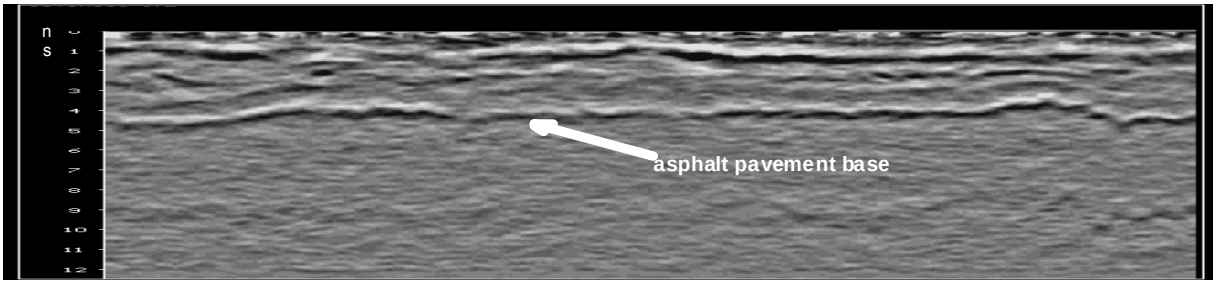

Figure 122: 2.5 GHz profile recorded before the start of repair work, length 180 m.

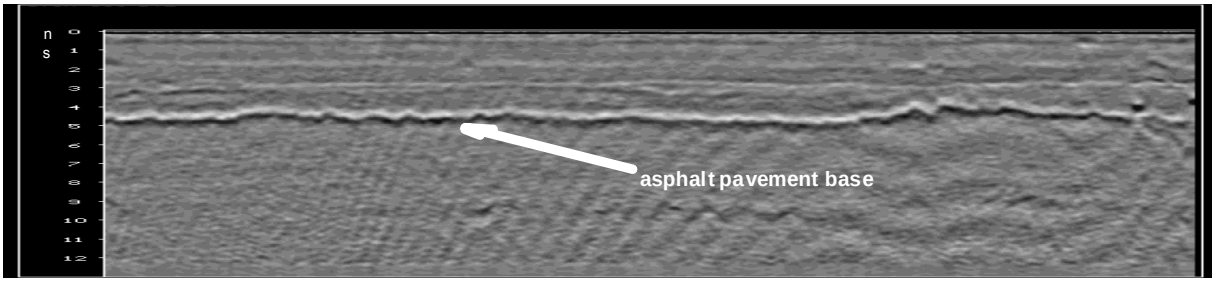

Figure 123: 2.5 GHz profile recorded after the completion of repair work, length 180 m.

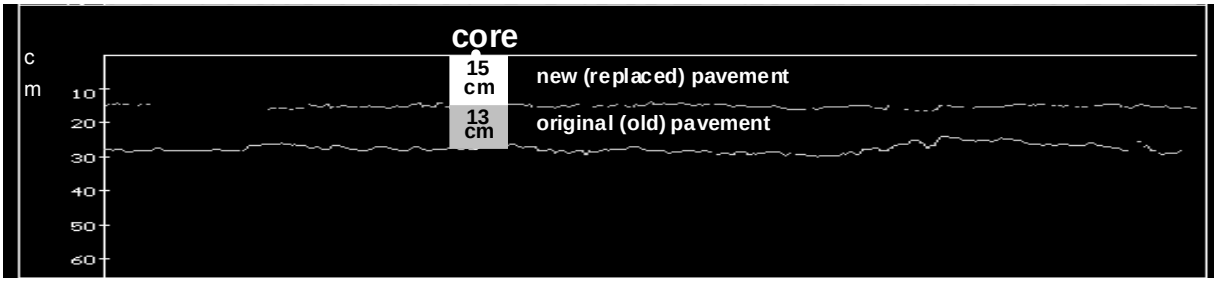

Figure 124: Interpretation of 2.5 GHz profile (Figure 123) after completion of repair work.

Conclusions

The radar survey proved to be a valuable complement to traditional distress monitoring methods in supporting the planning of repair work.

Previously unknown damaged zones were detected and the horizontal extent of known problem zones as well as the depth of the pavement problems could be defined over wide areas. This knowledge was essential for deciding where, to what extent and to what depth the pavement had to be replaced

Co-operation between the geophysicist interpreting the radar data and the road engineer investigating the road by other means was essential for interpretation.

The comparison between two data sets obtained before and after rehabilitation work suggests the suitability of GPR as a tool for quality control.

References

1. Davis J.L., Rossiter J.R., Mesher D., Dawley C. (1994) Quantitative Measurement of Pavement Structures using Radar, 5th International Conference on Ground Penetrating Radar, Kitchener, Canada, Waterloo Center for Groundwater Research: 319-334
2. Hugenschmidt J. (1996) Non-destructive inspection of roads using GPR, 2nd meeting environmental & engineering geophysics, Nantes, France: 224-227
3. Parry N.S., Davis J.L. (1992) GPR Systems for Roads and Bridges, 4th International Conference on Ground Penetrating Radar, Rovaniemi, Finland: 247-257
4. Roddis W. M., Maser K., Gisi A. J. (1992) Radar Pavement Thickness Evaluations for Varying Base Conditions, Transportation Research Record 1355, National Academy Press, Washington D.C.: 90-98

9 Appendix C - Railway track inspection using GPR

Johannes Hugenschmidt

Journal of Applied Geophysics 43 (2000): 147–155

Abstract

Swiss Federal Railways (SBB) inspect their railway tracks at regular intervals. The first step of track renewal planning is a geotechnical study. Inspection is focused on the thickness of the ballast, on subsoil material penetrating upwards into the ballast and on geotechnical properties of subgrade and subsoil materials. Up to now, the inspection has been done mainly by digging trenches at evenly spaced intervals and in locations of special interest.

In order to evaluate the benefits and limits of GPR railway track inspections, three GPR surveys were carried out on three different railway lines. Data were acquired using a mobile system travelling at 10 km/h. Subsequent to radar data acquisition, trenches were dug. The positioning of some of the trench locations was based on preliminary GPR results in order to support the interpretation of GPR data. Only those trenches were available during interpretation of radar data. In addition, SBB performed their usual investigation programme. This provided an opportunity for checking the radar results in great detail.

Keywords: GPR, railway track inspection, ballast inspection, non-destructive testing

Introduction

Up to now, in Switzerland the inspection of railway ballast beds, subgrade and subsoil has been done mainly by digging trenches at evenly spaced intervals and in locations of special interest. By doing so, detailed information was obtained at the trench locations but only little information was available in between. Also, digging trenches is expensive, destructive and obstructive to railway traffic.

When searching for a method allowing for a reduction of trenches required and providing information in between, GPR seems to be an obvious choice. GPR has been successfully applied for the investigation of other traffic-related structures such as road pavements and bridge decks. If mobile acquisition systems are used, data can be recorded economically causing minimal obstruction to traffic flow (Davis et al. 1994; Hugenschmidt, et al.1998). However, railway lines do not offer very favourable radar conditions. The problems caused by the presence of sleepers, tracks and numerous near- and subsurface installations have to be addressed by an appropriate approach to data acquisition and processing.

With the aim of evaluating the benefits and limits of GPR inspections, Swiss Federal Railways (SBB) placed an order with EMPA for the investigation of three railway lines. The focus of the radar inspections was on ballast thickness and on the detection of zones where subsoil material had penetrated into the ballast. The total length of the inspected sections was 15.1 km. In addition to the 41 trenches based on preliminary GPR results that were available during interpretation of radar data, SBB performed their usual investigation programme digging 77 trenches. This provided the opportunity for a quantitative evaluation of radar results.

Data acquisition

Data were acquired in summer 1997 using a GSSI SIR-10A system and a 900 MHz antenna (GSSI Model 3101D). Hänninen et al. (1992) provide more information on the 900 MHz antenna.

Figure 125 shows the survey wheel and the antenna mounted to a trailer which was pulled by a small diesel locomotive at 10 km/h.

The acquisition parameters can be summarized as follows:

- acquisition speed: 10 km/h
- horizontal sample rate: 15 scans/meter
- data word length: 16 bit
- samples per scan: 512
- antenna height: 8 cm, top of sleeper to bottom of antenna casing
- antenna orientation: at right angles to travelling direction
- scan length: 25 ns

In the weeks prior to the radar surveys and during data acquisition there was heavy rainfall.

Data were recorded and stored on tape without any processing. Also, no effort was made to avoid data collection when passing over sleepers as this would not only require a more sophisticated acquisition system but would also reduce the potential for future high speed data acquisition.

The site locations are shown in Figure 126. The different sections are presented in Table 9.

Figure 125: Set-up for mobile data acquisition on railway tracks.

Table 9: GPR sections.

Site	Name	Length	trenches available for interpretation	total number of trenches	Remarks
1	Au-Waedenswil	2.4 km	4	19	
1	Waedenswil-Au	2.4 km	5	20	
2	Rubigen-Guemligen	4.0 km	12	31	
3	Deitingen-Wangen	2.3 km	8	15	
3	Wangen-Deitingen	2.3 km	6	15	
3	Wangen Track 3	0.75 km	3	8	railway station
3	Wangen Track 4	0.95 km	3	10	railway station
		total: 15.1 km	total: 41	total: 118	

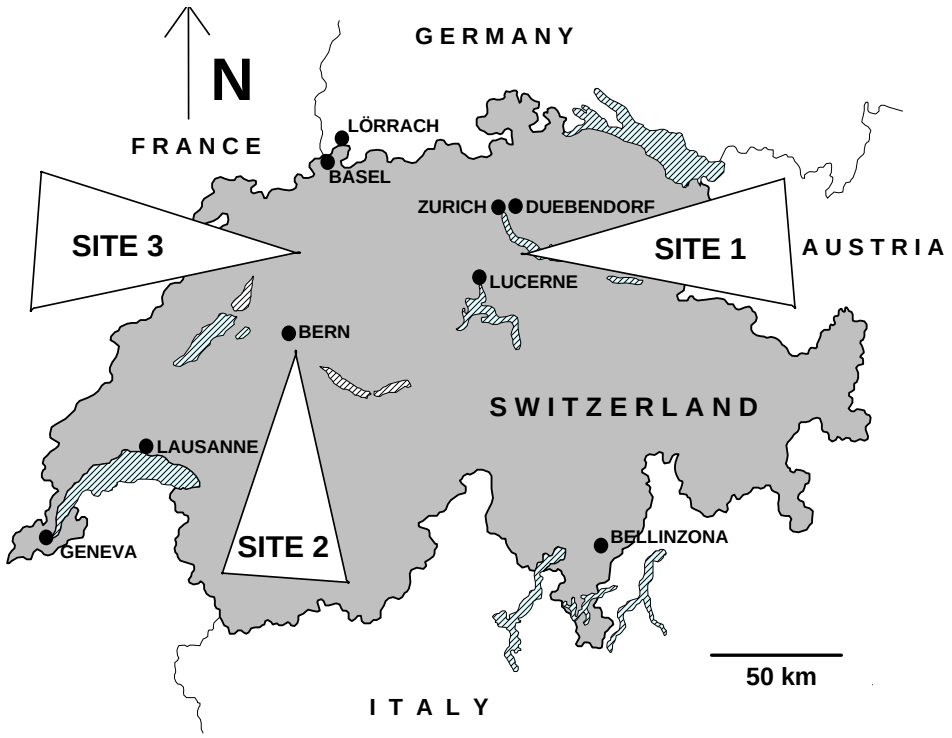

Figure 126: Location of GPR sites.

Data processing

Raw data were copied to a PC for processing. The aims of this processing can be summarized as follows:

Establishment of the ballast surface as a common reference level

- Enhancement of signal/noise ratio
- Introduction of coordinate system used by SBB
- Reduction of effects caused by sleepers

The following processing steps were applied:

1. bandpass filtering
2. correction of surface reflection to time zero
3. migration
4. horizontal scaling
5. Stack, 8-fold
6. background removal

7. horizontal smoothing
8. vertical gain correction
9. editing
10. transformation into SBB coordinates

A comparison between raw and processed data is presented in Figure 127. For ease of comparison, only every 5th trace has been plotted in the raw data set and the processed data set is displayed before transformation into SBB coordinates. Profile length is 40 m. Besides an obvious improvement of the signal/noise ratio, the surface reflection, around 3 ns in the raw data set, was shifted to time zero and eliminated by applying background removal. The influence of the sleepers, which caused a very irregular reflection pattern in the raw data, was reduced considerably.

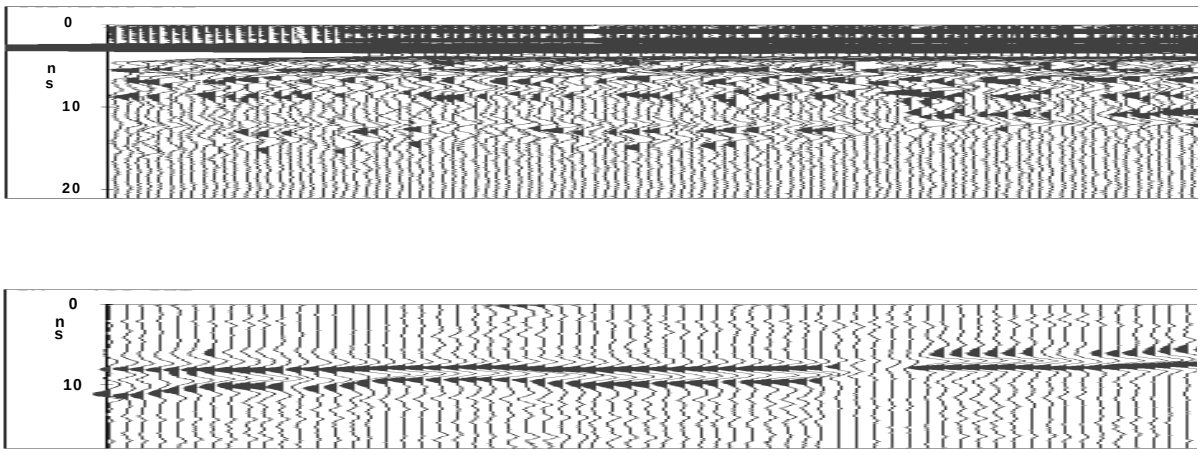

Figure 127: Comparison between data set before (top) and after processing (bottom), site 2, profile length 40 m.

Whereas processing aims such enhancement of the signal/noise ratio, correction of surface reflection or coordinate transformation are common to many GPR investigations, the reduction of the effects caused by sleepers is specific to railway track inspections and is therefore described in more detail. This reduction is achieved mainly through processing steps 3-6. In order to demonstrate the effects of these steps a subset of the data set presented in Figure 127 has been processed for demonstration purposes and is shown in Figure 128 to Figure 132. This subset was taken from the left part of the section presented in Figure 127 where there are two reflections of interest around 10 ns.

After bandpass filtering and correction of the surface reflection the two reflections are still masked by noise (Figure 128). Data were migrated using a signal velocity of $1.4 \cdot 10^8$ m/s. This velocity was chosen after a comparison of radar data with trench information. As a re-

sult the horizontal alignment of the two reflections is improved (Figure 129) and energy has been moved from traces which are covered by sleepers into traces which are not.

The data set after migration shows increased near surface signal amplitudes for traces recorded on sleepers. A time gate was defined (1.06-5.09 ns) and the mean amplitudes within this gate were scaled to the same level. By doing so, the amplitudes for the time range below the selected time gate are scaled down for sleeper traces (Figure 130). Please note that this scaling was not applied to all data sets because not all data sets showed a clear difference in near surface signal amplitudes between sleeper and non-sleeper traces. After stacking 8-fold (Figure 131) the two reflections of interest show only minimal reduction in resolution when compared to the data set in Figure 128. As near-surface reflections caused by sleepers show little variation horizontally, background removal is an efficient tool for reducing their amplitude (Figure 132).

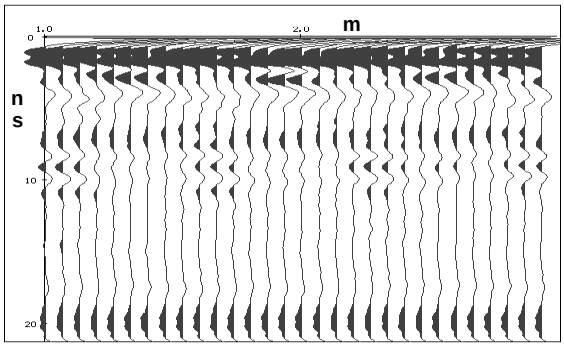

Figure 128: Data set after bandpass filtering and correction of surface reflection to time zero, profile length 2 m.

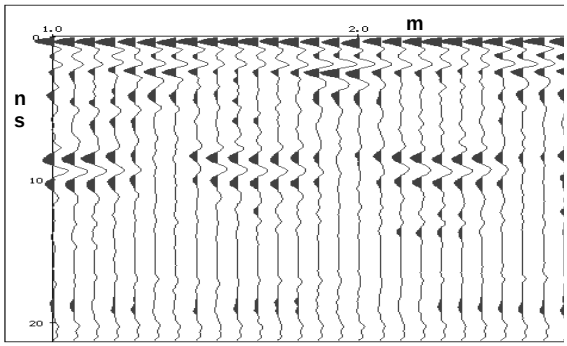

Figure 129: Data set after migration.

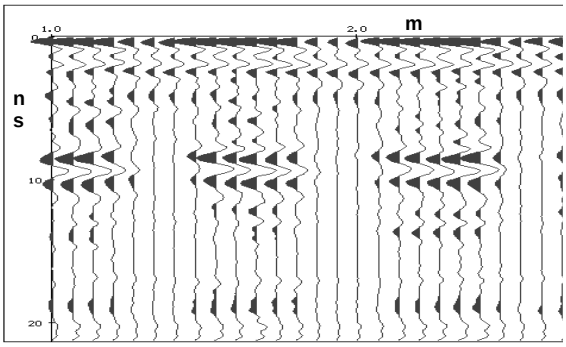

Figure 130: Data set after horizontal scaling.

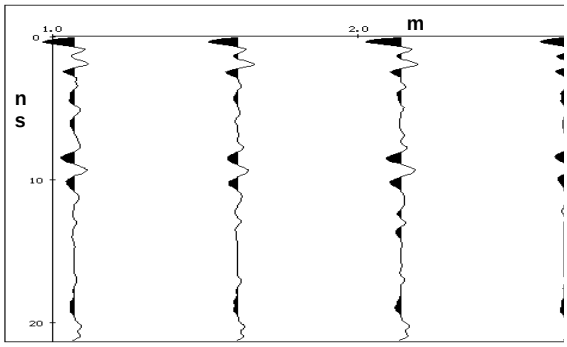

Figure 131: Data set after stack (8-fold).

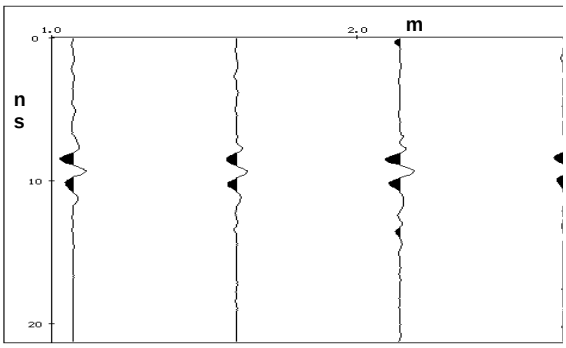

Figure 132: Data set after background removal.

Signal velocity

Göbel et al. (1994) investigated the influence of various parameters on the signal velocity within the ballast and found velocities varying between 0.8-1.2 · 10^8 m/s for soiled ballast and 1.2-2.1 · 10^8 m/s for clean ballast.

For economic reasons, the use of a constant signal velocity for the ballast is most desirable. Based on a comparison between radar data and trench information available during interpretation, it was found that a constant signal velocity for the ballast of 1.4 · 10^8 m/s gave good results almost everywhere. The mean difference for the thickness of the ballast bed between the radar results and trench information in all 34 locations, where this thickness could be defined by the radar survey, was 3 cm. As this proved to be sufficient, a constant signal velocity of 1.4 · 10^8 m/s was used for the ballast.

Results

Data quality

Data quality after processing was good almost everywhere. An example showing poor data quality is presented in Figure 133. This section was acquired within a railway station where numerous subsurface installations and material littered on the top of the ballast affected the quality of radar data.

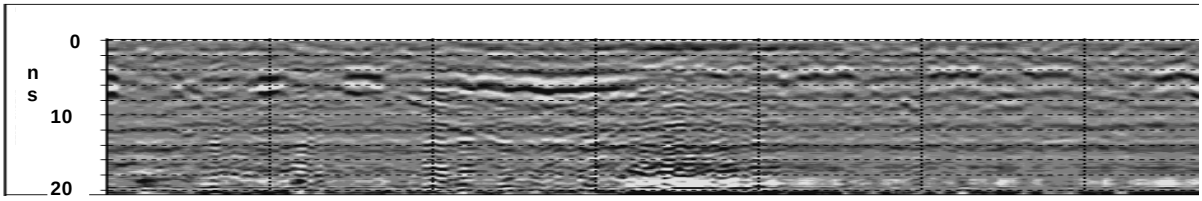

Figure 133: Example of poor data quality within railway station, site 3, profile length 200 m.

Thickness of ballast

A comparison between radar results and trench information not available during interpretation (49 comparisons) results in a mean difference of 4 cm. This is only slightly worse than that obtained during calibration and is sufficient for all practical purposes.

In Figure 134, a 750 m long section from site 3 is presented together with the results for the base of the ballast. The four trenches available in this section are presented by vertical lines together with the depth obtained by the radar survey (number left of line) and the trenches (right of line) respectively. Almost everywhere in the section presented, the identification of the base of the ballast is straightforward. A different situation is encountered at trench location 66200 where the first reflection from the top does not result from the bottom of the

ballast but from a reflector within the ballast caused by a partial cleaning of formerly soiled ballast. Trench location 66200 was defined after viewing the data and was available during interpretation. Without this information this situation would probably have been misinterpreted.

In three locations the difference between radar and trench results was found to be greater than 10 cm, the maximum difference being 20 cm due to a misinterpretation of a reflector within the ballast caused by partial cleaning.

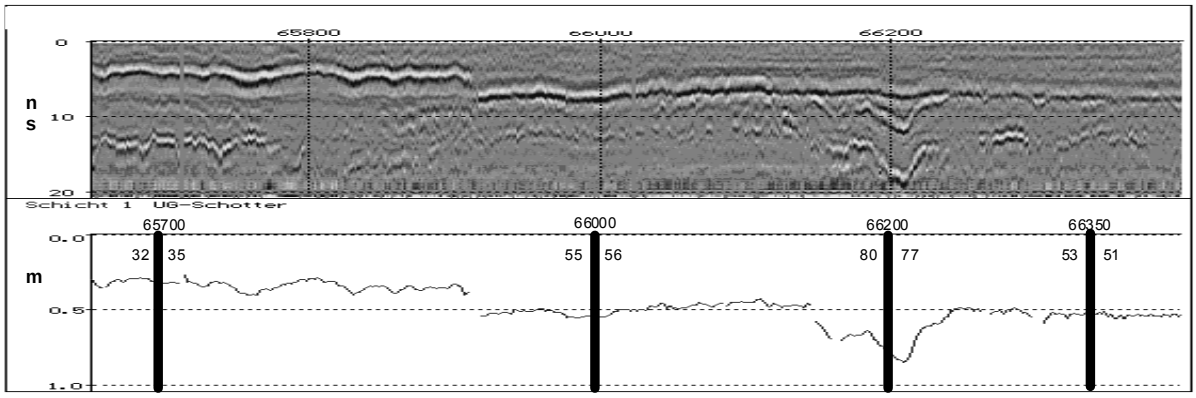

Figure 134: Comparison between radar results (left number) and trench information (right number) for bottom of ballast, site 3, profile length 750 m.

Subsoil material penetrating into the ballast

Subsoil material penetrating into the ballast was found in 19 trench locations. In addition to this, material penetrated only into small parts of the ballast (Figure 135, left). As the radar survey was not expected to locate such zones they were not included in the following description which is restricted to locations with subsoil material halfway in between rails.

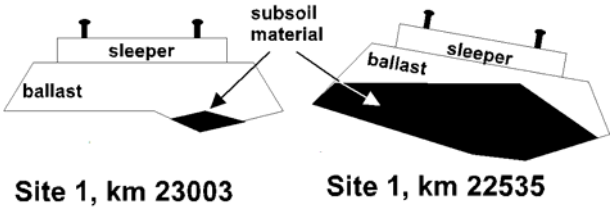

Figure 135: Subsoil material that has penetrated only into small parts of the ballast (left) and subsoil material halfway in between rails (right).

Twelve of the 19 zones of penetration (ZOPs) were identified by the radar survey, two more were defined as possible ZOPs. Five ZOPs remained undetected by the radar survey for two reasons:

- In two locations the penetration of subsoil material was only 2 cm resp. 4 cm.
- Three ZOPs were located in or near a railway station where data quality was poor due to numerous installations in the subsurface and material littered on the top of the ballast.

Twenty three ZOPs that were not found by trenches due to the large distance between trench locations, were located by the radar survey. Also, the horizontal extent of most ZOPs could be defined.

In Figure 136, a section of radar data is presented revealing not only several zones where clay had penetrated but also showing the top of the clay beneath the ballast. As in most other ZOP locations, no ballast thickness was obtained within the two ZOPs due to the strong attenuation of the radar signal within the clay.

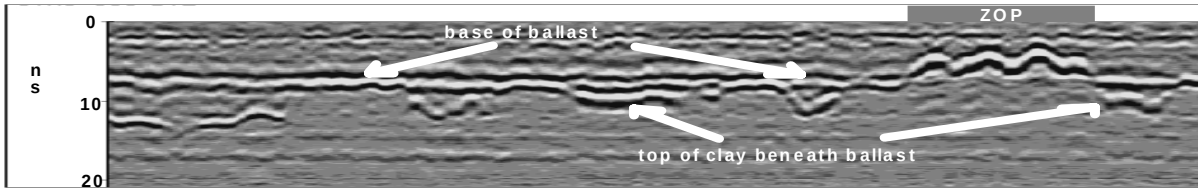

Figure 136: Data section showing two zones of penetration (ZOPs), site 1, profile length 200 m.

Subgrade and subsoil

Structures beneath the ballast such as subgrade and subsoil interfaces are also of interest to the railway engineer. The radar surveys presented in this paper revealed such structures in some sections only. An example is presented in Figure 137 where a reflection can be distinguished arriving later than that caused by the bottom of the ballast. A trench marked in Figure 137 revealed 42 cm of ballast followed by 42 cm of sandy gravel on top of silt containing clay and sand. Please note that this information was obtained just outside the rails whereas radar data were acquired in the middle between the rails.

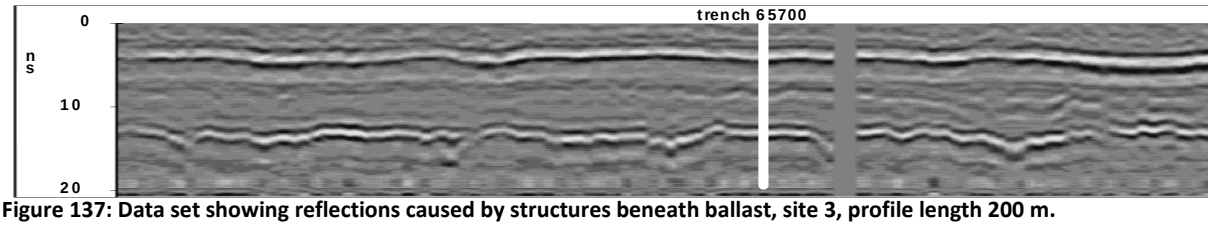

Figure 137: Data set showing reflections caused by structures beneath ballast, site 3, profile length 200 m.

Conclusions

The radar survey proved very useful to complement traditional inspection methods. The validation of radar results by numerous trenches that were not available until after interpretation of radar data, suggests that a considerable reduction of the number of trenches required for the inspection of the ballast is possible.

Using a constant signal velocity of $1.4 \cdot 10^8$ m/s resulted in a satisfactory accuracy for the thickness of the ballast almost everywhere.

Subsoil material penetrating into the ballast was identified very reliably. Such zones only remained undetected in a railway station where data quality was rather poor and in two cases where penetration was as little as 2 cm resp. 4 cm.

Acknowledgements

The author wishes to express his gratitude to Swiss Federal Railways, SBB for permission to publish the results described in this paper. Special thanks to Gerhard Schmutz from SBB for his comments on this paper and the fruitful discussion of radar results.

References

1. Davis J.L., Rossiter J.R., Mesher D., Dawley C. (1994) Quantitative Measurement of Pavement Structures using Radar, 5th International Conference on Ground Penetrating Radar, Kitchener, Canada, Waterloo Center for Groundwater Research: 319-334
2. Göbel, C., Hellmann, R., Petzold, H. (1994) Georadar-model and in-situ investigations for inspection of railway tracks, 5th International Conference on Ground Penetrating Radar, Kitchener, Canada, Waterloo Center for Groundwater Research: 1121-1133
3. Hänninnen P., Hänninen, P., Koponen L., Koshkiahde A., Maijala P., Pollari R., Saarenketo T., Sutinen R. (1992) Ground Penetrating Radar, The Finnish Geotechnical Society, Finland
4. Hugenschmidt, J., Partl, M. N., de Witte H. (1998) GPR inspection of a mountain motorway in Switzerland, J. Appl. Geophys. 40: 95-104

10 Appendix D - Concrete bridge inspection with a mobile GPR system

Johannes Hugenschmidt

Construction and Building Materials 16 (2002): 147–154

Abstract

A detailed knowledge of the present condition of bridges is essential for the planning of maintenance and rehabilitation. Mobile ground penetrating radar (GPR) systems are efficient tools for obtaining information such as depth of rebar, asphalt pavement thickness and concrete damage beneath the pavement. Non-destructive testing, quasi-continuous results and efficient data acquisition are the main advantages of mobile GPR systems.

In this paper, benefits and limitations of mobile GPR systems are discussed using examples from EMPA's recent work. The emphasis is on the investigation of pavement thicknesses and depths of rebar on concrete bridges.

Introduction

Most of Switzerland's motorways were built between 1960 and 1980 and many motorway bridges have now reached an age where rehabilitation work becomes necessary. For planning such work a detailed knowledge of the present bridge condition is essential. On the other hand, traffic has risen to a level where obstruction to traffic flow and road or lane closures have to be kept to a minimum. This situation led to an increased interest in methods capable of providing detailed information at affordable cost and with reduced obstruction to traffic.

In recent years, ground penetrating radar (GPR) has become an important tool for the inspection of bridges and many other structures, such as road pavements and tunnel walls (Davis et al., 1994; Daniels, 1996; Hugenschmidt et al., 1998a). GPR offers several advantages compared to traditional methods. In particular, it is non-destructive and results are quasi-continuous. Using a mobile GPR system to inspect bridge decks or road pavements permits a high rate of data acquisition with minimized traffic flow obstruction.

Data acquisition, is only the first step in a radar survey. It is followed by data processing and interpretation, during which the information contained within radar data is extracted and converted into a format meaningful to the bridge engineer. The availability of information obtained by other methods such as cores is always useful and often necessary to produce reliable and accurate results.

This paper focuses on radar inspections of bridges performed during contract work using a mobile GPR system. Benefits and limits are discussed by means of three case studies. In ad-

dition the principles of the radar method and a comparison between mobile and manual data acquisition are presented.

Radar principles

GPR is an electromagnetic investigation method. It is also known as surface penetrating radar or electromagnetic reflection method. It is mostly used in reflection mode, where a signal is emitted via an antenna into the structure under investigation. Reflected energy caused by changes in material properties is recorded (Figure 138) and analyzed.

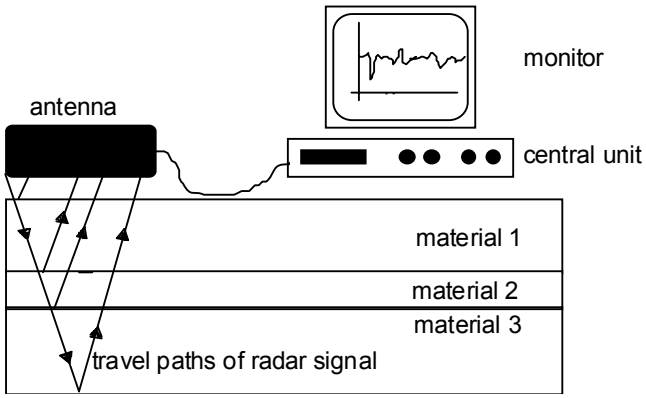

Figure 138: Radar principles.

A sketch of the emitted and recorded signal in wiggle and grey scale mode is presented in Figure 139. The signal recorded is usually referred to as a scan or trace. It should be noted that the vertical axis is a time axis. It denotes the time required by the signal to travel first to the reflector and then back to the antenna again. It is therefore referred to as two-way-traveltime (twt). All time specifications in this paper are given in twt. In order to obtain depths, the signal velocities in the different materials under investigation have to be known. There are several different ways to obtain these velocities. In all the case studies presented below, they were determined by a comparison of the radar data and core information.

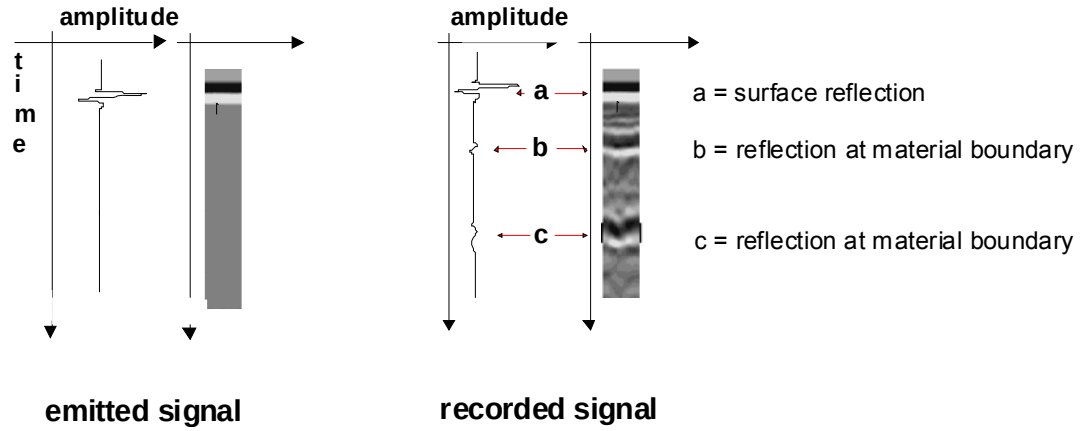

Figure 139: Comparison of emitted and recorded signal.

Different antenna types emitting and recording different ranges of frequencies are available. Using high-frequency antennae results in high resolution data, but reduces the depth of penetration. Low-frequency antennae provide greater depth of penetration at the expense of lower resolution. Most GPR manufacturers offer antennae with center frequencies ranging from about 50 MHz to about 1.5GHz. For bridge inspections, typically antennae with center frequencies above 1 GHz are used.

Daniels (1996) gives a detailed description of ground penetrating radar.

EMPA's approach to data acquisition, processing and interpretation

EMPA's mobile radar system is based on a GSSI SIR-10 system with horn antennae mounted on a plastic rack at the front of the vehicle (Figure 140) and a 900 MHz antenna situated at the back. When inspecting asphalt pavements on motorways, travelling speed is as high as 80 km/h. When inspecting bridges, however, the chosen travelling speed is as low as 10 km/h to ensure exact positioning with respect to a predefined profile line and to increase the number of measurements per meter to typically 20 traces (measurements). The latter is useful during interpretation of radar data, allowing a clear distinction between the upper layer of rebar and the asphalt pavement bottom or other layer boundaries that might be present (see below for details).

Figure 140: EMPA's mobile GPR system.

The case studies presented below were recorded with the horn antennae (GSSI Model H4205). The center frequency of these antennae is around 1.2 GHz (Hugenschmidt, 1998b). The three surveys were carried out during contract work for clients using acquisition parameters that were optimized with respect to the problem under investigation, economy, reliability and obstruction to traffic flow.

The 900 MHz antenna was not used for the three case studies documented in this paper. It offers increased depth of penetration, which was not required for these surveys, at the expense of reduced resolution when compared to the horn antennas. A comparison between data recorded with the horn antennae and the 900 MHz antenna is presented in (Hugenschmidt et al., 1998a).

In most cases, data are stored without application of on-site processing. Processing is performed on a PC and typically aims to:

- Increase the signal/noise ratio;
- Correct the asphalt surface reflection to time zero;
- Convert radar coordinates into the coordinates used by local authorities.

In Figure 141 a comparison between radar data before (top) and after (bottom) processing is presented. The section shown is 40 meters long. The processing sequence consisted of bandpass filtering followed by a correction of the pavement surface reflection (arrow) to time zero. This step includes a correction of antenna height variations. Afterwards background removal was applied by computing a mean trace and subtracting it from every single

trace. By doing so, constant noise such as reflections from the vehicle were removed. Finally, the original distance scale was adjusted to comply with distance along the bridge axis. In this example, a rather basic processing sequence was sufficient to fulfil the aims described above. Depending on data quality and the problem under investigation further processing steps may be required.

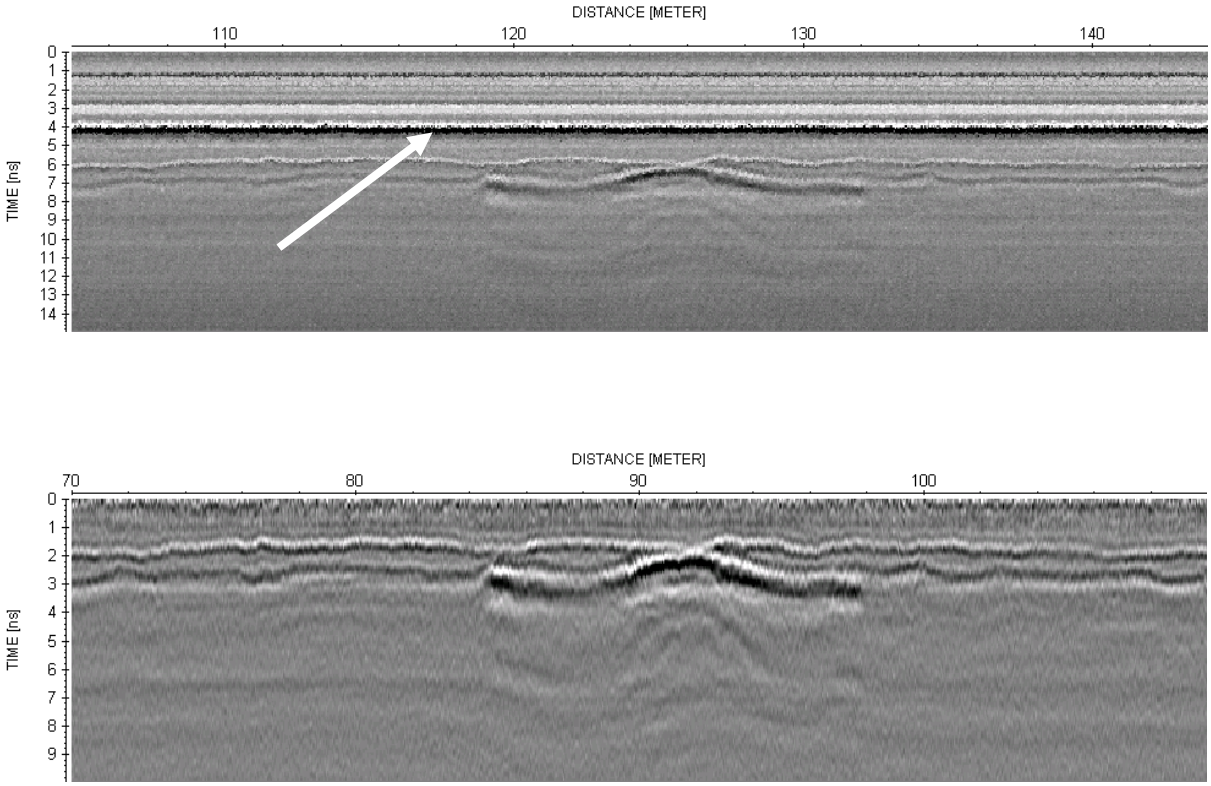

Figure 141: Comparison between data section before (top) and after processing (bottom), length 40 m.

Interpretation is the final step in a radar investigation, relating reflections within radar data to subsurface structures. If cores are available, the velocities of the radar signal within the different materials of the structure under investigation are determined by a comparison between travel times and layer thicknesses to enable a calibrated conversion of the original timescale to depth.

Case study 1: 4 bridges on San Bernardino road, Graubuenden, Switzerland

A radar survey was carried out on 4 concrete bridges (Ponte Quadinei, Ponte Cebia 1-3) on San Bernardino road. The inspection focused on rebar coverage. Data were acquired along 4 longitudinal profiles. The lane under inspection was closed to traffic. The total length of the 4 bridges was 597 m, resulting in a total survey length of 2388 m. The acquisition parameters can be summarized as follows:

- Horizontal distance between traces (measurements): 5 cm
- Acquisition speed: 10 km/h

In Figure 142, a processed data set from one of the bridges (Ponte Cebia 3) is presented together with the interpreted result for the rebar coverage. The vertical axis denotes nanoseconds in the data set and millimeters for the result. The reflections caused by the asphalt bottom (grey arrow) and by the top layer of rebar (white arrow) can be distinguished in the data set. An additional reflection (black arrow) is caused by the bottom of the concrete.

A constant signal velocity of $0.9 \cdot 10^8$ m/s within the concrete was used to convert the original time axis to depth. A comparison between radar results and 15 cores resulted in a mean difference of 6 mm for all 4 bridges.

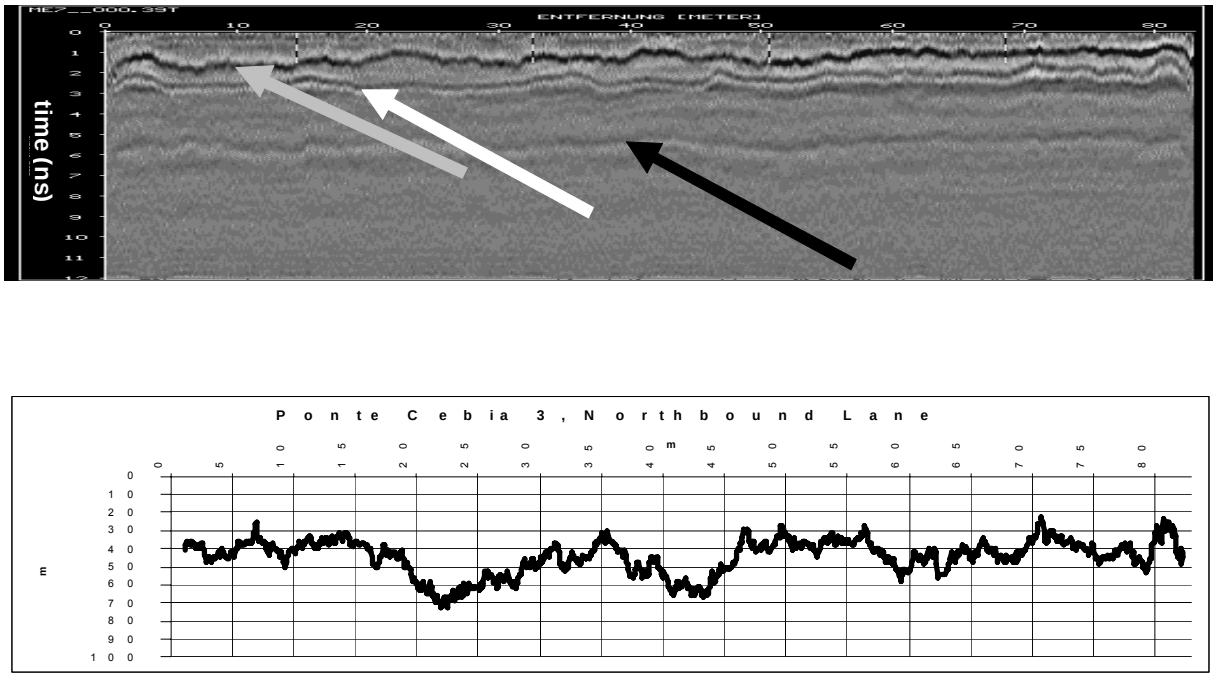

Figure 142: Radar data (top) and results for rebar coverage on Ponte Cebia 3, bridge length 82 m.

A 2 m-long data section from Ponte Cebia 3 is presented in Figure 143 (top). The 5 cm distance between traces (measurements) is too wide to properly map single rebars, since the spacing between them is around 20 cm. However the distance between traces is small enough to clearly distinguish the top layer of rebars (white arrows) from the asphalt bottom (grey arrow) by the regular variation in reflection strength. In the bottom section of Figure 143 the normalized signal amplitudes along the pavement bottom reflection (dotted line) and the rebar reflection (solid line) are plotted. The rebar reflection shows a regular pattern of amplitude maxima. The distance between those maxima is around 20 cm. The pavement

bottom reflection varies also in amplitude but there is no obvious repeat pattern. Thus, the evaluation of reflection amplitudes supports the identification of the rebar reflection.

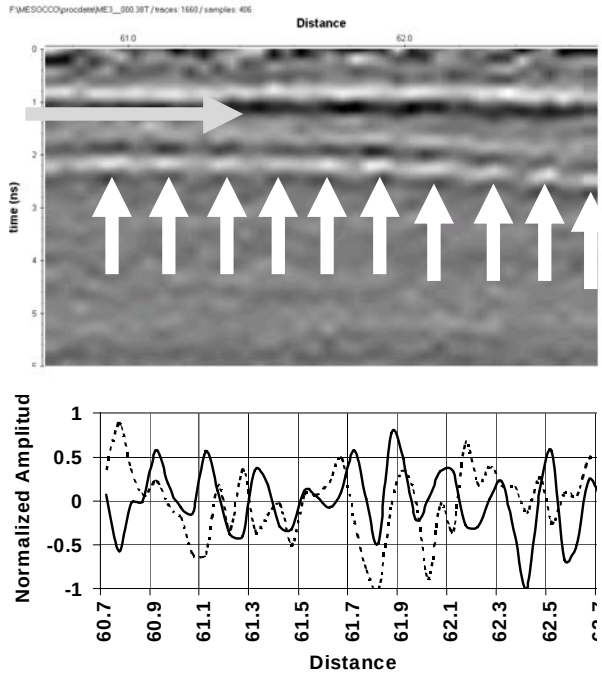

Figure 143: Enlarged data section from Ponte Cebia 3 (top, length 2 m), and normalized amplitudes (bottom) along pavement bottom reflection (dotted line) and rebar reflection (solid line).

Case study 2: Sihl flyover (Sihlhochstrasse), A3 motorway, Zurich, Switzerland

Sihl flyover (Sihlhochstrasse) is about 1.5 km long and entered service in 1973. Major rehabilitation is currently taking place. In order to determine the surface of the concrete bridge deck, which was covered by asphalt pavement, an EMPA radar inspection combined with a geodetic levelling survey by terra vermessungen ag of Zurich was carried out prior to present rehabilitation.

Radar and levelling data were acquired along 8 profiles covering the whole length of the structure and along 6 additional profiles of shorter length on the ramps, the lane under inspection being closed to traffic. Radar data were acquired using the same acquisition parameters as in case study 1. During interpretation of the radar data, 40 cores drilled along the radar profiles were available.

A 200 m-long section of processed radar data is presented in Figure 144 (top) together with the result for the pavement thickness (bottom). The reflection caused by the base of the asphalt pavement (white arrow) is clearly visible over the whole length of the section. A second reflection (black arrow) resulting from the top of rebar was not evaluated since it was not part of the project. A constant signal velocity of $1.24 \cdot 10^8$ m/s within the asphalt pavement was used for the conversion from time to depth. This resulted in a mean difference of 11 mm between the radar and core results.

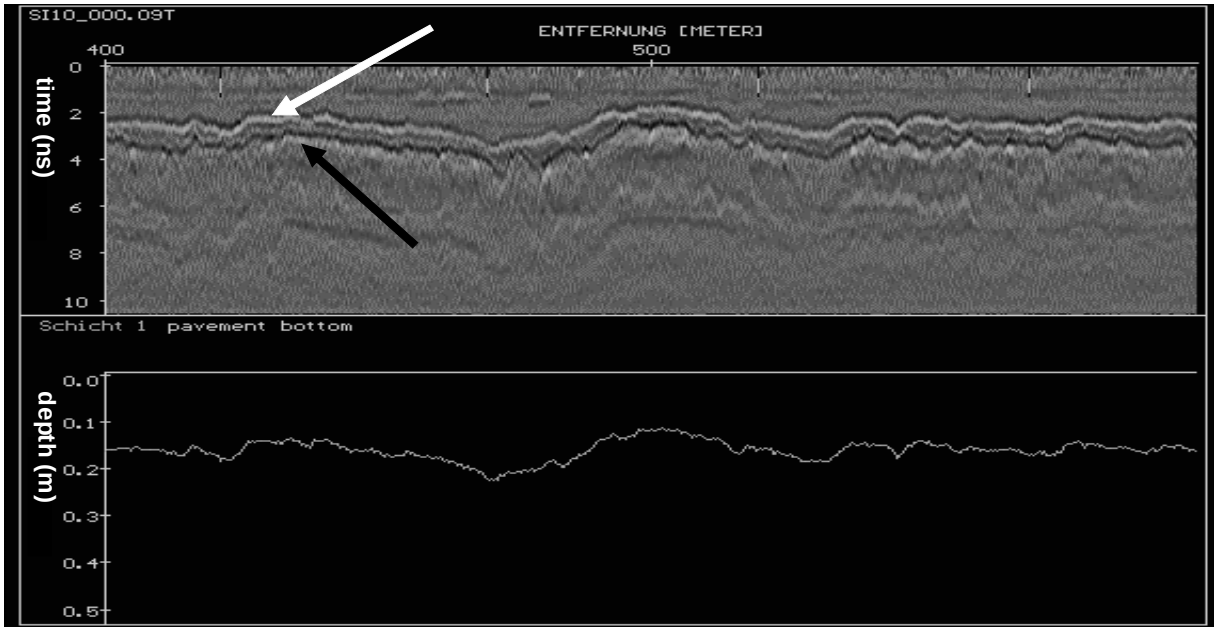

Figure 144: Data set (top) and interpreted result (bottom) for pavement thickness, length 200 m.

An area plot of the asphalt pavement thickness is presented in Figure 145. The section shown is 170 m long and 45 m wide. On this part of the bridge the pavement thickness varies between 9 and 28 cm. The corresponding plot for the surface of the asphalt pavement is presented in Figure 146. Subtraction of the results shown in Figure 146 and Figure 145 produces the height of the concrete surface given in Figure 147.

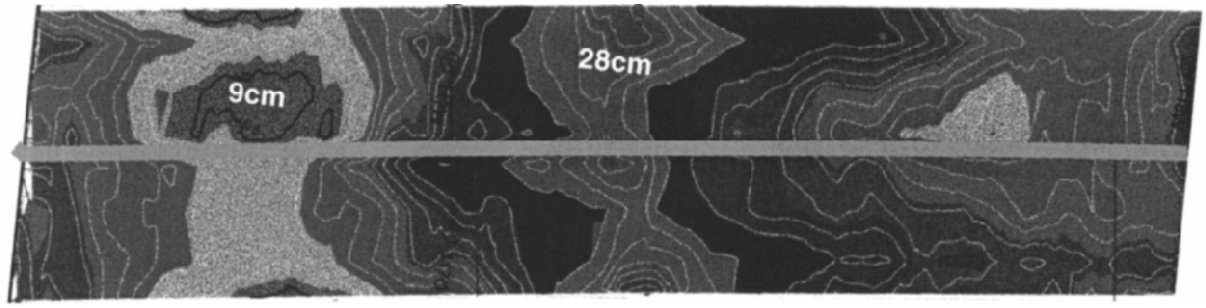

Figure 145: Asphalt pavement thickness, area plot covering 7990 square meters, the solid grey line denotes the separation between north- and southbound lanes, courtesy of terra vermessungen ag.

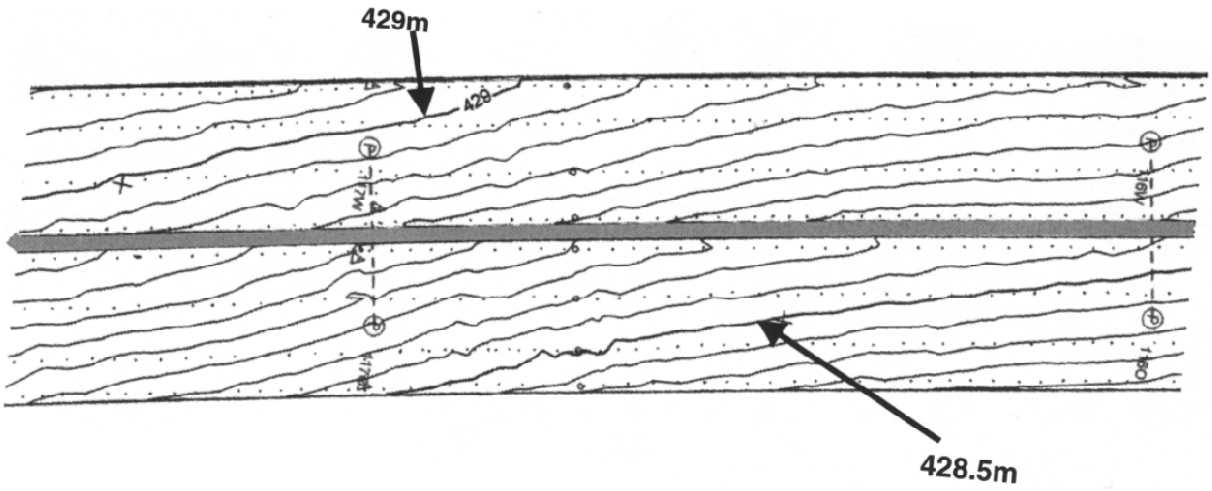

Figure 146: Height of asphalt surface, area plot covering 7990 square meters, the solid grey line denotes the separation between north- and southbound lanes, courtesy of terra vermessungen ag.

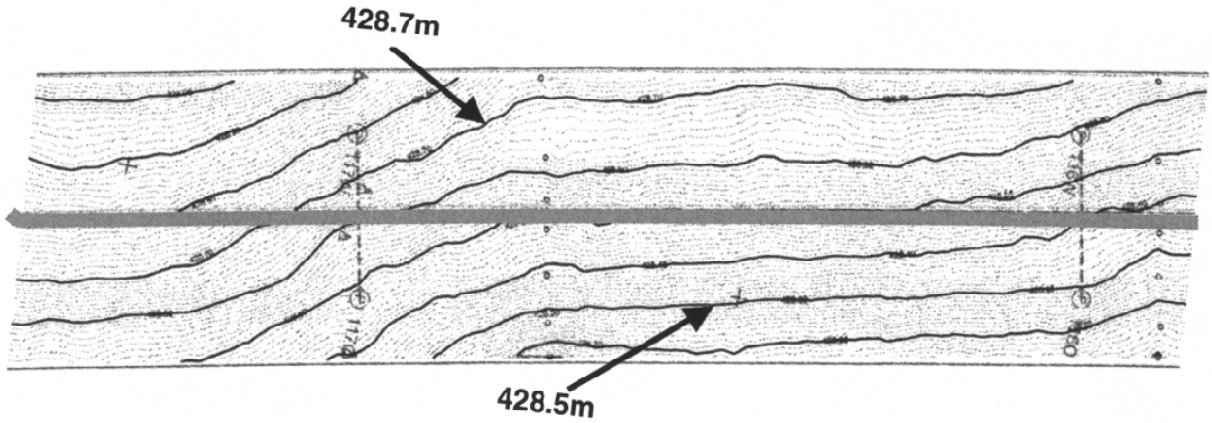

Figure 147: of concrete surface, area plot covering 7990 square meters, the solid grey line denotes the separation between north- and southbound lanes, courtesy of terra vermessungen ag.

Case study 3: High speed data acquisition, A2 motorway, Uri, Switzerland

In the above case studies, acquisition speed was 10 km/h to ensure exact positioning along a predefined profile line marked on the pavement. In addition, during the radar survey presented in case study 2 the lane under inspection had to be closed because of the levelling survey.

When performing radar surveys on motorways that are open to traffic, the acquisition speed has to be increased for safety reasons. This and the fact that the driver of the mobile GPR system has to pay heed to the flowing traffic will reduce the accuracy of positioning relative to a predefined reference. A solution to this problem is in sight. As GPS (global positioning system) is becoming faster and more accurate, it will become possible to store radar and GPS data in real time, thus eliminating the need for predefined profile lines in many cases

(Müller, 1999). Whether and when this approach will become an economical alternative has to be evaluated.

A radar survey was carried out on a 3.2 km-long section of the A2 motorway (canton Uri). Acquisition speed was 50 km/h. Data were acquired in the middle of both lanes on both carriageways. The inspection focused on the thickness of the asphalt pavement.

In Figure 148 a 200 m-long section of radar data (top) is presented together with the results for the pavement thickness (bottom). A bridge is marked with a white bar. Both the asphalt bottom reflection (white arrow) and a second reflection (grey arrow) can be distinguished in the data set. This second reflection probably results from the top layer of rebar. It was not evaluated as rebar depth was not part of the project.

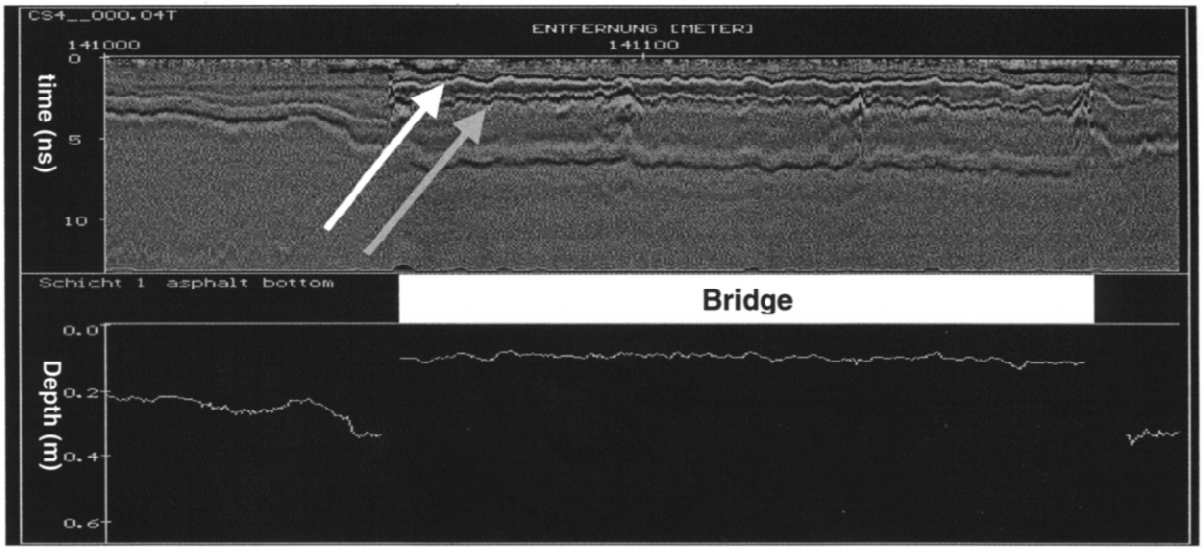

Figure 148: Data section (top) and results for pavement thickness (bottom) from motorway A2, length 200 m.

Comparison between mobile and manual data acquisition

EMPA's mobile data acquisition system was built to facilitate efficient inspection of roads and bridges. However, manual data recording offers advantages in certain cases. This is particularly true if very detailed results are required and if the area under inspection is small.

In Figure 149, an antenna suitable for manual data acquisition on concrete structures (GSSI, Model 5100) is shown mounted on a small cart built by EMPA to allow for a controlled movement of the antenna over the surface of the object under inspection. According to the manufacturer the center frequency of the Model 5100 antenna is 1.5 GHz on concrete. A test carried out by EMPA (Hugenschmidt, 2000) resulted in a center frequency of 1.2 GHz in air. If required, a second antenna of the same type is connected to this setup, thus increasing the distance between transmitter and receiver. This can be useful to reduce near-surface

noise and for the enhancement of deeper layers of rebar. A data set recorded with this setup on a concrete floor using an offset between the two antennae of 20 cm is presented in Figure 150. Single rebars can be easily identified at different depths.

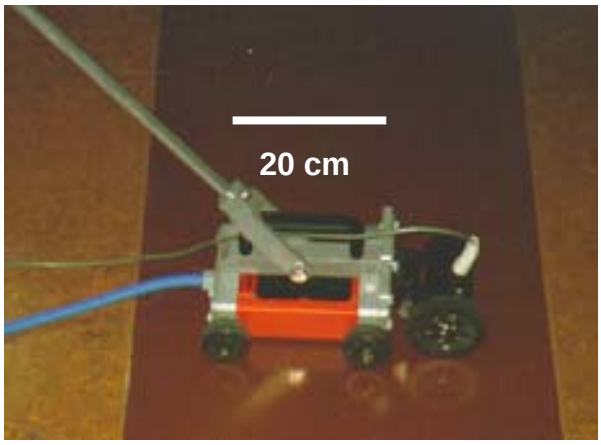

Figure 149: Antenna setup for manual data acquisition.

An example of a three-dimensional small-scale radar survey on a concrete floor is shown in Figure 151. It is a horizontal slice through a data cube consisting of 37 profiles along the x-axis and 51 profiles along the y-axis. Thus single rebars within a certain time (depth) gate are mapped.

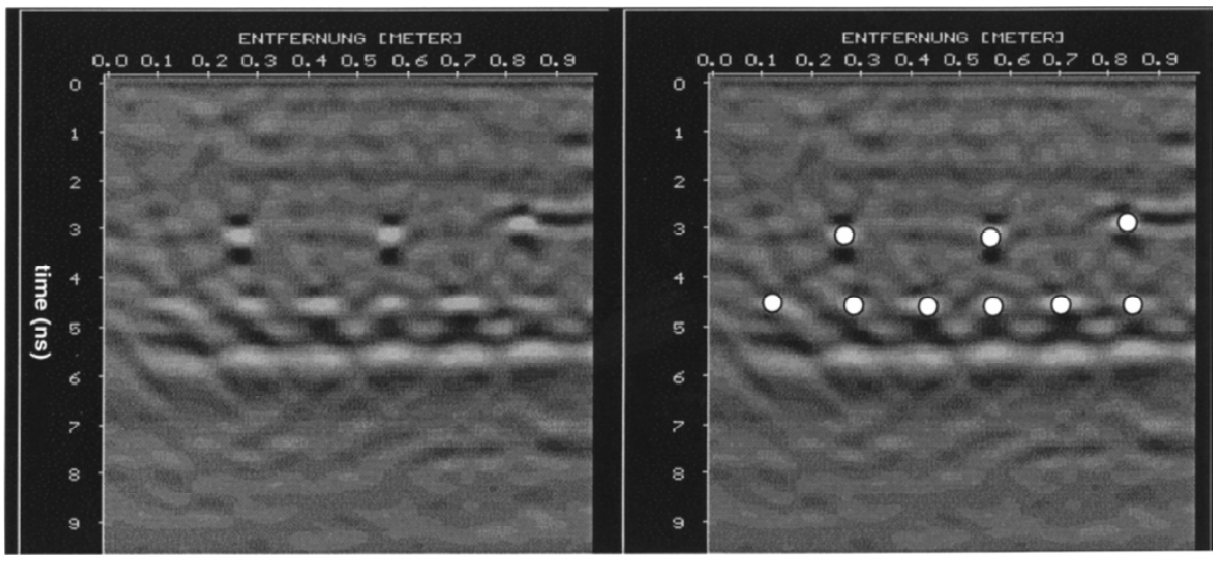

Figure 150: Data set acquired manually on concrete floor (left) and data set with interpretation (right, single rebars marked with white dots), the length of the section shown is 1 m.

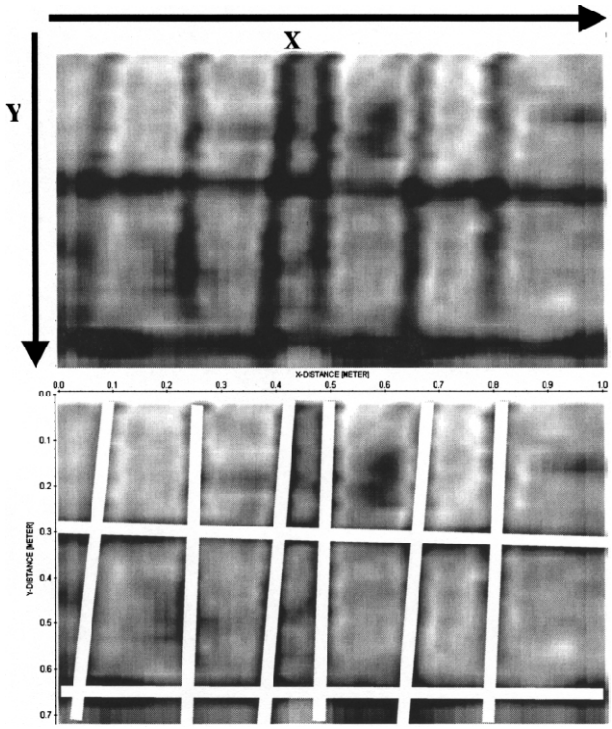

Figure 151: Time slice from three-dimensional data set acquired manually on concrete floor (top) and data set with interpretation (bottom, rebars marked with white lines), the length of the section shown is 1.0 m in the x-direction and 0.72 m in the y-direction.

When locating objects such as tendons on bridge decks manual data acquisition can also be of advantage. Provided the objects under consideration cause a clear response in the radar data, interpretation can take place during data acquisition. In Figure 152 two comparisons between tendon positions determined by a manual radar survey (black arrows) and reality (white arrows) are shown. Tendon positions were marked on the bridge deck during data acquisition.

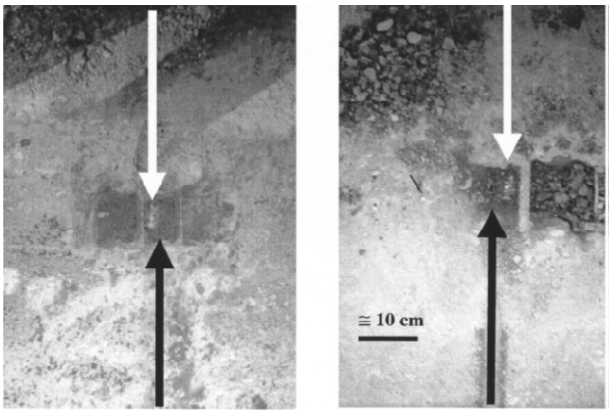

Figure 152: Comparison between tendon positions found with radar (black arrows) and reality (white arrows).

When choosing between manual or mobile data acquisition it should be remembered that manual data acquisition is significantly more time consuming on large sections and that obstruction to traffic flow is increased. On the other hand, if very detailed results are required, a manual survey might be the only solution.

The effort involved in acquiring and processing three-dimensional data sets such as the example presented in Figure 151 is several times higher than in a two-dimensional survey.

Conclusions

GPR is a powerful and economical tool for the non-destructive investigation of bridge decks.

Mobile GPR systems can considerably reduce the cost of data acquisition. Obstruction to traffic flow can be avoided or kept to a minimum.

The accuracy of radar results for layer thicknesses is typically between 5 and 15 mm if signal velocities are assumed to be horizontally invariant. This accuracy can be improved by taking into account velocity variations.

Acknowledgements

The author wishes to express his gratitude to the Building and Construction departments of canton Graubuenden, canton Zurich and canton Uri for their permission to publish the case studies described above. Special thanks to U. Mueller from terra vermessungen ag for preparing Figure 145, Figure 146 and Figure 147 and for his comments on this paper.

References

1. Daniels DJ. (1996) Surface Penetrating Radar, The Institution of Electrical Engineers, London, United Kingdom
2. Davis J.L., Rossiter J.R., Mesher D., Dawley C. (1994) Quantitative Measurement of Pavement Structures using Radar, 5th International Conference on Ground Penetrating Radar, Kitchener, Canada, Waterloo Center for Groundwater Research: 319-334
3. Hugenschmidt, J., Partl, M. N., de Witte H. (1998a) GPR inspection of a mountain motorway in Switzerland, J. Appl. Geophys. 40: 95-104
4. Hugenschmidt J. (1998b) Mobile Georadar-Anlage – Technische Beschreibung, EMPA Report Nr. FE 160617: 11
5. Hugenschmidt J. (2000) Multi-Offset-Analysis for man-made structures, 8th International Conference on Ground Penetrating Radar, Gold Coast, Australia: 414-420
6. Müller U. (1999) terra vermessungen ag, Zurich, personal communication

11 Appendix E - Curriculum vitae

Personal

Name	Johannes Hugenschmidt
Date of birth	01. 06. 1960
Place of birth	Freiburg, Germany
Nationality	German

Education

Since 2008	Doctoral student at the Institute of Geophysics, Swiss Federal Institute of Technology (ETH), Zurich, Switzerland
2010	Certificate of Advanced Studies in Applied Earth Sciences from Swiss Federal Institute of Technology (ETH), Zurich, Switzerland
2003	Executive MBA from St. Gallen University, Switzerland
1989	Diploma in Geophysics from Freie Universität Berlin, Germany
1979	Abitur from Hans-Thoma-Gymnasium, Lörrach, Germany

Work experience

Since 1995	Scientist with EMPA in Dübendorf, Switzerland
1992 – 1994	Geophycicist with Simultec AG in Meilen, Switzerland
1989 – 1992	Scientific Programmer with Ensign Geophysics, Addlestone, Surrey, UK
1984 – 1988	Employment with the Geophysical Institute of Freie Universität Berlin, Germany
1979 – 1981	Military service in Germany

12 Appendix F - List of publications

Journal publications - SCI and SCIE

1. Hugenschmidt J. (1998) GPR for road engineering, Materials and Structures 31: 192-194
2. Hugenschmidt, J., Partl, M. N., de Witte H. (1998) GPR inspection of a mountain motorway in Switzerland, J. Appl. Geophys. 40: 95-104
3. Hugenschmidt J. (2000) Railway track inspection using GPR, Journal of Applied Geophysics 43: 147-155
4. Hugenschmidt J. (2002) Concrete bridge inspection with a mobile GPR system, Construction and Building Materials 16: 147 – 154
5. Hugenschmidt J., Mastrangelo R. (2006) GPR inspection of concrete bridges, Cement & Concrete Composites 28: 384-392
6. Hugenschmidt J., Loser R. (2008) Detection of chlorides and moisture in concrete structures with Ground penetrating radar, Materials and Structures 41: 785-792
7. Hugenschmidt J., Kalogeropoulos A. (2009) The inspection of retaining walls using GPR, Journal of Applied Geophysics 67: 335-344
8. Hugenschmidt J., Kalogeropoulos A., Soldovieri F., Prisco G. (2010) Processing Strategies for high-resolution GPR Concrete Inspections, NDT&E International 43: 334-342

Journal publications – Other journals

1. Hugenschmidt J., Partl M. (1999) Die zerstörungsfreie Untersuchung von Asphaltbelägen mit dem Georadar-Verfahren, BITUMEN 61: 125-130
2. Hugenschmidt J. (2006) Georadar zur zerstörungsfreien Prüfung von Verkehrsbauwerken, MITTEILUNGEN der Deutschen Geophysikalischen Gesellschaft, Sonderband 2/2006: 69-84
3. Hugenschmidt J. (2008) Georadar zur zerstörungsfreien Prüfung von Verkehrsbauwerken, Strasse und Verkehr Nr. 1-2: 26-35
4. Hugenschmidt J (2008) Il Georadar per la valutazione non distruttiva di infrastrutture di trasporto, Il Giornale delle Prove non Distruttive Monitoraggio Diagnostica 4, Organo ufficiale dell'AIPnD: 38-46

Extended abstracts

1. Hugenschmidt J., Makin J., Neilson I., Teasdale N. (1991) A Commercial Parallel Seismic Processing System, International Workshop Parallel Architectures for Seismic Data Processing, IEEE UK & RI Signal Processing Chapter, Glasgow, UK: 12-19
2. Hugenschmidt J. (1996) Non-destructive inspection of roads using GPR, 2nd meeting environmental & engineering geophysics, Nantes, France: 224-227
3. Hugenschmidt J., Partl M., de Witte H. (1996) GPR Inspection of a Mountain Motorway - A Case Study, 6th International conference on Ground Penetrating Radar, Sendai, Japan: 365-370
4. Hugenschmidt J. (1997) Non-Destructive Testing using GPR - Current activities at EMPA, EAGE 59th Conference and Technical Exhibition, Geneva, Switzerland
5. Hugenschmidt J. (1997) Non-Destructive Evaluation of Bridge Decks using GPR- Benefits and Limits, US-Canada-Europe Workshop on Bridge Engineering, Zurich, Switzerland: 362-367
6. Hugenschmidt J. (1998) Railway track inspection using GPR - some examples from Switzerland, 7th International Conference in Ground Penetrating Radar, Lawrence, USA: 197-202
7. Hugenschmidt J. (1999) Ballast inspection using Ground Penetrating Radar, Railway Engineering 2nd International Conference and Exhibition, London, UK
8. Hugenschmidt J. (1999) Bridge inspection using a mobile GPR system, Structural faults and repair 8th International Conference and Exhibition, London, UK
9. Hugenschmidt J. (2000) Multi-Offset-Analysis for man-made structures, 8th International Conference on Ground Penetrating Radar, Gold Coast, Australia: 414-420
10. Hugenschmidt J. (2002) A one-to-one comparison between radar results and reality on a concrete bridge, 9th International Conference in Ground Penetrating Radar, Santa Barbara, USA: 427-432
11. Hugenschmidt J. (2003) Non-destructive-testing of traffic-infrastructure using GPR, International Symposium Non-Destructive Testing in Civil Engineering (NDT-CE), Berlin, Germany
12. Hugenschmidt J. (2004) Accuracy and reliability of radar results on bridge decks, 10th International Conference on Ground Penetrating Radar, Delft, the Netherlands: 371-374
13. Hugenschmidt J. and Kasa, C. (2005) NDT Inspection of Railway Tracks Embedded in Concrete, 8th Int. Conf on Railway Engineering 2005, London, UK
14. Hugenschmidt J. (2005) Assessment of the quality of radar results on bridge decks, Near Surface 2005, Palermo, Italy

15. Hugenschmidt J. (2006) The effects of chloride and moisture in concrete on radar amplitudes, 11th International Conference on Ground Penetrating Radar, Columbus, USA

16. Hugenschmidt J., Mastrangelo R. (2007) The inspection of large retaining walls using GPR, 4th International Workshop on Advanced Ground Penetrating Radar, Naples, Italy: 267-271

17. Hugenschmidt J., Kalogeropoulos A., Soldovieri F., Prisco G. (2008) Processing Strategies for high-resolution Concrete Inspections, 12th International Conference on Ground Penetrating Radar, Birmingham, UK

18. Hugenschmidt J., Kalogeropoulos A., Soldovieri F., Prisco G. (2009) Current Trends in Non-destructive Testing of Reinforced Concrete Structures using GPR, 4th International Conference on Structural Health Monitoring on Intelligent Infrastructure, Zurich, Switzerland